Phase Diagram Studies in the Mg-rich Corner of the Mg-Ce-In Ternary System

by

Elvi C. Dalgard

Department of Mining, Metals and Materials Engineering

McGill University, Montreal, Canada

August 2007

A thesis submitted to McGill University in partial fulfilment of the requirements of the degree of Master of Engineering

Abstract

In the present study, dilute alloys in the Mg-rich corner of the Mg-Ce-In ternary system in the composition range 0 to 3% In and 0 to 1.5% Ce were synthesized. Cooling curve analysis was used to determine the liquidus points in order to construct the liquidus surface of the ternary phase diagram in the Mg corner. Energy dispersive spectroscopy (EDS), wavelength dispersive spectroscopy (WDS), and x-ray diffraction (XRD) techniques were used to examine phases present at the compositions studied. A thermal arrest presumed to represent a eutectic transformation was discovered at 580°C. Two new intermetallic compounds, designated τ and θ, were found. Trace silicon present in the alloys was found to concentrate in one of the intermetallic compounds.

To further investigate these compounds, an induction furnace was used to synthesize alloys containing the concentrations of Ce and In seen in electron probe micro-analysis (EPMA) examinations of these compounds. The alloys were examined using the cooling curve technique and XRD, and proved to contain the compounds already observed with some variation in dissolved indium content. In addition, differential scanning calorimetry (DSC) was used to confirm the liquidus and solidus values determined using cooling curve analysis.

A diffusion couple with terminal compositions of pure Ce and a Mg-In alloy was prepared in order to determine the equilibrium phases present in the system between these two compositions at 390°C. EPMA was used to identify the zones obtained, and confirmed the presence of several Mg-Ce compounds with 1 at% dissolved indium, as well as a ternary compound corresponding to the θ compound found in the dilute alloys.

Finally, literature values and experimental data were used to calculate a preliminary ternary phase diagram using FACTSage, in collaboration with the CTRC at Ecole Polytechnique, in order to affirm the validity of the experimentally determined values as well as to project the diagram beyond the studied composition range.

Résumé

Dans la présente étude, des alliages dilués dans le coin de la composition riche en Mg du système ternaire de Mg-Ce-In dans la gamme de composition variant de 0 à 3% indium et 0 à 1.5% cérium ont été fabriqués. Des analyses des courbes de refroidissement ont été effectuées afin de déterminer les points du liquidus dans le but de permettre la construction de la surface liquide du diagramme ternaire dans le coin riche en magnésium. Des techniques telles que la spectroscopie par énergie dispersive, la spectroscopie dispersive de la longueur d'onde et la diffraction des rayons-X ont été utilisées pour examiner les phases présentes pour les compositions étudiées. Un palier thermique qui est supposé représenter une transformation eutectique a été découvert à la température de 580 °C. Deux nouveaux composés intermétalliques désignés par les symboles τ et θ ont été découverts. Le silicium présent dans ces alliages à un niveau de trace se retrouve concentré dans l'un des composés intermétalliques.

Afin d'analyser plus en détails ces composés, un four induction a été utilisé pour la fabrication d'alliages contenant les concentrations de cérium (Ce) et d'indium (In) qui ont été observées par microscopie électronique lors des analyses des composés effectuées par micro-sonde Les alliages ont été examinés en utilisant la technique des courbes de refroidissement et la technique de diffraction des rayons-X . Ces analyses ont alors prouvées la présence des composés avec certaines variations de la teneur en indium en solution dans ces alliages. De plus, la technique d'analyse par la calorimétrie différentielle (DSC) a été utilisée pour confirmer les valeurs des températures de fusion et de solidification obtenues lors des analyses des courbes de refroidissement.

Un couple de diffusion avec une composition finale de cérium pur et un alliage de Mg-In a été préparé dans le but de déterminer les phases en équilibre présentes dans le système entre ces deux compositions à la température de 390°C. La technique d'analyse par la microscopie avec micro-sonde a été utilisée pour identifier les zones obtenues et pour confirmer la présence de plusieurs composés Mg-Ce contenant 1 at% d'indium dissout et aussi la présence du composé θ trouvé dans les alliages dilués.

Finalement, des valeurs obtenues dans la littérature et dans les expériences réalisées dans cette étude ont été utilisées pour calculer le diagramme ternaire préliminaire. En

collaboration avec le CTRC de l'École Polytechnique de Montréal, le programme FACTSage a été utilisé pour confirmer la validité des valeurs expérimentales obtenues et pour prédire le diagramme au-delà de la gamme de composition étudiée dans ce projet.

Acknowledgements

Without the support of my family, I'd have given up long ago, so thank you Laurie, Elisabeth, Ilana and Jacob, as well as my parents and parents-in-law. Dr. A. Elisabeth Dalgaard, you showed me the way by going back to school for your advanced degrees so long after your bachelor's. Thank you. Friends also offered support, encouragement, and in Stuart Easson's case, custom software. Thank you, too.

Finally, though he was not directly involved in my research, Dr. André Laplante's cheery smile and bad puns were always a source of joy in my daily life, as in that of the whole department. Rest in peace, André.

Table of Contents

Table of Figures

Table of Tables

1 Introduction

The automotive and aerospace industries have long been aware of the benefits of replacing steel components with lighter-weight alloys in order to improve fuel efficiency and reduce emissions. Aluminum alloys have been extensively used for this purpose, but the weight savings offered by these alloys is in many cases no longer sufficient. Since Mg is 36% lighter per unit volume than Al and 78% lighter than iron, new wrought magnesium alloys are in demand to reduce component weight while maintaining structural integrity. Mg sheet could be used in body nonstructural and semi-structural applications, while extrusions could be used in such structural applications as spaceframes.

In magnesium wrought alloy development, the primary goal is to render the magnesium alloy more workable without sacrificing its low density or any other desirable property. Some elements may form a solid solution with magnesium, while others will form intermetallic compounds. Electron valency and atomic radius of the alloying additions are important parameters in the effect of the element on magnesium.[1] New alloy systems will provide opportunities for improved performance in magnesium.

When new alloy systems are being investigated, accurate and complete phase diagrams are essential tools. Given a set of thermodynamic variables, the equilibrium phase diagram indicates which phases are present and in what quantities when the system is at equilibrium. Experimentally determining the phase diagram of an unknown system involves techniques such as thermal analysis, X-ray diffraction, microstructure analysis, and diffusion couples.

The system studied in this work is magnesium-cerium-indium, for which no ternary phase diagram exists in the literature, either experimentally determined or thermodynamically calculated. Additionally, no known ternary intermetallics are described in the literature for this system.[2,3,4]

Indium was chosen for its large solid solubility region with magnesium on the magnesium-rich side of the phase diagram. The indium atom is similar in size to

magnesium, a necessary condition for this extensive solid solubility. In addition, it is trivalent, which may affect the axial ratio of the crystal structure and improve its formability.[1] Although indium is very dense in comparison with magnesium, small amounts should not negate the advantages of magnesium's low density, as can be seen from the fact that zinc, of a similar density to indium, is one of the most common alloying elements in magnesium.

The first Mg–rare-earth alloys developed used mischmetal (50% Ce, 30% La, 15% Nd, and 5% Pr) to strengthen magnesium[5] and reduce microporosity in wrought alloys such as Mg–1.25Zn–0.17MM. Table 1-I lists several commercial magnesium alloys containing rare earths. Rare earth (RE) additions are effective in improving the creep resistance of magnesium-based alloys. The rare earths also refine the grain size and improve the strength, ductility, toughness, weldability, machinability, and corrosion resistance. The high vapor pressure of Mg and the reactivity of rare-earth elements make experimental determination of complete phase diagrams difficult for these systems.[5] Commercial alloys containing rare earths are listed in Table 1-I.

The rare earth cerium was chosen for the large number of interesting intermetallic compounds that it forms with magnesium. Although these are desirable for precipitation hardening, which is not a goal when a wrought alloy is being considered, they also have the effect of refining the grain structure, which may lead to higher ductility.

The objective of this work was to study the liquidus surface, solidus surface, and phase boundaries in this ternary system, in the Mg-rich corner. In addition, ternary intermetallic compounds found in the system were investigated.

Table 1-I: Commercial Mg alloys containing rare earths

EK30A	Sand casting alloy; 2.5-4.0 RE, 0.2 Zr	
EK41A	Sand casting alloy; 3.5 Ce, 0.7 Zr	
EQ21A	Casting alloy; 0.7 Zr, 1.5 Ag, 2.1 RE (mostly Praseodymium and Neodymium)	Mainly obsolete, replaced by WE alloys
EZ33A	Casting alloy; 2.5-4.0 RE, 2.7 Zn, 0.6 Zr	Magnesium Elektron's ZRE1
QE22A	Casting alloy; 2.5 Ag, 2.1 Di, 0.7 Zr	Mainly obsolete, replaced by WE alloys
ZE41A	Casting alloy; 4.2 Zn, 1.2 RE, 0.7 Zr	
ZE63A	Casting alloy; 5.8 Zn, 2.6 RE, 0.7 Zr	
WE43A	Casting alloy; 4.0 Y, 2.4-4.4 RE, 0.7 Zr	Automotive applications
WE54A	Casting alloy; 5.2 Y, 2.5-4.0 RE, 0.7 Zr	Aerospace applications
ZE10A	Casting alloy; 1.0-1.5 Zn, 0.12-0.25 Ce,	
Elektron 21	0.2-0. Zn, 2.6-3.1 Nd, 1.0-1.7 Gd, 0.7 Zr	
MA8	Russian; 0.15-0.35 Ce, 1.3-2.2 Mn	
MA20	Russian; 0.12-0.25 Ce, 1.0-1.5 Zn, 0.05-0.12 Zr	
MA18	Russian; Ce, Al, Mn, Zn, Li	
MA21	Russian; Ce, Al, Mn, Zn, Cd, Li	

2 Literature Review

A phase diagram is the graphic representation of phase equilibria present in a system as a function of the controlling variables, typically composition and temperature. Phase diagrams are of fundamental importance for understanding the properties and structures of materials. They can be used in the development of new alloys, in processing and fabrication of these alloys into useful components, in the design and control of heat-treatment procedures, and in solving performance problems that arise with specific alloys. [6]

The construction of a phase diagram relies on data generated using a variety of research techniques. No single research method is sufficient to construct an accurate diagram. Section 2.1.2 will focus on these techniques.

Computational thermodynamics is a technique whereby phase diagrams are generated by analysis of the basic thermodynamic properties of the system. In addition to providing a useful check on experimental data, computational thermodynamics makes possible the prediction of some features of the system which are not easily measured, as well as the prediction of higher level phase diagrams, i.e. ternary systems, quaternary systems, and so on. [7] These methods are reviewed in section 2.1.3.

Magnesium alloys are attractive to the automotive and aerospace industries due to their low density and corresponding high specific strength. While numerous gravity casting and die casting alloys have already been developed and are in use, commercial wrought alloys have not been as well-studied. In its unalloyed state, magnesium has limited formability, so alloying additions for wrought alloys are chosen with the goal of improving the workability of the alloy.

A review of magnesium alloy systems and specifically of the Mg-Ce-In system forms the second part of this literature review, section 2.2. This section also includes alloy and diffusion couple preparation techniques and challenges.

2.1 Phase Diagram Research

2.1.1 Thermodynamic Basis of Phase Diagrams

The reactions between components in a system, the phases formed, and the shape of the resulting phase diagram can be explained and understood using the principles, laws, and terms of thermodynamics. The shapes of liquidus, solidus, and solvus curves are determined by the Gibbs energies of the relevant phase constituents as well as the energy of mixing of these components in the phase.[6]

Enthalpy. Thermal energy changes under constant pressure can be expressed in terms of the *enthalpy, H,* of a system. Enthalpy, also called *heat content,* is defined by:

$$H = E + PV$$

Enthalpy is a function of the state of the system, as is the product PV.

Entropy. The second law of thermodynamics can be expressed as "all natural processes tend to occur only with an increase in entropy, and the direction of the process always is such as to lead to an increase in entropy." Entropy represents the energy (per degree of absolute temperature, T) in a system that is not available for work. For processes taking place in a system in equilibrium with its surroundings, the change in entropy is defined as follows:

$$dS \equiv \frac{\delta Q}{T} \equiv \frac{dE + PdV}{T}$$

The entropy of all chemically homogeneous materials can be taken as zero at absolute zero temperature (0 K). This principle allows calculation of the absolute values of entropy of pure substances solely from heat capacity.

Gibbs Energy. Because both S and V are difficult to control experimentally, an additional term, *Gibbs energy, G,* is introduced, whereby:

$$G \equiv E + PV - TS \equiv H - TS$$

and

$$dG = dE + PdV + VdP - TdS - SdT$$

The *phase-field rule* specifies that at constant temperature and pressure, the number of phases in adjacent fields in a multi-component diagram must differ by one. The Gibbs phase rule is expressed:

$$P + F = C + N$$

where P is the number of phases present, F is the number of degrees of freedom, C is the number of components in the system, and N is the number of non-compositional variables.
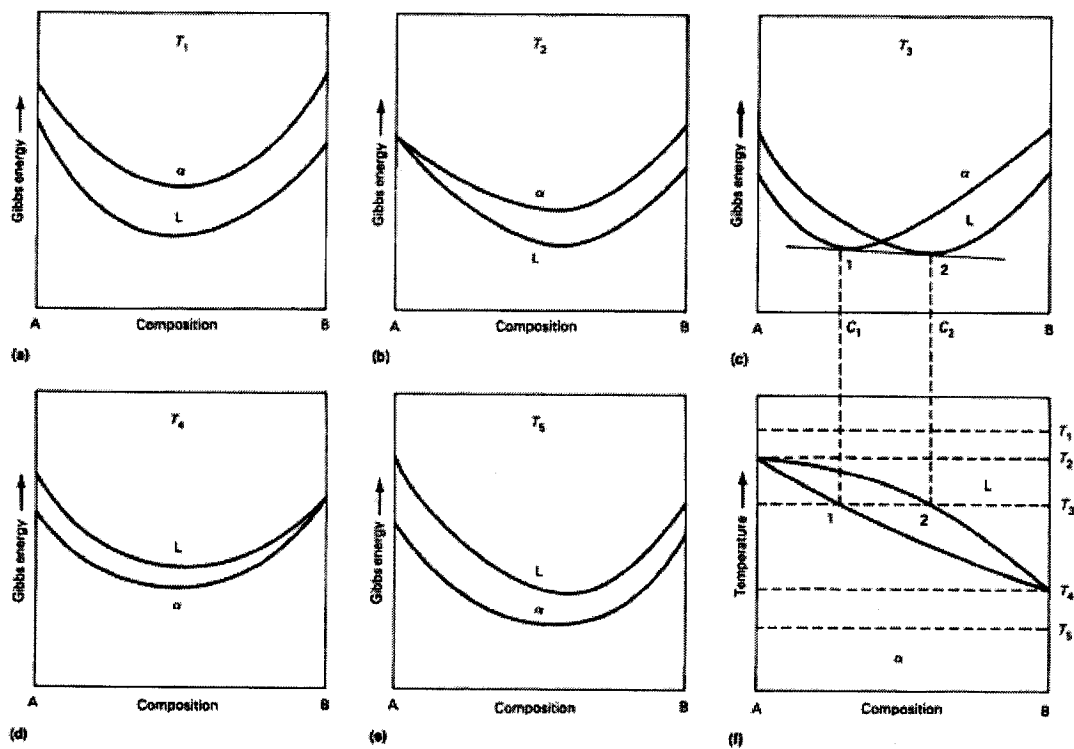
Figure 2-1 - Use of Gibbs energy curves to construct a binary phase diagram that shows miscibility in both the liquid and solid states.[6]

The two-phase field in Figure 2-1(f) consists of a mixture of liquid and solid phases. The compositions of the two phases in equilibrium at temperature T_3 are C_1 and C_2. The horizontal isothermal line connecting points 1 and 2 is called a *tie line*. Tie lines connect the coexisting phases throughout all two-phase fields (areas) in binary and (volumes) in

6

ternary systems, while *tie triangles* connect the coexisting phases throughout all three-phases regions (volumes) in ternary systems. Eutectic phase diagrams, a feature of which is a field where there is a mixture of two solid phases, also can be constructed from Gibbs energy curves.
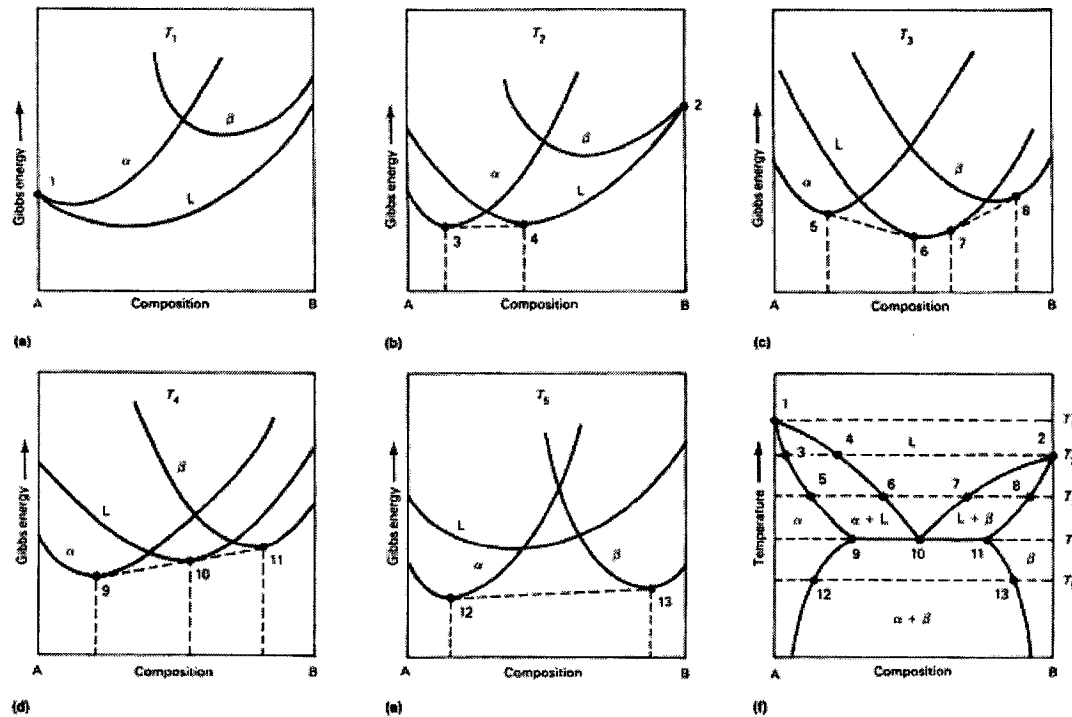
Figure 2-2 - Use of Gibbs energy curves to construct a binary eutectic phase diagram.[6]

The shapes of the boundary curves and angles at which they meet are also determined by thermodynamic principles. With these techniques and sufficient experimental data, phase diagrams can be calculated from first principles. Accuracy of the calculated diagram depends upon the completeness of the initial data as well as upon the correct application of the principles. [6]

2.1.2 Experimental Research Methods

The experimental methods used in phase diagram research are geared towards determining phase transformation temperatures and compositions, as well as phase boundaries. The techniques can be separated into dynamic and static methods.

Dynamic methods are those, such as thermal analysis, wherein the metal or alloy's properties are measured as a phase transformation is undergone. The difficulty is in relating this to the equilibrium state, since the alloy is clearly not in equilibrium.

The term static methods refers to techniques, such as high temperature X-ray diffraction, based on in-situ examination of a property in an equilibrium state. An alternative to high-temperature analysis is the use of annealed and quenched samples with room temperature analysis techniques.[8]

2.1.2.1 Phase Transformations

2.1.2.1.1 Thermal Analysis (Cooling Curve Method)

One of the most widely used methods for the determination of phase boundaries is thermal analysis. The temperature of a sample is monitored while it is allowed to cool naturally from an elevated temperature, usually in the liquid phase. The shape of the resulting curves of temperature versus time are then analysed for deviations from the smooth curve found for materials undergoing no phase change. The decreasing slope of the curve as the temperature decreases is due to a reduction in the heat-flow rate resulting from a smaller temperature difference between the cooling material and its surroundings.[6]

The occurrence of a phase transformation is accompanied by the release of latent heat for an exothermic reaction or by the need for additional heat, if the change is endothermic. These events are accompanied by arrests in the smooth cooling curve. In addition to the time-temperature curve itself, derivatives of this curve can also be used in

detecting and analyzing phase changes of the material.[9] An example of these curves can be seen in Figure 2-3.
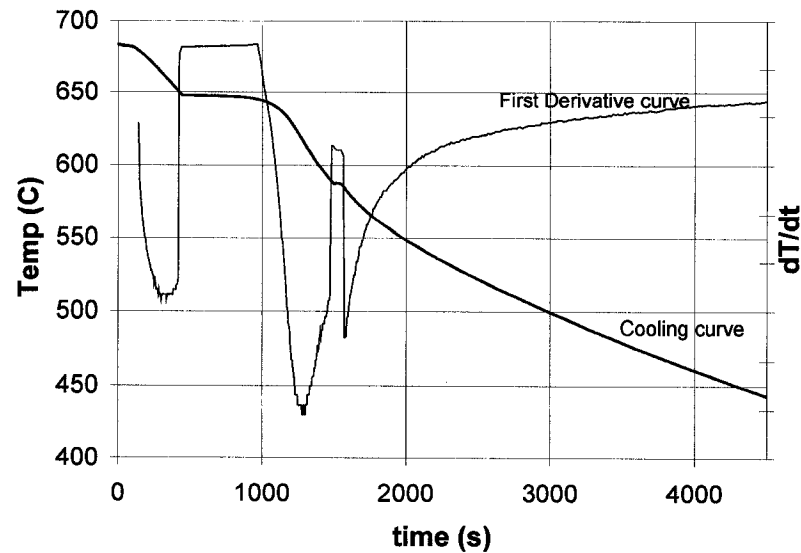
Figure 2-3 - Cooling curve and first derivative of a Mg alloy.

2.1.2.1.2 Differential Thermal Analysis and Differential Scanning Calorimetry

In differential thermal analysis (DTA), a schematic of which is shown in Figure 2-4, the temperature difference that develops between a sample and an inert reference material is measured when both are subjected to identical heat-treatments. DTA can, therefore, be used to study thermal properties and phase changes which do not lead to a change in enthalpy. The baseline of the DTA curve should then exhibit discontinuities at the transition temperatures and the slope of the curve at any point will depend on the phase constitution at that temperature. DTA is frequently used to determine liquidus and solidus temperatures, as well as temperatures of other phase changes.[10]
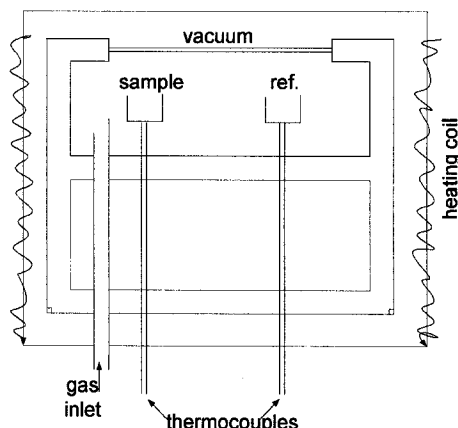
Figure 2-4 - Schematic of a DTA instrument.

The related technique of differential scanning calorimetry (DSC) relies on differences in energy required to maintain the sample and reference at an identical temperature. There are two types of DSC systems in common use. In power-compensation DSC the temperatures of the sample and reference are controlled independently using separate, identical furnaces. The temperatures of the sample and reference are made identical by varying the power input to the two furnaces; the energy required to do this is a measure of the enthalpy or heat capacity changes in the sample relative to the reference. In Figure 2-5 a schematic of this type of DSC instrument is shown.
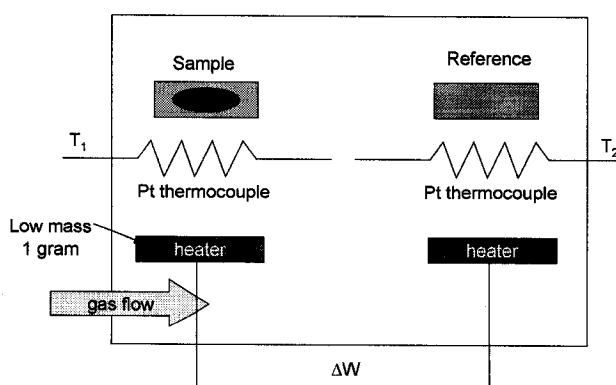
Figure 2-5 – Power compensation DSC schematic.

In heat-flux DSC, the sample and reference are connected by a low-resistance heat-flow path (a metal disc). The assembly is enclosed in a single furnace. Enthalpy or heat capacity changes in the sample cause a difference in its temperature relative to the reference; the resulting heat flow is small compared with that in DTA because the sample and reference are in good thermal contact. The temperature difference is recorded and related to enthalpy change in the sample using calibration experiments.

Using thermal analysis, DSC, and DTA, a phase diagram can be experimentally constructed. Figure 2-6 and Figure 2-7 show examples of determining the eutectic and liquidus temperatures in a hypothetical A-B binary system using cooling curves and DTA measurements. Example 1 corresponds to the eutectic composition and has only one thermal arrest. When the alloy reaches the eutectic temperature the latent heat evolved causes a delay in cooling until solidification is complete. This can be observed as an arrest on the cooling curve or as a sharp peak on the DTA. Example 2 has two thermal arrests: the first occurs when a liquidus line is crossed, slowing the cooling rate; the second corresponds to the eutectic temperature.[10]
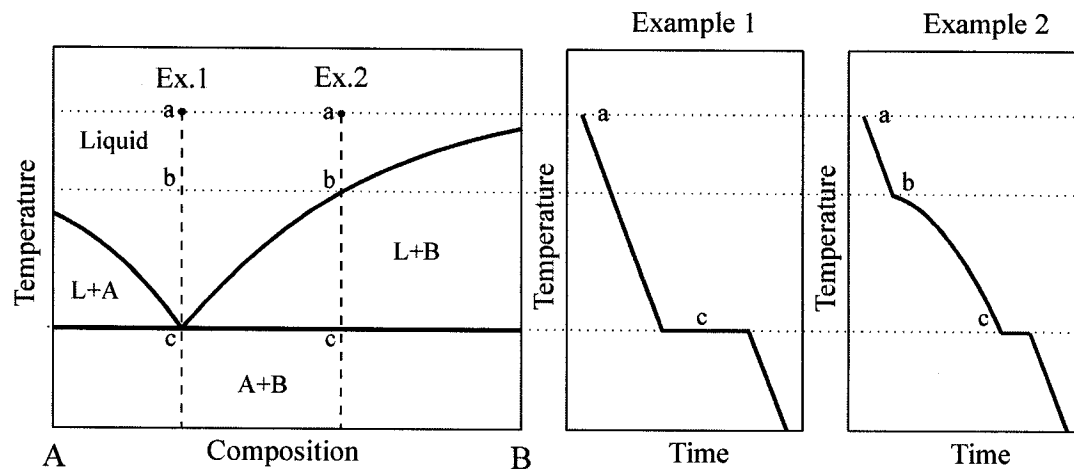
Figure 2-6 - Determination of phase transformations using the cooling curve technique.[6]
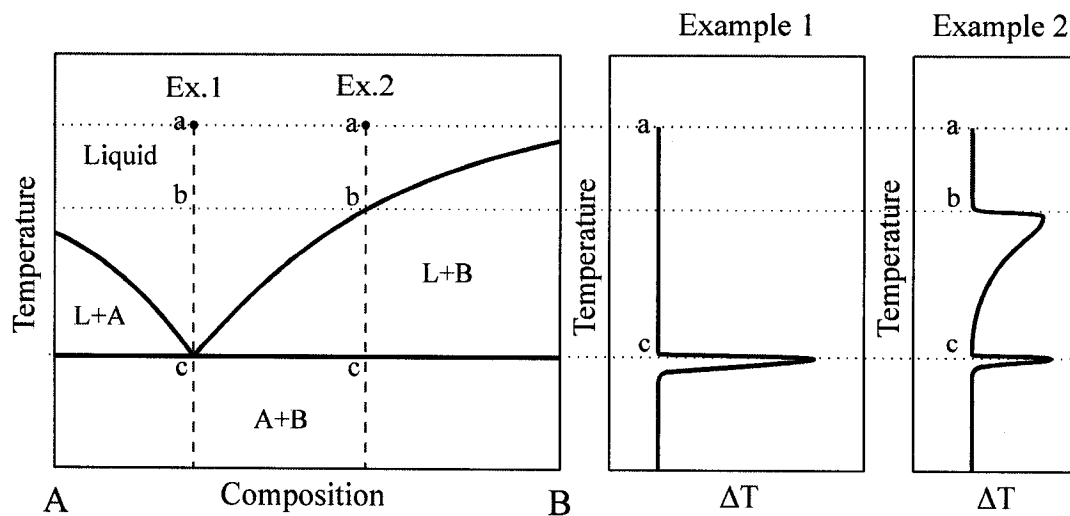
Figure 2-7 - Determination of phase transformations using DTA.[6]

It is not always easy to confidently identify the arrests visible in DTA and DSC graphs with respect to the equilibrium phase diagram, as cooling may be closer to Scheil conditions than to equilibrium. The Scheil model presumes a homogeneous liquid phase and no solute back diffusion in the solid phase. Solidification following the Scheil path, where diffusion in the solid is forbidden and thermodynamic equilibrium exists only as local equilibrium at the liquid/solid interface, produces worst case microsegregation with the lowest final freezing temperature. Modeling of real solidification behavior requires a kinetic analysis of microsegregation and back diffusion. However, for most low-alloyed compositions, the predictions of the Scheil model are close to reality. For high-alloyed compositions where Scheil predicts badly, thermodynamic calculations may assist in correctly identifying arrests.[11]

2.1.2.1.3 Anneal/Quench and Microstructural/XRD Examination

In this method, the heat treatment is designed to produce equilibriation of the system at a given temperature, and the sample is then rapidly cooled in order to preserve the phase assemblage. Solid solutions, solid state phase relations and liquidus phase equilibria can be investigated using quenching techniques. This technique relies on two assumptions: that equilibrium has been achieved before quenching, and that the heat treated structure has been preserved through quenching.[8]

The anneal-quench method for a hypothetical binary system relies on a large number of experiments at different compositions and annealing temperatures. If a mixture of composition X is heated to temperature T_a, in the liquid phase region, it will consist entirely of the liquid phase, and on quenching should reflect the mixture as it exists in the liquid — either an ideal mixture or one with some short or long range ordering.

If the experiment is repeated at a lower temperature T_b, subsequent analysis may show the presence of the amorphous "frozen liquid" phase as well as a crystalline phase. This would indicate that the liquidus lies between T_a and T_b. Further experiments at different temperatures between T_a and T_b could pinpoint the liquidus temperature more precisely. Similar series of experiments would be done at a variety of compositions in order to define where phase regions begin and end. In Figure 2-8 this technique is shown graphically, with samples being prepared at composition X and annealed at each temperature from T_1 to T_9. The maximal solid solubility of component B in the α phase can be evaluated from the two-phase samples (T_1, T_2, T_3, T_7, T_8, T_9).
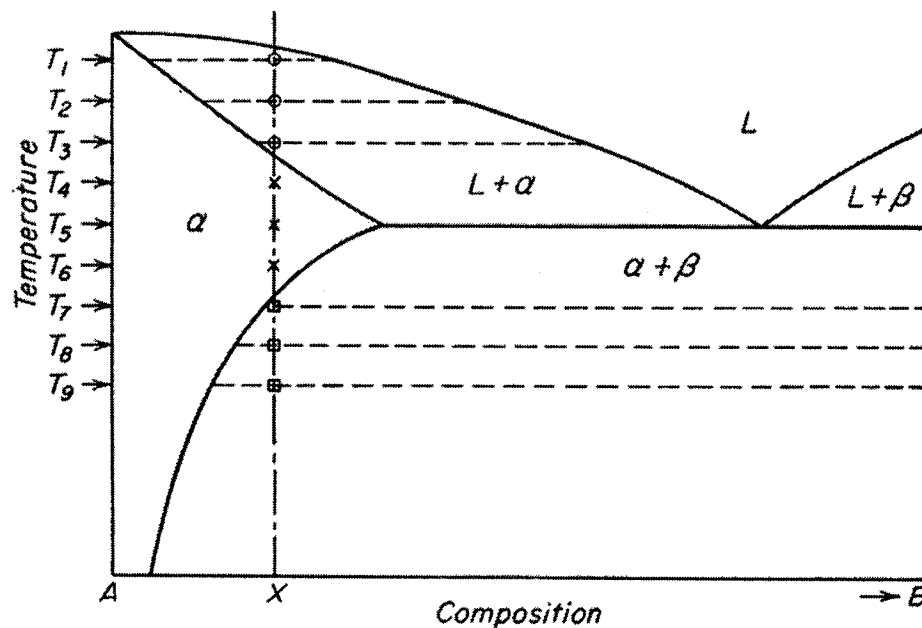
Figure 2-8 - Example of using anneal/quench technique with microstructural evaluation to determine phase boundaries.[10]

13

Figure 2-9 shows the result of a possible series of anneal-quench experiments designed to define the phase boundaries in a ternary system. In this case, B is held constant while the compositions of A and C are varied.
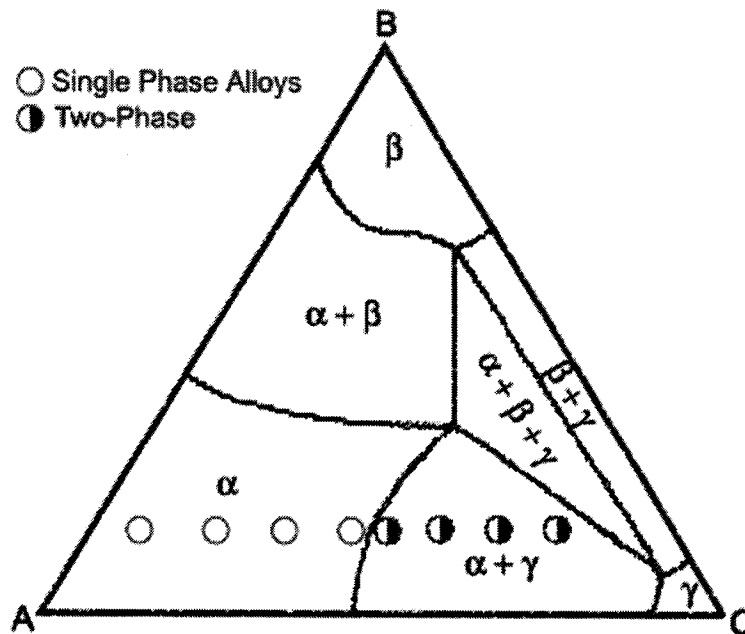
Figure 2-9 - Hypothetical ternary phase diagram indicating determination of a single phase to two phase boundary.[12]

2.1.2.1.4 Other Methods

Almost any of the physical properties that are responsive to phase changes may be useful in phase diagram studies. Electrical resistivity, thermal expansion, magnetic susceptibility, percentage of elongation – all can be measured at varying compositions and temperatures, with varying degrees of difficulty, and used to define phase boundaries.

Like lattice parameters, electrical resistivity changes substantially with a composition change in the solid solution. Unlike lattice parameters, the electrical resistivity does not

remain constant in a two-phase field. It approximates the average resistivity of the mixture.

In practice, the resistivity of a series of alloys is measured either at the temperature of investigation or after quenching from this temperature. The resistivity is then plotted as a function of composition at fixed temperature or as a function of temperature at fixed composition. In both cases the inflections on the resistivity curves will correspond to bivariant boundaries. The arrests of the temperature-resistivity curves will correspond to univariant transformations.[10]

2.1.2.2 Phase Identification

2.1.2.2.1 Diffusion Couples/Triples

The diffusion couple technique is a valuable experimental tool in phase diagram research. It is widely used for the investigation of binary phase diagrams, but a modified diffusion couple technique can be used for investigation of multi-component phase diagrams.

The solid state diffusion couple technique brings two metals in close contact so that each can diffuse into the other. The annealing temperature and time should be selected such that all equilibrium phases have time to form. Because the solid state diffusion is relatively slow and diffusion coefficients may not be known for some phases, however, the appearance of all equilibrium phases is not guaranteed.[13]

Given sufficient time at a sufficiently elevated temperature, a diffusion-controlled interaction in a multiphase binary system will result in a diffusion zone with single-phase product layers separated by parallel interfaces in a sequence dictated by the corresponding phase diagram. The reason for the development of only straight interfaces with fixed composition gaps follows directly from the phase rule. Three degrees of freedom are required to fix temperature and pressure and to vary the composition.

15

The use of solid-state diffusion couples in phase diagram studies is based on the assumption of local equilibria in the diffusion zone. This means that the binary solid-solid diffusion couple can have only single-phase regions. Two-phase regions are reduced to infinitely thin layers called diffusion zones. The diffusion zone is in thermodynamic equilibrium with the neighboring single-phase layers. Figure 2-10 illustrates a hypothetical binary phase diagram and a corresponding diffusion couple with a concentration gradient of component B.
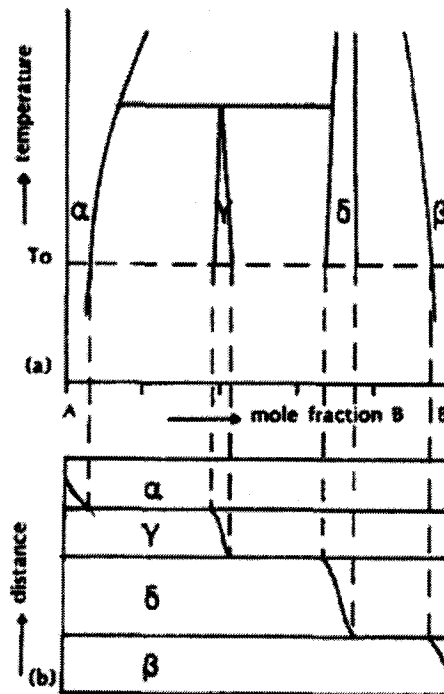
Figure 2-10 – (a) Hypothetical binary phase diagram and (b) the diffusion couple[10]
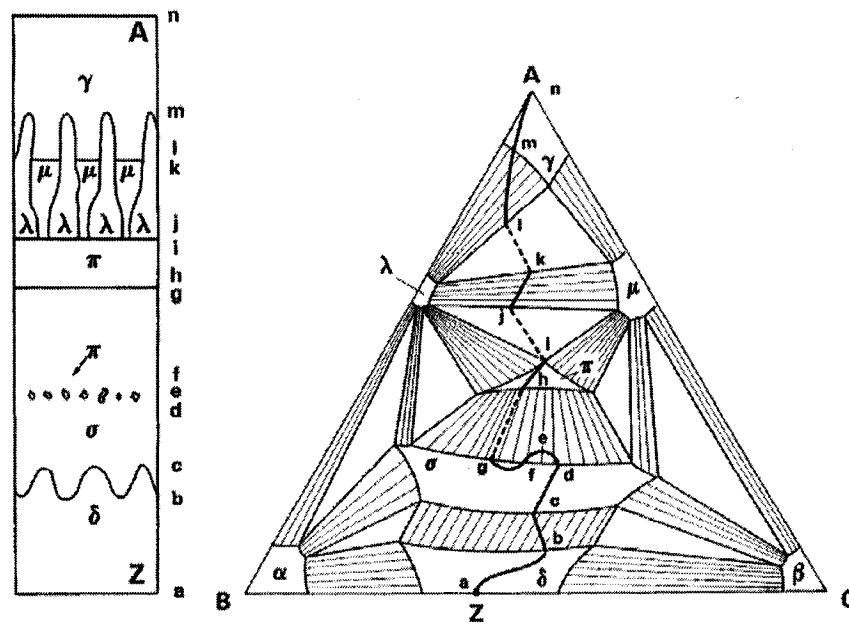
Figure 2-11 - A zone structure in a diffusion couple A/Z (on the left) and the corresponding diffusion path plotted on the isotherm of the ternary diagram (on the right).[14]

Figure 2-11 depicts a reaction zone structure and corresponding diffusion path in a hypothetical A-B-C system. The lower case letters relate the structure to the appropriate composition on the isotherm. (Note: all paths in three-phase fields are denoted by dashed lines, as a three-phase layer cannot form in a ternary diffusion couple.)

In order to obtain information about the phase equilibria existing in a system at a specified temperature, the phase boundaries within the diffusion zone have to be measured. A number of error sources may appear when multiphase diffusion experiments are employed for constructing isothermal cross-sections. The difficulties connected with concentration measurement at the interfaces and problems associated with the formation of a quasi-equilibrated diffusion zone are discussed in Kodentsov et al.[14]

2.1.2.2.2 X-Ray Diffraction (XRD)

X-ray diffraction is one of the main methods for the detection and characterization of intermetallic phases. The instrument commonly used is an X-ray powder diffractometer.

An X-ray diffraction pattern is unique to a particular element or compound, and even to a specific crystalline form of that compound. Identification of compounds is done by comparing experimental spectra with known peak locations from the literature. Results can be affected by factors such as the grain size of the material (i.e. if grain size is large, x-rays may be generated preferentially in certain orientations rather than in expected theoretical peak ratios), residual stresses, and sample angle (if not perfectly perpendicular to beam angle, Bragg angles will be distorted).

In the case of a new compound, sometimes identification can be suggested using comparison with similar compounds. However,,more often XRD is inconclusive with compounds that have not already been described in the literature.

2.1.2.2.3 Scanning Electron Microscopy

Microstructural phase analysis is often used in conjunction with x-ray phase analysis. The main applications of microstructural analysis are detection of intermetallic phases and characterization of invariant reactions. Microstructural analysis can detect the presence of intermetallic phases and also give information about the type of solidification that took place in the sample. Figure 2-12 shows an example of a micrograph displaying the characteristic lamellae of a eutectic structure.
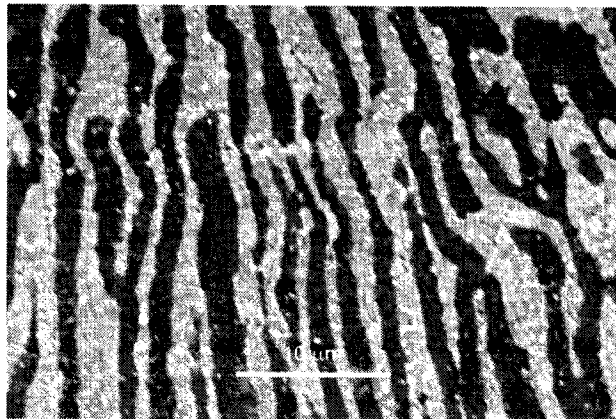
Figure 2-12 – Micrograph of near-eutectic (Bi 60, Sn 40 wt%) alloy showing fine lamellae.[15]

Peritectic alloys also display characteristic structures when examined microscopically. Unless cooled in a completely equilibrium fashion, a peritectic alloy will display a microstructure where blobs of the primary phase are surrounded by a reaction rim of the beta phase, where the primary phase has reacted with the matrix.
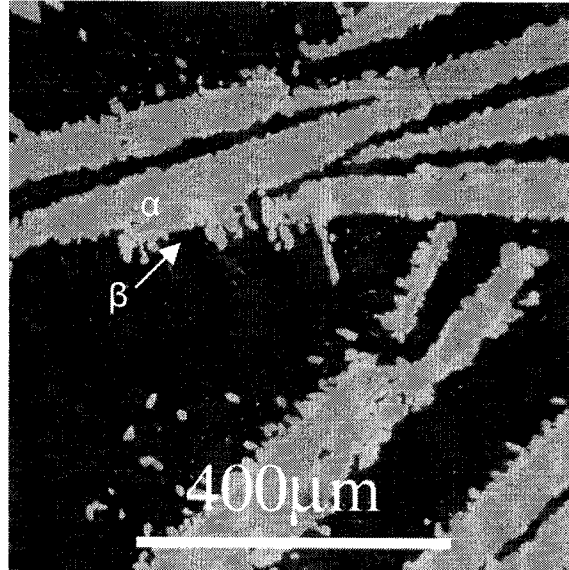
Figure 2-13 - Micrograph generated via a peritectic reaction (Cu 21, Sn 79 wt%).[15]

Figure 2-13 shows a typical microstructure of an alloy solidified through a peritectic reaction. Following the primary solidification of the α phase, the peritectic reaction occurs, and β forms from α and from the matrix. If the microstructural analysis is done using a scanning electron microscope (SEM) with energy dispersive spectroscopy (EDS) or wavelength dispersive spectroscopy (WDS) capability, quantitative analysis of the visible phases can also be performed.

2.1.2.2.4 Electron Probe Micro-Analysis

Electron probe micro-analysis (EPMA) is a qualitative and quantitative method of non-destructive elemental analysis of micron-sized volumes at the surface of materials, with sensitivity at the level of ppm. Quantification to 1% reproducibility can be obtained over several days. Elements from beryllium to uranium can be analyzed using EPMA. The

instrument uses a very stable electron beam to bombard the specimen and produce x-rays, which are then collected and analyzed via wavelength dispersive spectroscopy (WDS). The instrument normally has either four or five mono-crystals which can be set at specific Bragg angles in order to capture characteristic x-rays from different materials. There is generally also an energy dispersive spectroscopy (EDS) collector present in order to allow qualitative analysis of unknown specimens, since WDS crystals must be set at known angles and will only collect x-rays having those specific wavelengths.

The main advantages of EPMA over the EDS systems usually installed on scanning electron microscopes (SEM) are that first, the beam, although large, is extremely stable, making quantitative analysis much more accurate than with less stable beams, and second, WDS is more precise than EDS. Spectral resolution and detector dead time are much better using WDS than EDS, resulting in greater accuracy of quantitative analysis.[16]

The minimum detectable fraction of a phase is much smaller with EPMA than with XRD. In addition, the measurement of matrix composition with respect to distance from precipitates visible in the matrix can make it possible to determine whether the precipitation occurred at the annealing temperature or during the quench. Precipitation of a phase on quenching will result in a composition variation near the precipitate.[8]

2.1.2.2.5 Transmitting Electron Microscopy

Transmitting electron microscopy (TEM) uses a high voltage (120-200 keV) finely focused electron beam, which is passed through a thin (50-200 nm) solid sample. Contrast is derived by electrons scattering from atoms in the material. Figure 2-14 shows the different types of signals generated by the interaction of the TEM electron beam with the specimen material. The direct beam provides the bright field image when viewed in the image plane; the elastically scattered, or diffracted, electrons, provide dark field images, as well as diffraction patterns.
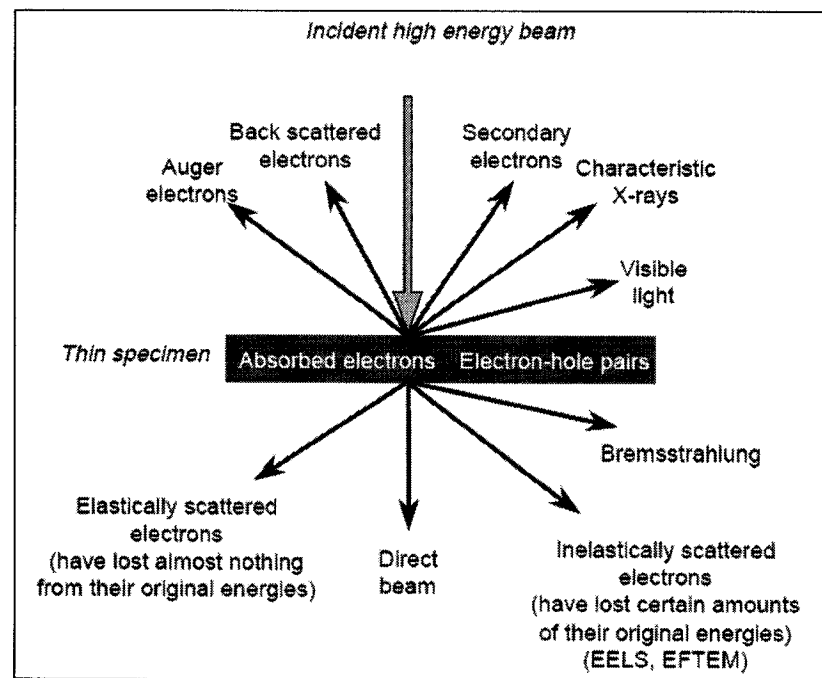
Figure 2-14 - Signals generated from thin film in transmission electron microscopy.[17]

Electron diffraction analysis using the TEM provides crystal phase identification, specimen preferred orientation information, and the determination of crystal lattice constants. Electrons diffracted from the crystal planes (in crystalline materials) form a pattern that can be measured to yield interplanar spacings, and angles between planes, in reciprocal space. Images are formed in TEM using either the transmitted electron beam (bright field) or the diffracted electron beam(s) (dark field). The electrons imaged are chosen by inserting an aperture into the back focal plane of the objective lens, thus blocking out most of the diffraction pattern except that which is visible through the aperture.[18]

The convergent-beam electron diffraction (CBED) method is used in semiconductor materials defect analysis, and in nano-phase identification in materials science generally. The method, which is often provided as a "nanodiffraction" mode on modern electron microscopes, provides transmission electron diffraction patterns from sub-nanometer areas of thin crystalline films, using a highly convergent beam, so that Bragg spots appear as discs, and it is the contents of these disks, or "rocking curves" which are

21

analyzed. The method uses the field-emission gun to produce a large number of scattered particles from a small volume of matter. CBED has traditionally been used to determine the space-group of TEM samples on a nanometer scale.[19]

All TEM techniques require exacting sample preparation. TEM provides a resolution on the order of .2nm, but in order to achieve the highest quality image, the sample must be thinned down to less than 30-40nm. Although multiple techniques are used in TEM sample preparation, Focused Ion Beam (FIB) milling provides the highest degree of accuracy in specific area sample preparation since the specimen may be viewed by secondary electron imaging while thinning.

2.1.3 Phase Diagram Calculation Methods

A useful tool to pre-select alloy composition is thermodynamic simulation. Solidification data, equilibrium phases or precipitate volume fractions are data which can be extracted from thermodynamic calculations and applied to experiments. [20]

2.1.3.1 FactSage© and Other Tools

There are several tools available to assist in the preparation of calculated phase diagrams based on thermodynamic principles. In thermodynamic optimization (as it is termed in this field) of a chemical system, all available thermodynamic and phase equilibrium data for a system are evaluated simultaneously in order to obtain one set of model equations for the Gibbs' energies of all phases as functions of temperature and composition. From these equations, all of the thermodynamic properties and the phase diagram can be back-calculated. In this way, all the data are rendered consistent with each other and with thermodynamic principles. Thermodynamic property data, such as activity data, can aid in the evaluation of the phase diagram, and conversely phase diagram measurements can be used to deduce thermodynamic properties. Discrepancies in the available data can often be identified and resolved, and interpolations and extrapolations can be made in a thermodynamically correct manner.[21]

FactSage is a software package developed by the Centre for Research in Computational Thermochemistry (CRCT) at Ecole Polytechnique de Montreal, Canada. One advantage of this package over other software applications is that it permits the use of a quasi-chemical model for the liquid mixture. In other words, short and long range ordering can be modelled, as opposed to a simple ideal mixture. If no ordering is present, this model collapses to the ideal mixture model.

Thermocalc, developed in Sweden, Pandat, developed in Madison, Wisconsin, and MTDATA, developed in the United Kingdom, all have similar functionality and databases to FactSage. Choosing between them is mainly a matter of comparing databases. As the FactSage team is currently actively developing a light metals database, this tool seems the best for magnesium applications.

2.2 Alloying Behavior of Magnesium

Hume-Rothery's criteria for extensive solid solubility between two elements encompass size similarity, electronegativity similarity, and crystal structure similarity. Each of these criteria can affect the way in which two elements behave together.

For size similarity, the atomic radii are compared. Table 2-I presents atomic radii of magnesium as well as of some alloying elements used in magnesium alloys. It should be noted that there are multiple ways to calculate atomic radius, none of which is completely accurate, due to the nature of electronic bonds. Both ionic radius and metallic radius are quoted in Table 2-I. Hume-Rothery's size criterion for predicting whether a solid solution can form between two elements is that the atomic size difference cannot be greater than 15%. Those elements falling into this category are highlighted in blue in Table 2-I.

Crystal structure is also a factor when considering which elements will alloy well together. The crystal structures of magnesium and several elements used with magnesium are shown in Table 2-I as well. Solid solutions are more likely to be extensive between elements of the same crystal structure.

Finally, electronegativity, i.e. the number of valence electrons an atom has, can also affect alloying behaviour. The lattice spacing relationsips in Mg alloys are closely related

23

to the valency of the solutes. For example, a solution of indium in magnesium causes less contraction than one of cadmium with magnesium, despite the similar atomic radii of Cd and In. There is a sharp distinction between the lattice distortion produced by solutes with valency equal to or less than Mg, and those with valency greater than Mg.[22]

Table 2-I: Atomic radii of selected elements[23]

Element	Atomic Number	Metallic rad (nm)	% Var. from Mg	Ionic rad (nm)	% Var. from Mg	Structure	
Li	3	0.152	0.00	0.078	0.00	bcc	
Na	11	0.186	22.37	0.098	25.64	bcc	
Mn	25	0.112	-26.32	0.091	16.67	bcc	
Al	13	0.143	-5.92	0.057	-26.92	fcc	
Si	14	0.117	-23.03	0.198	153.85	fcc	
Ca	20	0.197	29.61	0.106	35.90	fcc	
Ni	28	0.125	-17.76	0.078	0.00	fcc	
Cu	29	0.128	-15.79	0.096	23.08	fcc	
Ce	58	0.118	-22.37	0.182	133.33	fcc	
Th	90	0.18	18.42	0.097	24.36	fcc	
Mg	12	0.16	n/a	0.078	n/a	hcp	
Sc	21	0.16	5.26	0.083	6.41	hcp	
Zn	30	0.133	-12.50	0.083	6.41	hcp	
Y	39	0.181	19.08	0.106	35.90	hcp	
Zr	40	0.158	3.95	0.087	11.54	hcp	
Pr	59	0.183	20.39	0.116	48.72	hcp	
Nd	60	0.182	19.74	0.115	47.44	hcp	
Bi	83	0.17	11.84	0.103	32.05	rhomb	
In	49	0.157	3.29	0.091	16.67	tetra	

2.2.1 Properties of Magnesium

Magnesium is a hexagonal close-packed material. As a pure metal it is relatively soft and reactive, but many alloys have been developed which improve both the mechanical properties and the chemical properties of the metal.

Cerium and indium are the alloying elements of primary interest in the current work. Physical and chemical properties of pure magnesium, cerium, and indium are listed in Table 2-II.

Table 2-II: Properties of Mg, Ce and In

	Mg	Ce	In
Atomic Number	12	58	49
Atomic Weight	24.31	140.11	114.82
Crystal Structure	HCP	FCC	tetragonal
Space Group	hP2	Fm3m	I4/mmm
Melting Point	923 K	1068 K	430 K
Boiling Point	1363 K	3633 K	2345 K
Density at 20 °C	1738 kg/m^3	6689 kg/m^3	7310 kg/m^3
Electrical Resistivity at 20 °C	4.450 $\mu\Omega$ cm	74 $\mu\Omega$ cm	8 $\mu\Omega$ cm
Thermal Conductivity at 25 °C	155 W/mK	11 W/mK	82 W/mK
Linear Expansion Coefficient at 20 °C	25.2 x 10^{-6} K^{-1}	6.3 x 10^{-6} K^{-1}	32.1 x 10^{-6} K^{-1}

2.2.2 Alloys

The American Society for Testing Materials (ASTM) has developed a letter and number designation for magnesium alloy systems. Each alloy designation begins with two code letters, which represent the main alloying elements. The numbers following the two code letters represent the nominal composition (in wt %) of the alloying additions, rounded to

25

the nearest whole number.[24] There may be a third part, consisting of a letter of the alphabet, to distinguish between different alloys with the same percentages of the two principal alloying elements. These letters are assigned in order as compositions become standard. Finally, a fourth part of the alloy designation is reserved to indicate condition, or temper. Table 2-III lists the code letters used to indicate each alloying element. For example, AZ31 indicates an alloy containing approximately 3wt% Al and 1 wt% Zn. This nomenclature does not have any provision for indicating additional alloying elements, but does provide a good standard basis for alloy naming.

Table 2-III: ASTM code letters for use in Mg alloy names

Code Letter	Alloying Element
A	Aluminum
B	Bismuth
C	Copper
D	Cadmium
E	Rare Earths
F	Iron
H	Thorium
K	Zirconium
L	Lithium
M	Manganese
N	Nickel
P	Lead
Q	Silver
R	Chromium
S	Silicon
T	Tin
W	Yttrium
Y	Antimony
Z	Zinc

2.2.3 Alloying Elements

The mechanical properties of magnesium can be improved by the mechanism of solid solution hardening and/or second phase hardening. The reactivity of the melt, castability, corrosion properties, and microstructure can also be affected by adding various elements. The amount of alloying element that can usefully be added to magnesium is controlled by the liquid solubility of the element in the molten state, in addition to the interference between alloying elements.[24]

2.2.3.1 Existing Alloying Elements in Commercial Use

In general, an element's ability to form hardening intermetallic phases with Mg and the presence of a large field of homogeneous magnesium solid solution (Mg) on a wide range of temperature is necessary to make efficient solution treatments. A field where desired intermetallic phases precipitate at low temperatures is required to give the alloy its mechanical properties.

Aluminum is often used in magnesium, since it improves the mechanical properties and expands the freezing range, making the alloy more castable.[24]
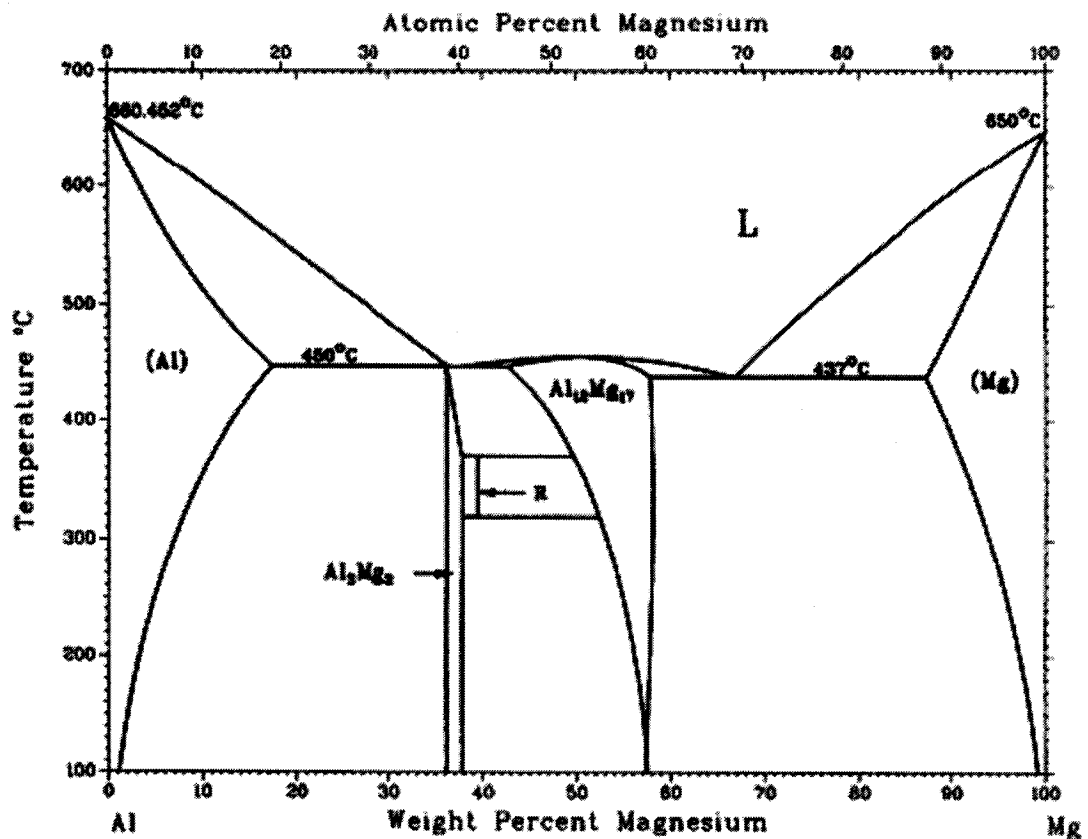
Figure 2-15 - Mg-Al binary equilibrium phase diagram.[6]

The decreasing solubility from the eutectic temperature makes it possible for the alloy to be heat treated and aged, since second phase particles will precipitate out as the alloy cools.

Calcium is often added in small amounts to grain refine the alloy and improve creep properties. It is helpful in reducing the reactivity of the melt, and also improves the rollability of magnesium sheet.[24]

Copper is added for the improvement of the high temperature strength of the alloy. Conversely, when it exceeds 0.05 wt% it decreases corrosion resistance.

Lithium has a high solid solubility in magnesium at room temperature, and at higher concentrations (11wt%) starts changing the crystal structure from HCP to BCC. This

change in crystal structure improves the formability of wrought magnesium alloys by making prismatic slip possible at room temperature.[25] Unlike most alloying additions, lithium has a lower density than magnesium, so actually improves this desirable property when added. The disadvantage is that it decreases strength and corrosion resistance.[24]

Manganese is frequently added with rare earths. Upon addition, the Mn reacts with the Fe that is present in the melt, reducing the corrosion potential of the alloy. Due to its low solubility in magnesium it can only be added up to 1.5 wt%. Mn increases yield strength, grain refinement, and weldability.

Magnesium alloys with additions of rare earth elements (RE) are very promising materials for many structural applications since they combine low density and good mechanical properties such as high specific strength, creep resistance and machinability.[20]

Historically, rare earths were usually added as mischmetal with 50 wt% cerium content, but more recently research has been focusing on the individual effect of the different rare earth metals on magnesium. Cerium in solid solution with magnesium has been found to improve the formability of wrought magnesium alloys.[22] The addition of rare earths improves the strength of magnesium at elevated temperatures, corrosion resistance, and creep resistance.

Silicon is added to magnesium to increase the fluidity of the molten metal. If Fe is present the corrosion resistance will decrease upon addition of Si.

Silver increases the high temperature strength and creep resistance of Mg alloys in the presence of rare earths. It also increases response to age hardening, thus improving mechanical properties.[26]

Like calcium, strontium has been used recently to develop creep resistant Mg alloys. One such alloy is in use in performance car engines.

In terms of castability and strengthening, zinc is as effective as aluminum.[27] It is added to magnesium with a combination of Zr, RE or thorium to produce precipitation-hardenable

materials. Alloyed only with aluminum, it increases room temperature strength. In addition, corrosive behavior of Fe and Ni is decreased with addition of Zn.

In 1937, it was discovered that zirconium has an intense grain refining effect on magnesium. The presence of zirconium gives a fine, equiaxed grain structure with typical grain sizes of 30-50 microns in sand castings. As zirconium forms stable compounds with aluminum and manganese, it can not be used to grain refine Mg-Al-Zn. The first Mg-Zr alloys contained zinc as strengthening element and subsequent alloys contained thorium, silver and most recently yttrium. Most Mg-Zr alloys contain rare earth elements such as cerium, neodymium and lanthanum, which form simple eutectic systems with magnesium and enhance castability due to formation of grain boundary networks of relatively low melting point eutectics. In addition to grain refinement, zirconium may also be used to increase the tensile strength without a loss of ductility.[27]

2.2.3.2 Other Elements

Elements as yet untried in commercial magnesium alloy development may prove to bring valuable property changes to the alloys. Indium, like aluminum, has a large solid solution area with magnesium as can be seen in Figure 2-16. In Hume-Rothery criteria terms, indium and magnesium are disposed to an extensive solid solution due to their very similar atomic radius (only 3% different), although their crystal structures are not the same, with indium being tetragonal and magnesium hexagonal. The third criterion, electronegativity, also points to an extensive solid solubility of indium in magnesium, as indium is trivalent, and magnesium is bivalent. The two are similar, and a lower valency atom will dissolve a higher valency one for bond stability.

Despite the decreasing solubility from the eutectic temperature, second phase hardening is unlikely to be a useful mechanism for this alloying element due to the high solubility even at room temperature, combined with the high density of indium, similar to that of zinc. Adding 40 wt% of indium to a magnesium alloy would result in an alloy no longer notably lightweight.

In-Mg
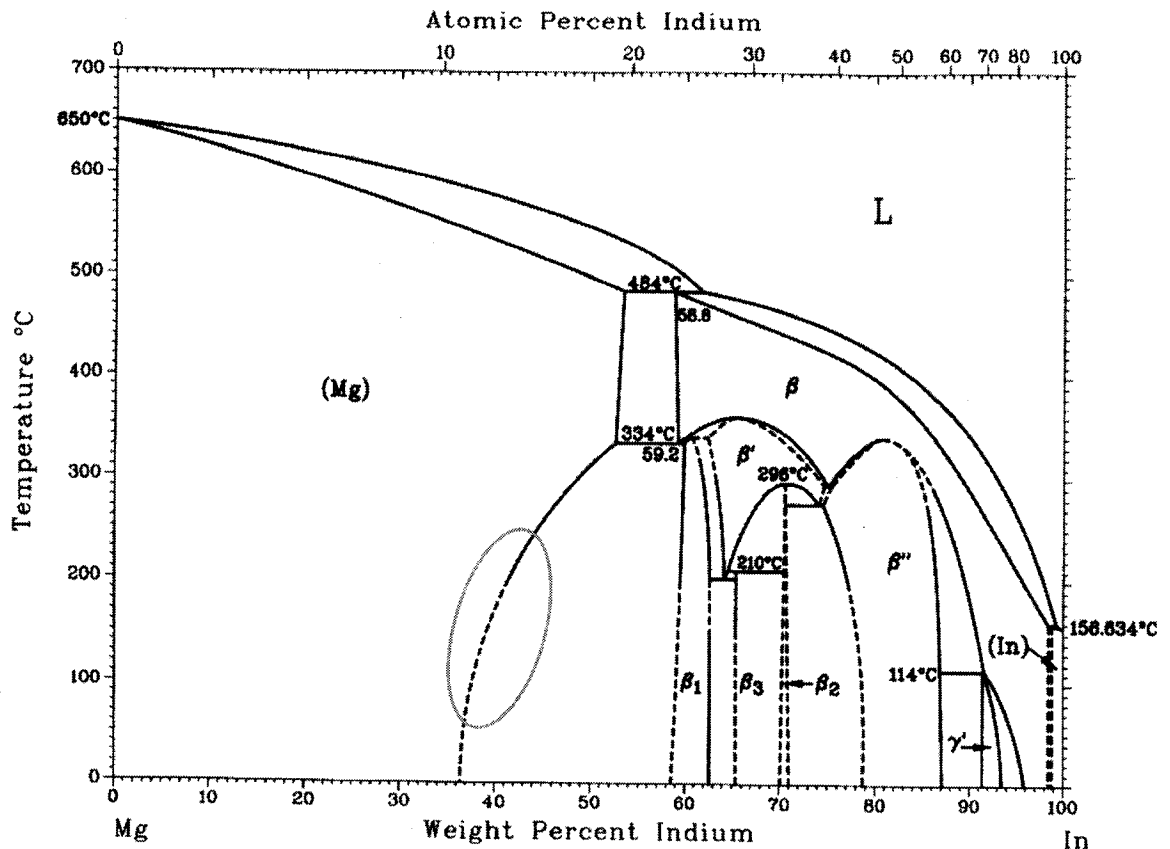
Figure 2-16 - Mg-In binary equilibrium phase diagram.[6]

2.2.4 Mg-Ce-In Alloy System

There are five basic groups of alloy systems that are currently being used in commercial application and they are based on the major alloying elements: aluminum, zinc, manganese, rare earths (RE), and zirconium.[24]

The ternary system of Mg-Ce-In has not as yet been studied. The literature contains information on the three binary systems Mg-Ce, Mg-In and Ce-In, and several binary compounds exist (see Table 2-IV). No ternary compounds have yet been reported.[28] In addition to the Mg-In phase diagram shown in Figure 2-16, binary phase diagrams also exist for Mg-Ce (see Figure 2-17) and Ce-In (see Figure 2-18).

31

Table 2-IV: Known binary compounds in the Mg-Ce-In system

Compound	Structure Type	Pearson Symbol
$CeIn_3$	Cu_3Au	cP4
$CeIn_2$	KHg_2	oI12
Ce_3In_5	Pu_3Pd_5	oS32
? Ce_9In_{11}		
? Ce_5In_4		
Ce_2In	Ni_2In	hP6
Ce_3In	Cu_3Au	cP4
CeMg	CsCl	cP2
$CeMg_{12}$	$ThMn_{12}$	tI26
$CeMg_2$	$MgCu_2$	cF24
$CeMg_3$	BiF_3	cF16
$Ce_{1.7}Mg_{17.6}$	$Ce_{1.7}Mg_{17.6}$	hP44
Ce_5Mg_{41}	Ce_5Mg_{41}	tI92
$Mg_{0.1}In_{0.9}$	Cu	cF4
$Mg_{1.2}In_{2.8}$	Cu_3Au	cP4
MgIn	CuAu	tP2
Mg_2In	Mg_2In	hP9
Mg_5In_2	Mg_5Ga_2	oI28
Mg_3In	Mg_3In	hR48

Ce-Mg
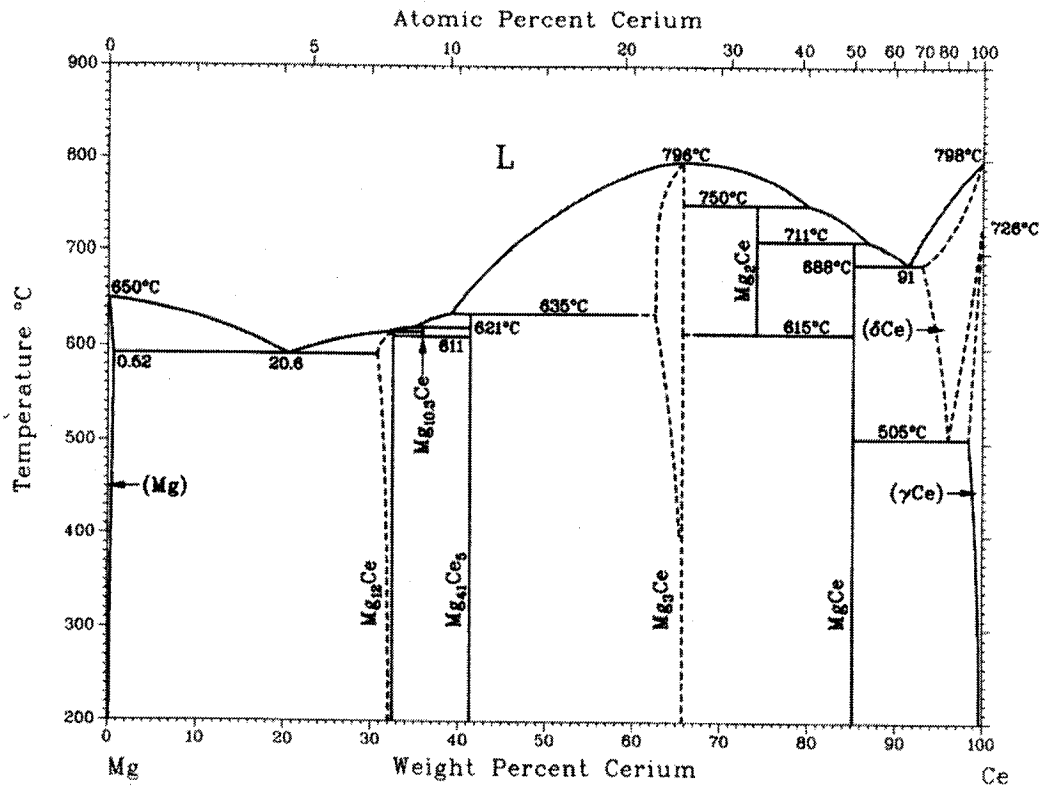
Figure 2-17 - The Mg-Ce binary equilibrium phase diagram. [6]

Ce-In
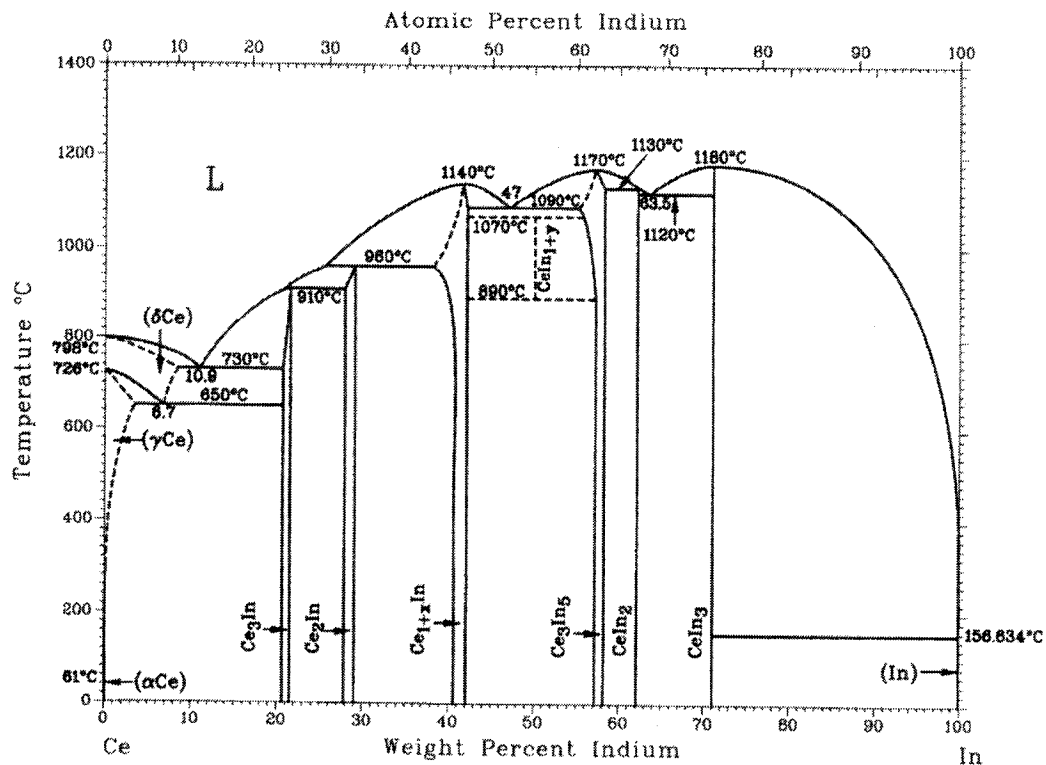
Figure 2-18 - The Ce-In binary equilibrium phase diagram. [6]

These phase diagrams are the result of the work of numerous researchers over the years. The Bulletin of Alloy Phase Diagrams gathered and evaluated all work done on these binary systems and chose the most consistent and reliable data to create the diagrams.[3,4]

2.2.5 Alloy Preparation Techniques and Challenges

2.2.5.1 Diffusion Couple Preparation

Several techniques are available to make solid-state diffusion couples, i.e. to bring two (or more) materials in such intimate contact that each diffuses into the other. In the most commonly used procedure, the bonding faces of the couple components are ground and

polished flat, clamped together and annealed at the temperature of interest. This is problematic with Ce due to its high reactivity in air. A technique was developed[29] in which a freshly polished Ce slice is immersed in molten Mg at just above the Mg melting point, so that the melt solidifies around the Ce almost instantly. This greatly improves the contact area. The assembly is then sectioned and encapsulated under vacuum in a quartz tube to prevent oxidation. Indium presents a different problem, specifically that due to its very low melting point (157°C), it can't be diffused in its pure state at any temperature above approximately 140°C, to avoid the risk of it melting.

Depending upon the initial materials, various ambient atmospheres in the furnace can be used (e.g. vacuum, inert gas, etc.). After the heat treatment, quenching of the sample is desirable in order to freeze the high-temperature equilibrium.

Electrolytic and electroless plating techniques can also be used, as well as other plating techniques such as plasma spraying and chemical vapour deposition. It is also possible to create a multiphase diffusion couple by annealing a substrate material in a reactive gas atmosphere.[14]

2.2.5.2 Preparation of Annealed/Quenched Samples

When preparing samples for determination of high temperature phase equilibria, each sample must be heat treated according to its probable position in the phase diagram. In other words, samples presumed to require solid diffusion to reach full equilibrium must be held at temperature for a long time, if one solid must form from another. An alternative is to do a two-step equilibriation wherein the sample is first brought to liquid state and quenched to avoid the formation of any crystalline solid, and then heated to temperature and the solids allowed to form directly from the amorphous state.[8]

2.2.5.3 Synthesis of Intermetallics

Once several alloys have been made and analyzed, compounds of interest may be discovered. In order to effectively study these, it is useful to make samples consisting only or mainly of these compounds. This may offer challenges related to potentially much

higher melting temperatures and/or the reluctance of some elements to dissolve completely. One method for producing intermetallic compounds in some systems is synthesis. The synthesis of intermetallic compounds can be carried out through a repeated cold-pressing technique for binary metallic systems whose large negative heat of formation ensures the solid state reaction. In some cases, those reactions get started on the surface of highly energized regions, called hot spots.

2.2.5.4 Contamination of Alloys

Due to the reactive nature of magnesium at high temperatures and of cerium at any temperature, preventing oxidation is an important consideration in producing oxide-free samples. The use of a glove bag during XRD powder preparation is a helpful technique, as small particles are otherwise extremely likely to oxidize, if not combust.

Initial pure metals used in making the alloys also need to be of very high purity. If impurities exist in the starting materials, they may well concentrate in certain phases in the alloys, leading to anomalies in the phase diagram creation. Zone refining can be used to produce highly pure metals from commercial-grade metals. In this technique, a molten zone traverses a long ingot of impure metal or chemical. The molten region melts impure solid at its forward edge and leaves a wake of purer material solidified behind it as it moves through the ingot. The impurities concentrate in the melt, and are moved to one end of the ingot.

3 Experimental Methodology

3.1 Alloy Preparation

Alloys were prepared using 99.98% pure magnesium (Mg) from Timminco Metals, Inc., containing 30 ppm Si; 99.997% pure indium (In) from Teck Cominco, containing <10 ppm Si; and 99.626% pure cerium (Ce) from Hefa, containing an average of 180 ppm Si. Chemical compositions of the raw materials can be seen in Table 3-I, Table 3-II, and Table 3-III. Ce was stored under mineral oil to prevent oxidation.

Table 3-I: Chemical composition of Mg

Element	Al	Zn	Mn	Fe	Ni	Cu	Si	Pb	Ca	Sn	Cd
ppm	40	40	21	22	3	2	30	10	10	10	10

Table 3-II: Chemical composition of In

Element	Al	Be	Ca	Ce	Cu	Fe	K	Mg	Ni	Pb	Pr	Si
ppm	<10	<10	<10	<10	1	<10	4	3	1	2	1	<10

Table 3-III: Chemical composition of Ce

RE Metal (ppm)	La	Pr	Nd	Sm	Eu	Gd	Tb	Dy	Ho	Er	Tm	Lu	Y
	320	150	430	10	2	5	2	5	1	1	1	1	10
Non-RE Metal (ppm)	Si	Fe	C	Ni	Al	Mg	O	Ca	Ta	Mo	Mn	W	N
	180	1050	450	50	420	50	115	50	50	210	25	100	50

3.1.1 Dilute Alloys

To prepare the dilute alloys in the Mg-rich corner of the ternary Mg-Ce-In system, a charge of approximately 600 g was calculated for each sample. The magnesium was placed in a mild steel crucible and melted in a Lindberg Blue M electrical resistance furnace (shown in Figure 3-1 and schematically in Figure 3-2) under a flow of protective CO_2 – 0.5% SF_6 gas. When the magnesium was molten, alloying additions were made, beginning with indium (where present) at 670°C and followed by cerium (where present) at 685°C once indium was incorporated. The melt temperature was then raised to a casting temperature of 740°C and held for fifteen minutes to allow cerium dissolution. Stirring took place shortly before casting in order to homogenize the melt as much as possible.
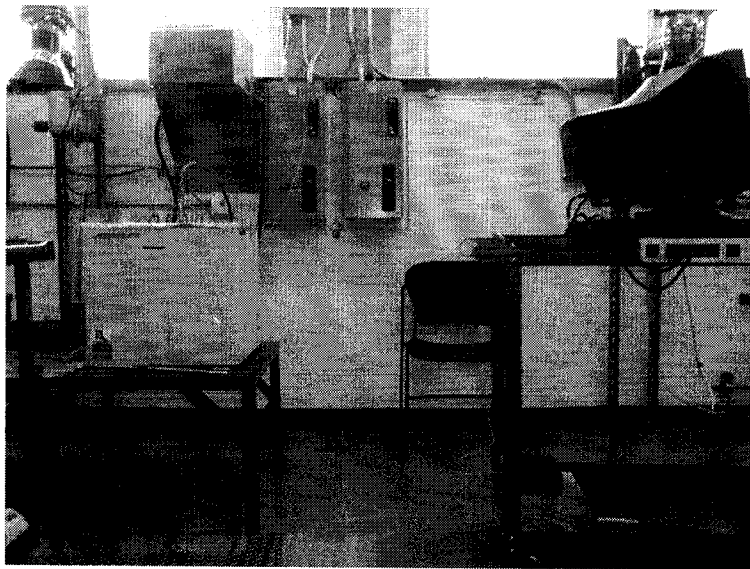
Figure 3-1 - Lindbergh Blue M electrical resistance furnace with data logging setup
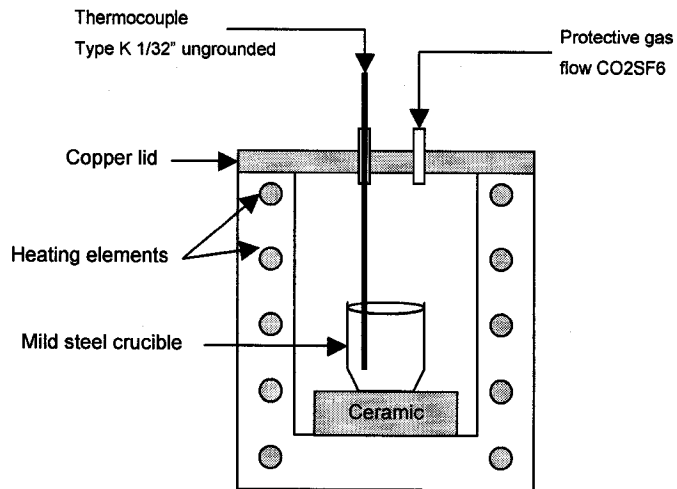
Figure 3-2 - Schematic representation of alloy preparation setup

The alloys were cast into small ingot molds under protective gas. As can be seen in Figure 3-3, the cast ingots were sectioned in six pieces. These pieces were used in pairs to produce three thermal analysis samples of approximately 200 g each. The compositions examined can be seen in Table 3-IV.
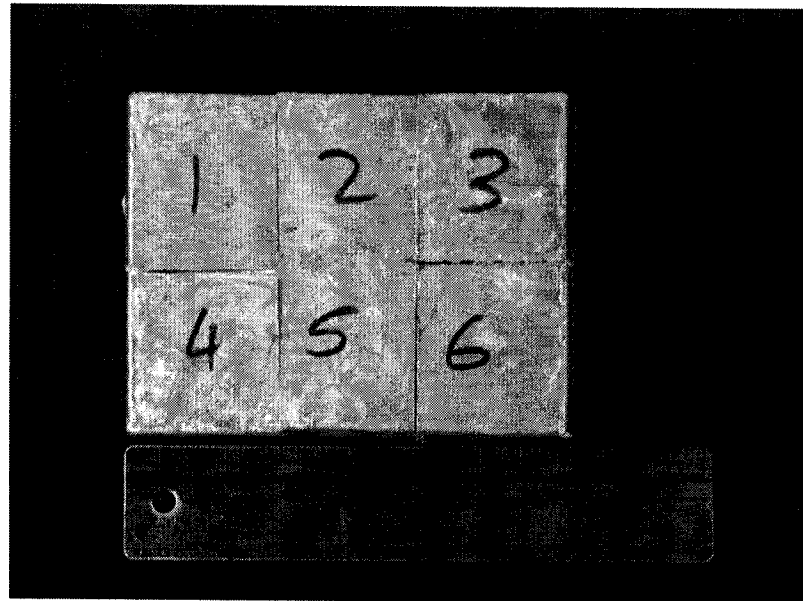
Figure 3-3 - Sectioned ingot.

Table 3-IV: Chemical Compositions of the dilute alloys prepared

Trial ID	Sample ID	Mg wt%	Mg at%	Ce wt%	Ce at%	In wt%	In at%
MIC-04	$Mg_{99}Ce_{.3}In_{.4}$	96.39	99.28	1.59	0.28	2.02	0.44
MIC-05	$Mg_{99}Ce_{.2}In_{.4}$	96.93	99.38	1.05	0.19	2.02	0.44
MIC-06	$Mg_{99}Ce_{.1}In_{.4}$	97.48	99.48	0.54	0.09	1.99	0.43
MIC-07	$Mg_{99}Ce_{.3}In_{.2}$	97.44	99.51	1.55	0.27	1.01	0.22
MIC-08	$Mg_{99}Ce_{.2}In_{.2}$	97.94	99.6	1.1	0.19	0.96	0.21
MIC-09	$Mg_{99}Ce_{.1}In_{.2}$	98.42	99.68	0.57	0.1	1.01	0.22
MIC-10	$Mg_{99}Ce_{.3}$	98.76	99.78	1.24	0.22	0	0
MIC-11	$Mg_{99}Ce_{.2}$	98.97	99.82	1.03	0.18	0	0
MIC-12	$Mg_{99}Ce_{.1}$	99.48	99.91	0.52	0.09	0	0
MIC-13	$Mg_{99}Ce_{.3}In_{.6}$	95.61	99.09	1.46	0.26	2.94	0.64
MIC-14	$Mg_{99}Ce_{.2}In_{.6}$	96.09	99.18	0.86	0.15	3.06	0.67
MIC-15	$Mg_{99}Ce_{.1}In_{.6}$	96.45	99.25	0.48	0.09	3.07	0.67
MIC-16	$Mg_{99}In_{.6}$	97.12	99.38	0	0	2.88	0.62
MIC-17	$Mg_{99}In_{.4}$	98	99.57	0	0	2	0.43
MIC-18	$Mg_{99}In_{.2}$	98.96	99.78	0	0	1.04	0.22

3.2 Synthesized Alloys with High In and Ce Concentrations

Alloys with high concentrations of In and Ce were prepared using an induction furnace (see Figure 3-4). It was found that the high reactivity of these alloys was better suited to the shorter melting and alloying time possible using the induction furnace. In addition, the induction furnace crucible is enclosed in a quartz tube flushed constantly with protective gas, which provides somewhat better protection against burning than the electrical furnace chamber. Rather than casting, these alloys were cooled in the crucible in which they were prepared.

Trial ID	Sample ID	Mg wt%	Mg at%	Ce wt%	Ce at%	In wt%	In at%
MIC-21	$Mg_{62}Ce_{21}In_{17}$	23.7	62.18	45.5	20.71	30.8	17.11
MIC-22	$Mg_{90}Ce_{5}In_{5}$	63.3	90.04	20	4.93	16.7	5.03
MIC-23	$Mg_{84}Ce_{6}In_{11}$	50	83.58	20	5.8	30	10.62
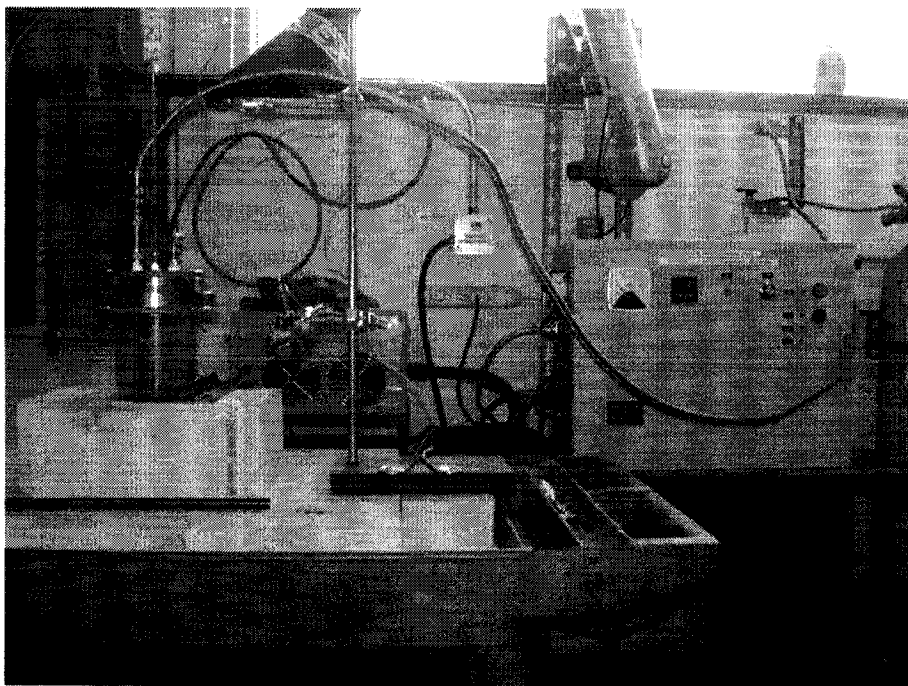
Figure 3-4 - Induction melting set-up in Mg lab.

3.3 Thermal Analysis

Cooling curve analysis was used to study the phase equilibria in the Mg-rich corner of the Mg-Ce-In system (Figure 2-17). Thermal analysis was performed in a Lindberg Blue M electrical resistance furnace using mild steel crucibles, under protective $CO_2 - 0.5\%$ SF_6 gas.

41

Type K thermocouple

Grant Squirrel 2020 Data Logger

Melt

Crucible

Computer
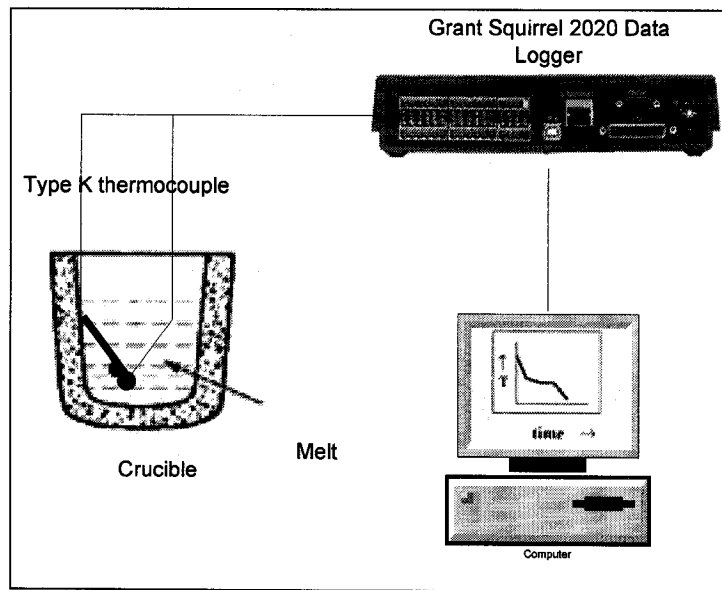
Figure 3-5 - Experimental setup for acquiring cooling curves

The thermal analysis setup, as seen in Figure 3-5, consisted of an Omega 0.8 mm ungrounded type K (chromel-alumel) thermocouple inserted into the melt with stainless steel sheathing to protect the thermocouple, connected to a Grant Squirrel SQ2020 data acquisition system. The thermocouple was positioned halfway between the center of the crucible and the side in order to minimize the likelihood of the thermocouple encountering a shrinkage pore. Thermocouples were tested before use to ensure that calibration was within stated limits. Thermocouple calibration tests were done using pure magnesium. In all cases, melting temperature determined experimentally was within 1°C of theoretical melting temperature.

The melt remained in the mild steel crucible inside the furnace throughout the cooling cycles. To slow the cooling rate, FibreFrax high-temperature insulating material was used to insulate the metal lid of the furnace as shown in Figure 3-6. This resulted in initial cooling rates ranging from 6 to 8 °C/min.
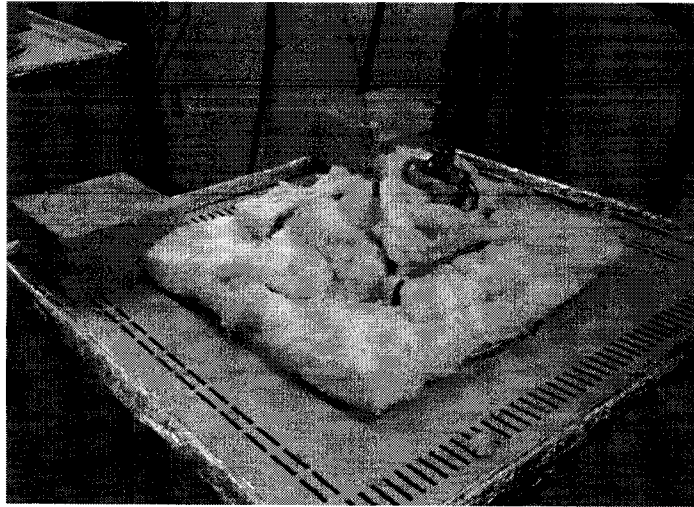
Figure 3-6 - Furnace with insulation and thermocouple

The Grant Squirrel SQ2020 data acquisition device was chosen due to its high signal-to-noise ratio. The SQ2020 has a resolution of up to six significant digits and analog-to-digital conversion at 24 bits. Cooling curves were recorded at a sampling rate of 10 Hz. It is recommended when doing thermal analysis that the sampling rate be at least 2 to 3 times the cooling rate in °C/sec. The rate used well exceeds this guideline. SquirrelView software made by Grant Instruments was used to record the data and convert it into Excel format. Liquidus points were determined by taking a maximum in the first derivative curve. Further arrests were also determined in this way, where they appeared.

The first derivative was acquired using an average of 20 data points and the formula dy/dx. Data were first manipulated to give a constant temperature interval rather than a constant time interval, as this was found to give more precision where temperature drop was very slow, i.e. during the liquidus plateau, without retaining unwieldy amounts of data during faster cooling segments of the curve. This manipulation was done using an unpublished Pascal code program.[30]
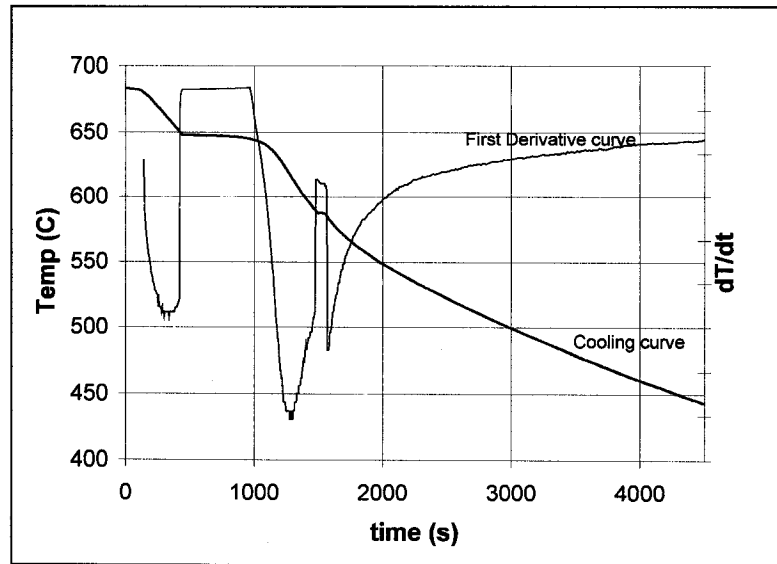
Figure 3-7 – Sample cooling curve and first derivative of a Mg alloy

Three experiments were carried out for each composition to confirm reproducibility. Liquidus and other arrest temperatures given in results section represent the average of three trials for each composition, except where trial failure left fewer values to average. Standard deviations are included with values to indicate the degree of error in the repeats. Errors associated with thermocouples are usually +/- 1°C but can range as high as +/-2°C.

In addition to cooling curve analysis, thermal analysis was performed using a Setaram SetSys Evolution combination thermogravimetric analysis (TGA)-DTA/DSC apparatus in DSC mode (see Figure 3-8). Before use, the Setaram was calibrated using three pure metals: indium, zinc, and aluminum. Only selected alloys were tested using this instrument.

Crucibles used were Al_2O_3 with lids (see Figure 3-9). Sample sizes ranged from 25 mg up to 80 mg. Setaram SetSys Evolution software was used both for calibration and to identify onset temperature, peak temperature, and enthalpy (i.e. area under the peak). Due to lack of repeatability of enthalpy values both in calibration and in testing, these values were discarded.
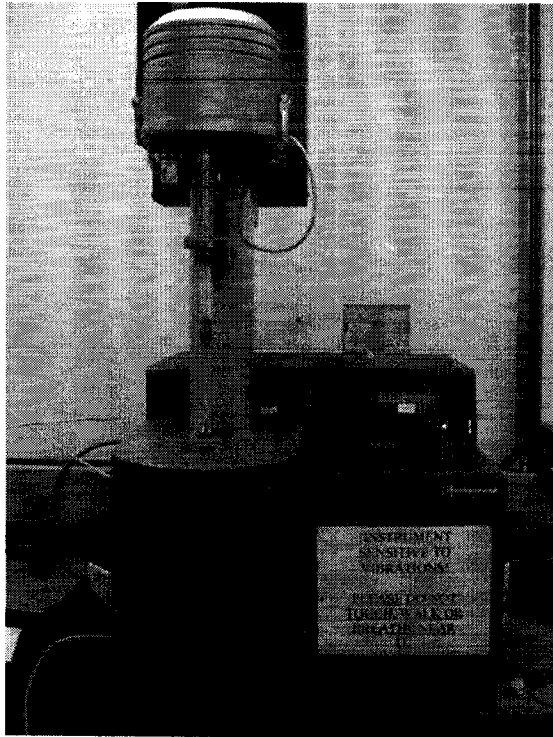
Figure 3-8 - Setaram TGA-DTA/DSC apparatus.
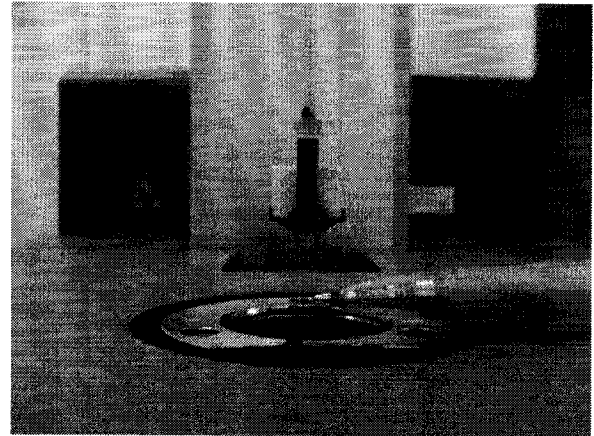
Figure 3-9 - Alumina lidded crucibles used in DSC analysis (pen included for scale).

3.4 Diffusion Couples

A diffusion couple consisting of one side pure Ce and the other side an alloy of Mg with 4.16 at% In was constructed using the liquid-solid method. The alloy was synthesized in a mild steel crucible in the electrical resistance furnace under protective CO_2-0.5%SF_6 gas, and removed from the furnace when the melt temperature was 680°C, approximately 50° over the liquidus point of this alloy.

The Ce piece, approximately 1 cm x 0.4 cm x 1.5 cm, ground to 1200 grit on both sides for good liquid-solid contact, was dropped into the melt, which rapidly solidified. After sectioning, it was determined that an area of good contact had formed at the bottom surface of the Ce piece. The diffusion couple was wrapped in Ta foil and placed in a

quartz tube which was flushed with Ar and evacuated for several cycles, and finally sealed under vacuum.

The vacuum-encapsulated diffusion couple was heat-treated at 390° for 14 days, then air quenched. The piece was mounted in conductive epoxy for EPMA and polished to 1 μm.

3.5 Microstructural Characterization

In the alloy samples, sections for metallography were taken from the region closest to the actual location of the thermocouple. The diffusion couple was sectioned perpendicular to the diffusion interface. Metallographic samples to be examined in the SEM were cold mounted in epoxy and ground and polished to 0.25 μm using silicon carbide or diamond disks for grinding and diamond paste for polishing. Silicon carbide papers of 240, 320, 400, 600 and 1200 grit were used, or alternatively diamond discs of 240 and 600 grit were used when silicon contamination was suspected. Polishing was done using diamond paste of 6 μm, 3 μm, 1 μm and 0.25 μm with extender oil on cloth discs. Ultrasonic cleaning was performed between each stage. Electron probe micro-analysis (EPMA) samples were mounted in Technovit 5000 conductive epoxy and ground and polished in the same way.

A JEOL 840A scanning electron microscope (SEM) was used to examine the metallography samples. SEM images were obtained using an accelerating voltage of 15 keV, at a working distance of 15 mm. Backscattered electron (BSE) images were preferred to secondary electron (SE) images due to the additional atomic number contrast giving compositional information. The electron dispersive spectroscopy (EDS) system attached to the JEOL 840A was used to perform standardless semi-quantitative analysis in order to determine the approximate compositions of visible phases in the samples.

Where more precise compositional information was important, EPMA was carried out, in part at General Motors Technology (Detroit) and in part at McGill using a JXA-8900L WD/ED combined microanalyzer. Samples for EPMA were mounted using conductive epoxy to obviate the need for coating samples before analysis. Both element maps and spot quantitative analyses in each visible phase were performed on each sample

46

examined. EDS and EPMA quantitative results were used to propose stoichiometry for the compounds found in the alloys.

3.6   Chemical Analysis

Chemical analysis samples were taken by drilling around the thermocouple location. 3 gram samples of the drillings were sent to Genitest Inc. for analysis using Inductively Coupled Plasma Spectrometry (ICP).

3.7   Further Phase Identification Testing – X-Ray Diffraction

X-Ray diffraction (XRD) testing was done using a Philips PW1710 powder diffractometer with a Cu Kα radiation source. XRD powder samples were prepared by filing the solid samples (under protective Ar gas for reactive samples) and mounting the powder onto a microscope slide using petroleum jelly as the binding agent (see Figure 3-10). X-ray spectra were measured at an interval of $0.04°$, measured from $10°$ to $120°$.
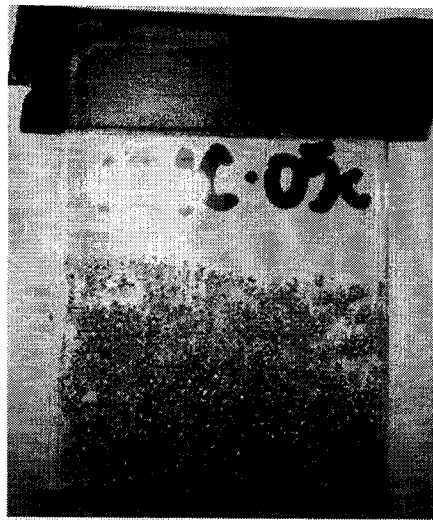
Figure 3-10 - Prepared powder sample for XRD analysis.

3.8 Annealing

Annealing of selected samples was performed in order to ensure that phases present were as close to equilibrium condition as possible. High-Ce/In samples were annealed at 175°C and 250°C for 14 days. One sample was also annealed at 500°C, but proved to be too reactive at this temperature. Samples were first wrapped in tantalum foil and enclosed under vacuum in a quartz tube, and then placed in a heat treatment furnace at the selected temperature for 14 days (see Figure 3-11. Upon removal from the furnace, samples were air cooled, then removed from the quartz tubes and sectioned and mounted for metallographic examination.
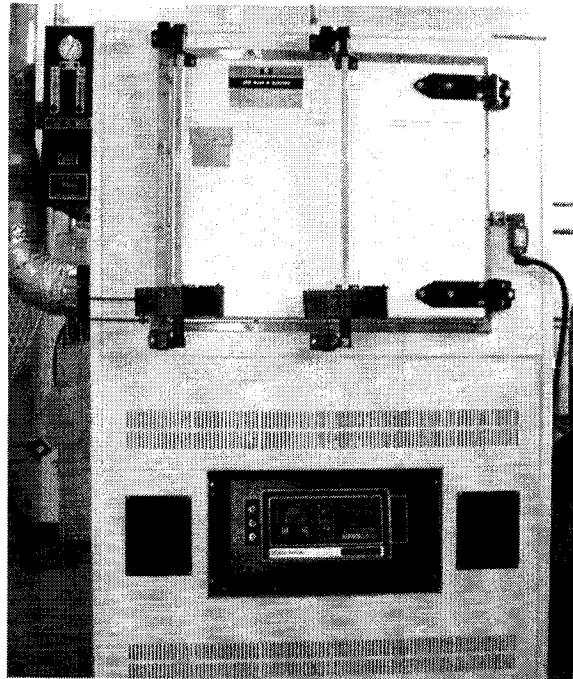
Figure 3-11 - Lindbergh heat treatment furnace in Mg lab.

3.9 FactSage©

FactSage© phase diagram calculation software was used to calculate preliminary sections of the ternary phase diagram for the Mg-Ce-In system. Since at the beginning of the work no FactSage© database entries existed for indium, the phase diagram was not calculated prior to designing the experiments, but was done afterwards.

48

4 Results and Discussion

Experimental and assessed binary phase diagrams of magnesium indium (Mg-In), magnesium-cerium (Mg-Ce) and cerium-indium (Ce-In) have been previously studied and are shown in Figure 2-16, Figure 2-17, and Figure 2-18.[6] Binary alloys of Mg-In and Mg-Ce were included in the study in order to assess the experimental method against the literature values.

4.1 Dilute Alloys in the Mg-rich Corner

4.1.1 Cooling Curve Analysis

Cooling curves of binary magnesium-indium alloys showed only liquidus and solidus inflections. No further thermal arrests appeared in the cooling curve data, confirming that only a solid solution exists in the binary composition range studied. This agrees with the existing Mg-In phase diagram (Figure 2-16). A typical cooling curve and its first derivative for a Mg-In binary is shown in Figure 4-1.
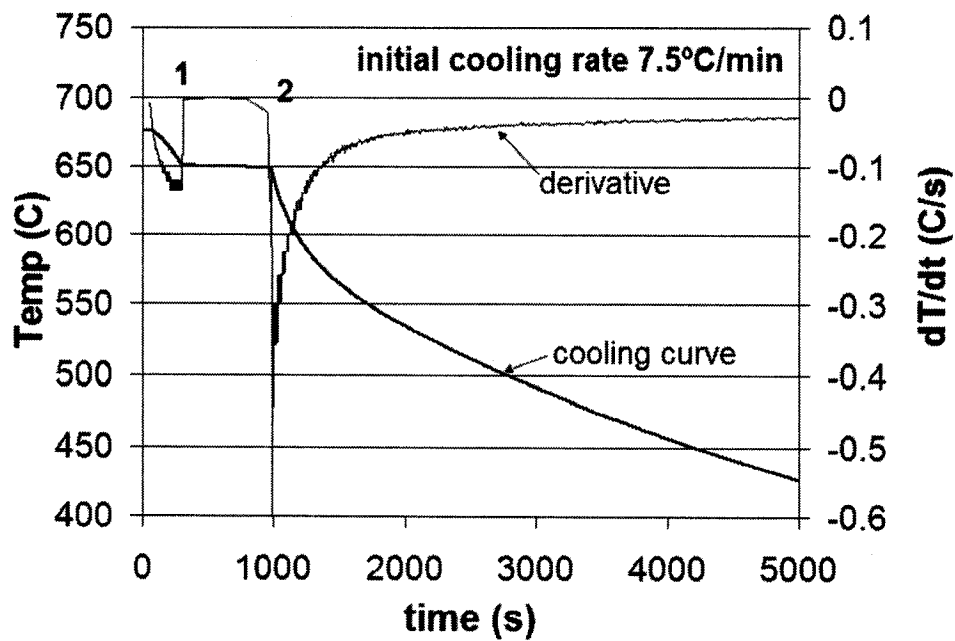
Figure 4-1 - Mg – 0.22 at% In cooling curve and first derivative curve.

The arrests visible in Figure 4-1 at points 1 and 2 represent the liquidus temperature and the solidus temperature of this alloy, and agree with those seen in the literature (see Table 4-I for temperatures of these events). The first derivative shows sharp changes in slope at the solidus and liquidus, and is otherwise quite smooth, indicating no other subtle arrests.
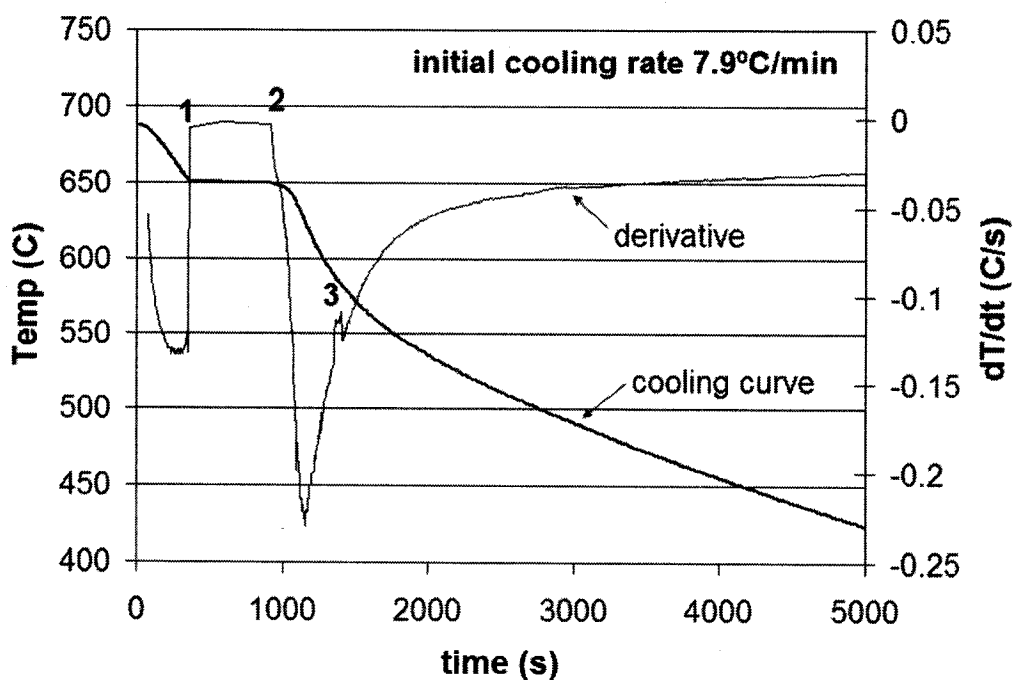
Figure 4-2 – Mg – 0.22 at% In, 0.10 at% Ce cooling curve and first derivative curve.

In contrast to the binary Mg-In alloys, magnesium-indium-cerium alloys with 0.1 at% cerium or less show an arrest around 583°C in addition to the liquidus arrest. Most of the alloy has solidified by point number 2 on Figure 4-2, when the cooling plateau ends. There is still a small amount of liquid present until the third point indicated, where a small arrest is barely visible on the cooling curve, but can be seen as a small peak on the first derivative curve. This represents the end of solidification. The microstructures for this alloy (see section 4.1.3, Microstructural Characterization of Dilute Alloys) indicate a very small amount of second phase around the grain boundaries, which agrees with the small arrest in the cooling curve.
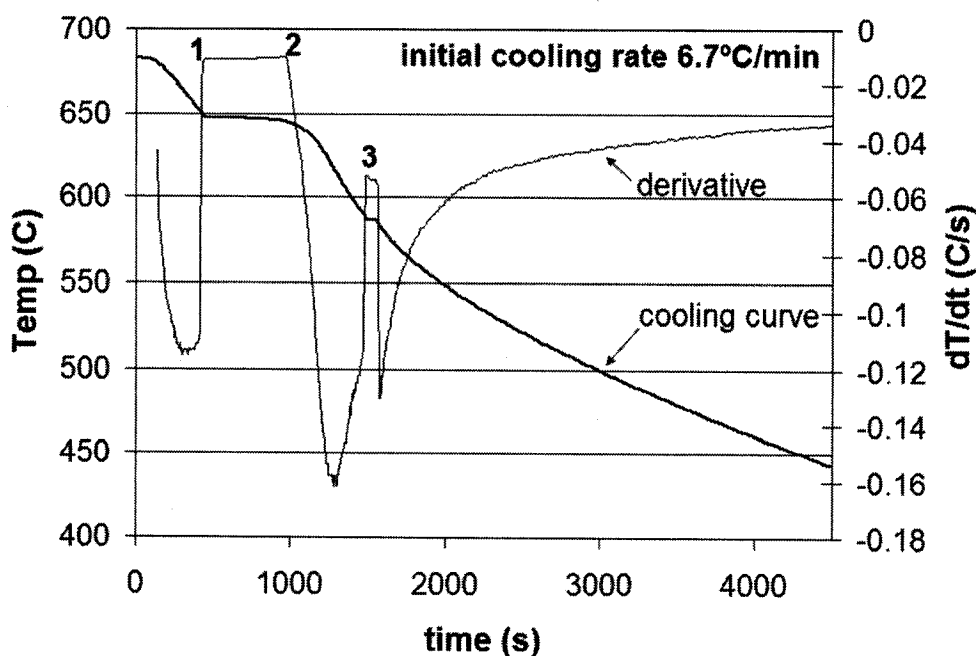
Figure 4-3 - Mg – 0.22at%In, 0.27at%Ce cooling curve and first derivative.

In alloys with 0.15-0.28 at% Ce, the additional arrest can be clearly seen on the cooling curves as well as on their derivatives in the vicinity of 583°C (see Figure 4-3). This arrest represents the end of solidification, as mentioned above in relation to the lower-cerium alloy. In addition, in both the lower and the higher cerium alloys, the arrest represents a eutectic point in the ternary Mg-In-Ce system, related to the binary eutectic in the Mg-Ce phase diagram occurring at 591±2 °C and 4.3 at% Ce (see Figure 2-17, Mg-Ce phase diagram).

Liquidus points and other arrests of all alloys measured from first derivatives of cooling curves are given in Table 4-I. The liquidus temperatures given in Table 4-I are plotted in three dimensions in Figure 4-4. Literature values for the binary liquidi are also plotted on the faces representing 0% In and 0% Ce, respectively. It can be seen that the experimental values for the binary Mg-In alloys are within 2°C of the literature values. The trend of the liquidus surface can be seen in this plot.

Table 4-I: Cooling arrests determined from first derivative curves

Ce at%	In at%	Liquidus (°C)	Other arrest (°C)
0.00	0.22	651.0±1.0	
0.00	0.43	649.9±1.0	
0.00	0.62	648.2±1.0	
0.09	0.00	650.3±0.4	588.6±1.0
0.10	0.22	650.2±0.9	583.9±0.4
0.09	0.43	647.7±1.1	577.5±3.5
0.09	0.67	647.5±1.0	584.5±1.0
0.18	0.00	650.2±0.1	591.1±0.9
0.19	0.21	648.6±0.1	585.7±0.4
0.19	0.44	646.9±1.0	582.0±1.0
0.15	0.67	647.3±0.6	580.5±0.1
0.22	0.00	649.5±1.0	591.5±1.0
0.27	0.22	647.1±0.7	586.5±0.7
0.28	0.44	645.9±0.2	583.2±0.3
0.26	0.67	645.2±0.2	581.1±0.9
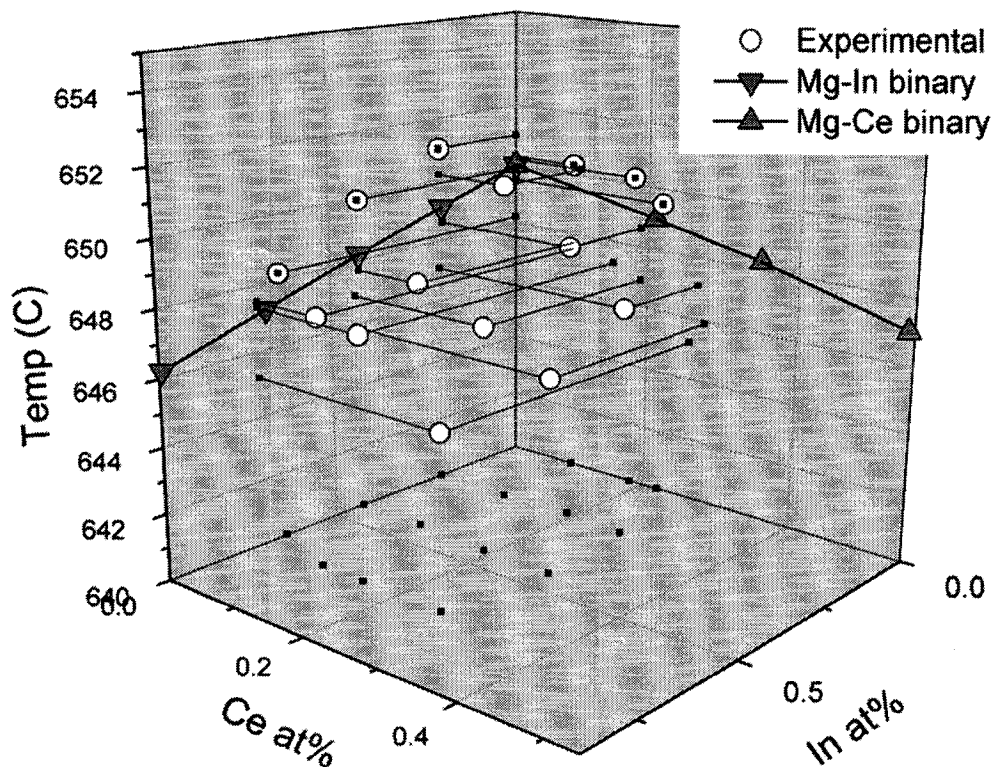
Figure 4-4- Liquidus temperatures vs. element concentration.

4.1.2 Ternary Eutectic

In addition to the liquidus arrests, an arrest at approx. 583-591°C was noted in all ternary alloys synthesized and subjected to cooling curve analysis. This arrest represents the end of solidification and the formation of the intermetallic phases. Cerium concentration has some effect on the arrest temperature, but indium concentration has a much stronger effect, as can be seen in Figure 4-5 and Figure 4-6.
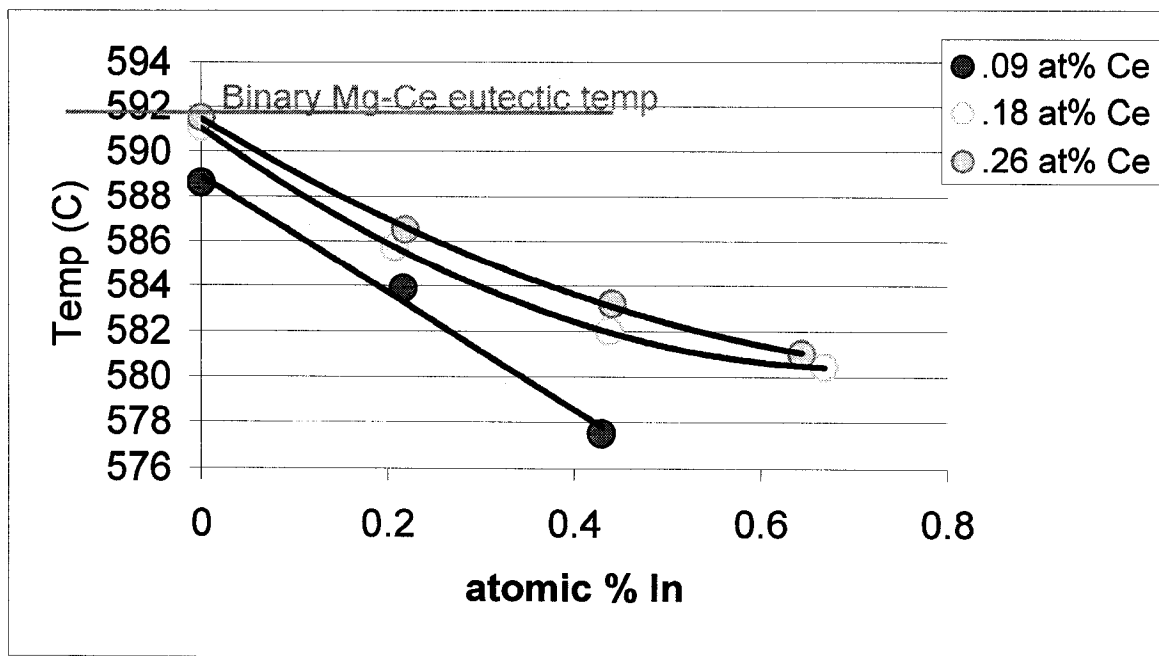
Figure 4-5 - Effect of In concentration on arrest temperature
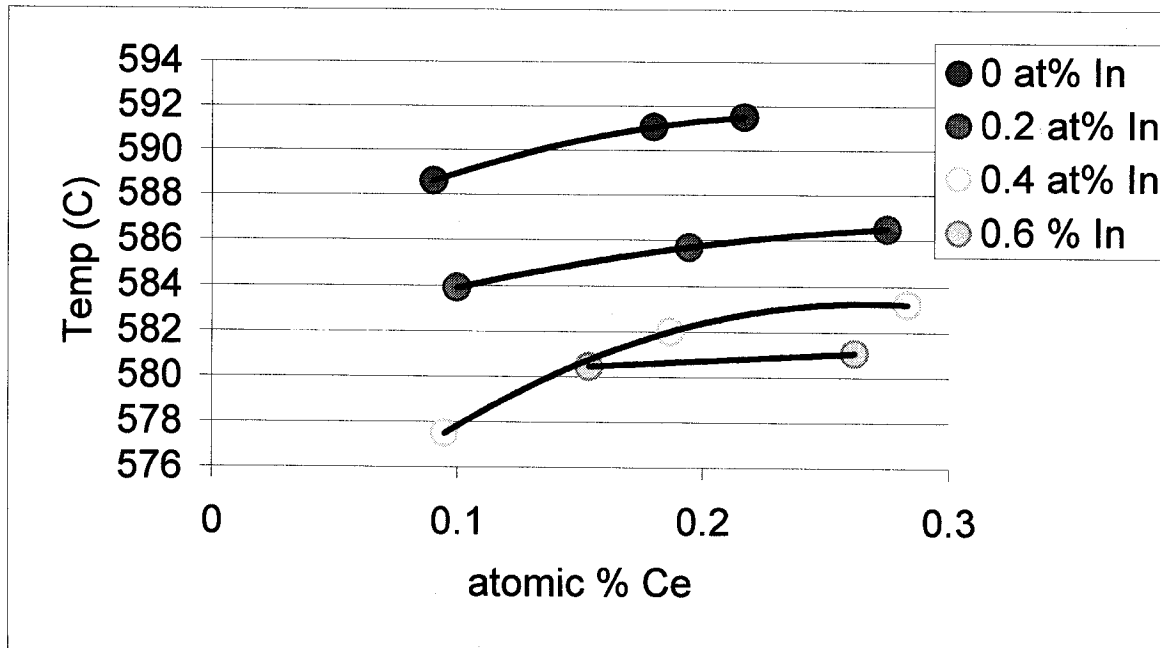
Figure 4-6 - Effect of Ce concentration on arrest temperature

Figure 4-7 shows all the measured values of the eutectic transformation temperature in the dilute alloys in a 3-dimensional form. Superimposed on the walls of the figure are the binary liquidus and eutectic lines from the corresponding literature Mg-Ce and Mg-In phase diagrams. The experimental values at 0% In correspond very well with the binary Mg-Ce eutectic line, and with increasing indium content the transformation temperature decreases, as was seen in the 2-dimensional figures above.
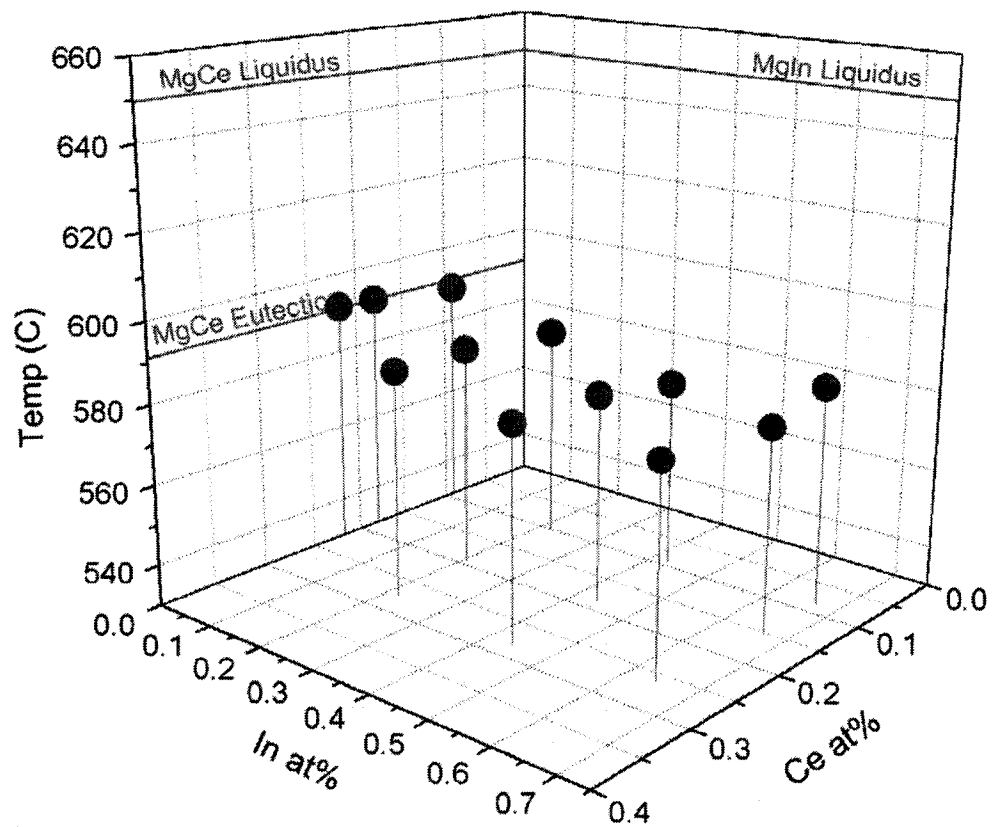
Figure 4-7 – Ternary eutectic values obtained from cooling curve analysis of dilute alloys

4.1.3 Microstructural Characterization of Dilute Alloys

In Figure 4-8, SEM BSE (back scattered electron) micrographs of the binary Mg-In alloys show no compositional contrast, but are an even grey throughout. This is consistent with the expected solid solution predicted by the phase diagram and the cooling curves.
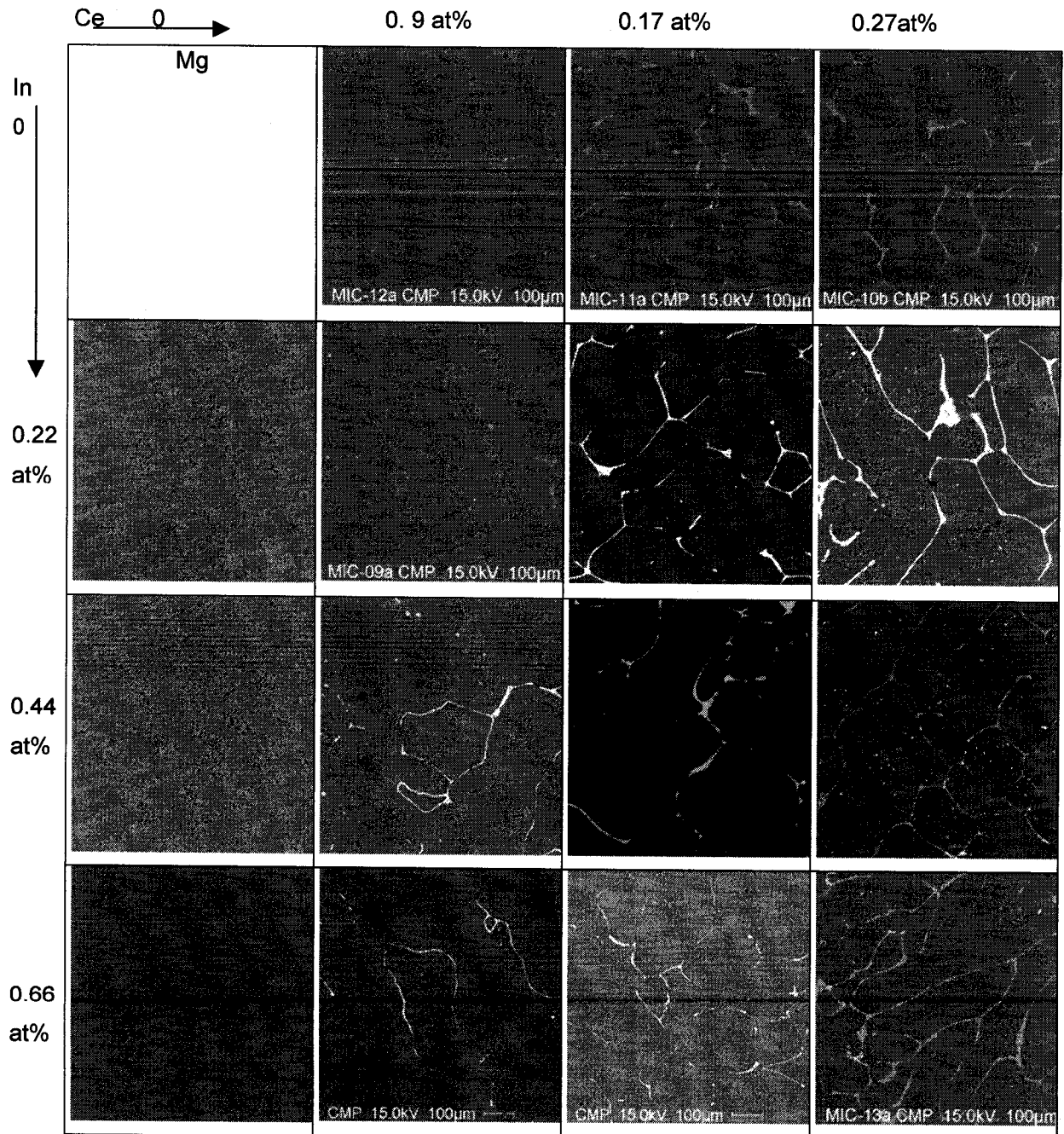
Figure 4-8 - Low magnification micrographs of dilute alloys.

With even a small amount of cerium, intermetallic compounds begin to appear as lighter areas at the grain boundaries. This indicates (in backscattered images such as these) that these compounds contain material of a higher atomic number than the surrounding matrix, i.e. high concentrations of one or both of the alloying elements, both of which have higher atomic numbers than magnesium. In general, going from lower to higher cerium (left to right across Figure 4-8) more intermetallic compound is visible. Only at higher magnifications, as shown in Figure 4-9 and Figure 4-10, can more detail of the make-up of these grain boundaries be seen.

No ternary intermetallic compounds are known to date in the Mg-In-Ce system.[28,3,4] However, SEM micrographs and EPMA of the ternary alloys studied show two potential ternary or higher level compounds. Figure 4-9 shows a grain boundary of sample $Mg_{99}Ce_{.1}In_{.4}$. Two distinct phases are present: one appearing almost white, which will be referred to as θ for the present study, and one a light grey, referred to as τ.
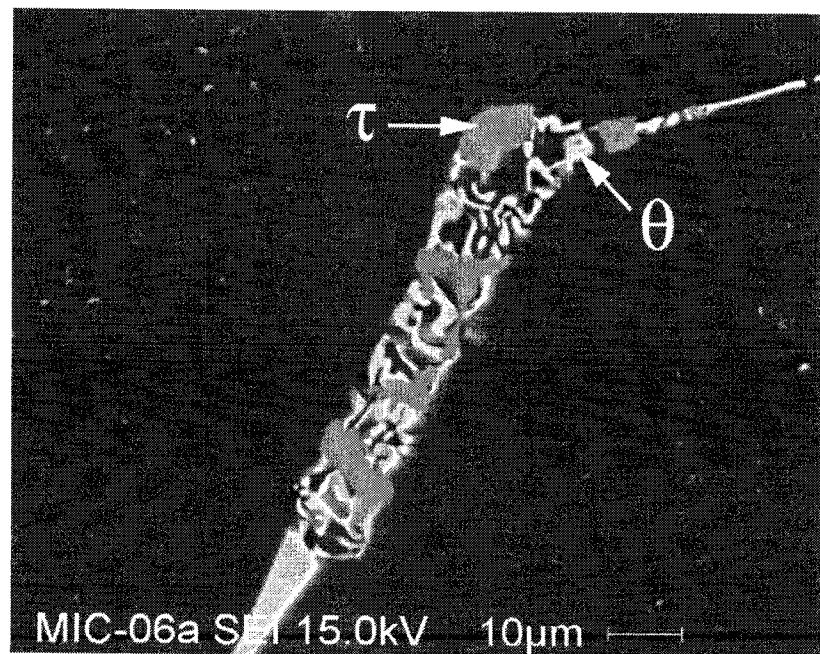
Figure 4-9 - BSE image of Mg 0.43at%In, 0.09at%Ce.

As can be seen in Table 4-II, the θ phase contains a significant amount of Si, despite only trace levels of Si present (5-20 ppm) in the bulk alloys. The Si level in the compound is not homogeneous, but can be as high as 2.8 at% where present. Since the θ phase does appear without Si (in other samples) as well as with Si, the compound does not require the presence of Si in order to form.

Table 4-II: EPMA Results for θ-phase

Bulk Ce%	Bulk In%	Ce at%	In at%	Mg at%	Si at%
0.57	1.01	19.9 ±0.4	13.4 ±0.8	65.6 ±1.4	1.0 ±1.4
0.54	1.99	20.0 ±0.3	16.5 ±0.4	62.8 ±0.6	0.7 ±0.2
1.1	0.96	19.6 ±0.2	13.0 ±0.5	64.1 ±0.6	3.3 ±0.2
1.05	2.02	20.2 ±0.2	15.2 ±0.3	62.4 ±0.9	2.2 ±1.2
1.55	1.01	20.0 ±1.0	12.9 ±1.0	64.4 ±2.1	2.8 ±0.5
1.59	2.02	19.8 ±0.3	15.6 ±0.8	63.9 ±0.8	0.7 ±0.3
1.46	2.94	20.3 ±0.1	16.1 ±0.8	61.8 ±0.8	1.8 ±1.6

Table 4-III: EPMA Results for τ-phase

Bulk Ce%	Bulk In%	Ce at%	In at%	Mg at%
0.52	0	7.4 ±0.2	0.0 ±0.0	92.6 ±0.2
0.57	1.01	7.6 ±0.1	2.2 ±0.0	90.3 ±0.1
0.54	1.99	7.3 ±0.4	2.3 ±0.1	90.3 ±0.5
1.03	0	7.6 ±0.1	0.0 ±0.0	92.4 ±0.1
1.1	0.96	7.5 ±0.1	2.1 ±0.1	90.3 ±0.1
1.05	2.02	7.6 ±0.1	2.9 ±0.0	89.4 ±0.1
1.24	0	7.5 ±0.1	0.0 ±0.0	92.4 ±0.1

In Figure 4-10, it can be seen that at ~0.27at%Ce and no indium, only the matrix and the τ phase appear. EPMA of this τ compound indicates that its composition matches to within one standard deviation the known binary $Mg_{12}Ce$ compound (see Table 4-II and Table 4-III for detailed EPMA quantitative results). This phase will henceforward be referred to as $(Mg, In)_{11}Ce$ rather than τ. Since recent studies in the Mg-Ce system[29] have indicated that this compound actually has the composition $Mg_{11}Ce$ and not $Mg_{12}Ce$, this new composition will be used.
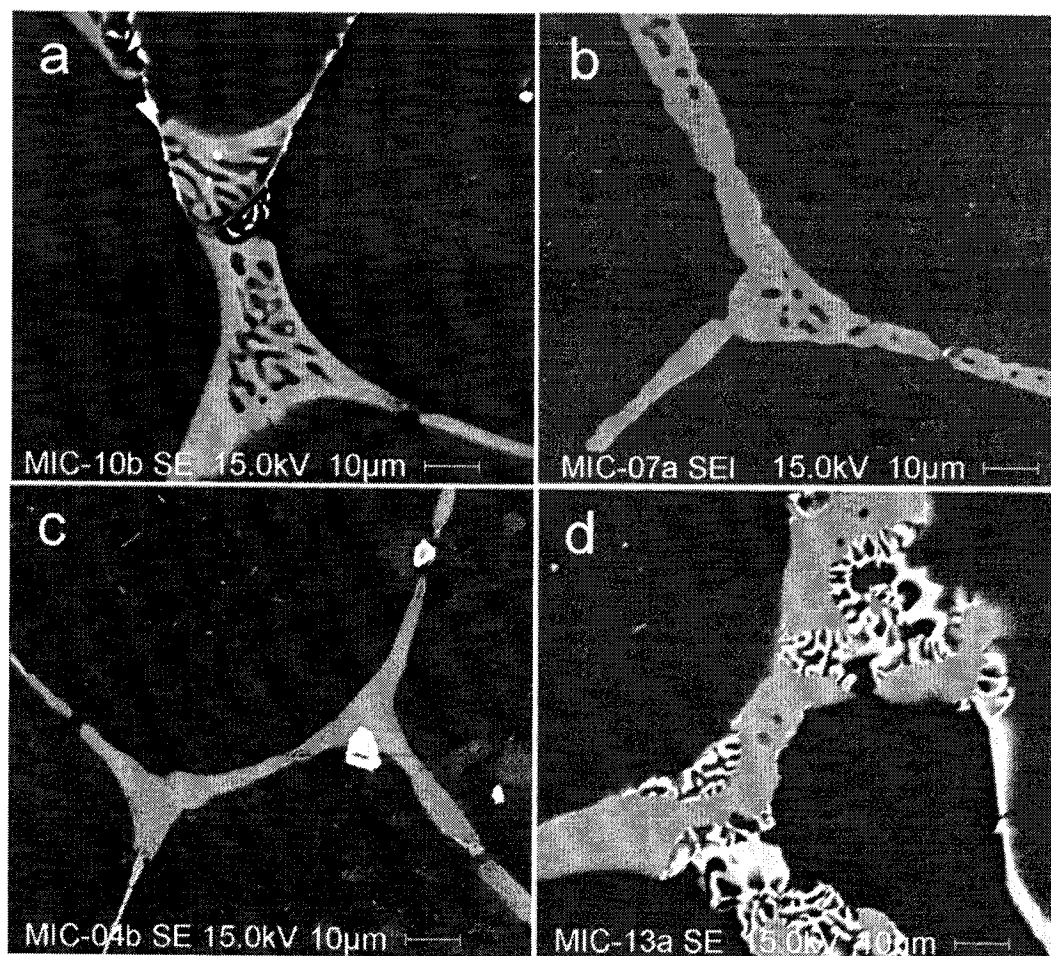
Figure 4-10 -BSE images of MgCeIn alloys with approximately 0.27at%Ce: (a) 0.00at%In, 0.22at%Ce (b) 0.22at%In, 0.27at%Ce (c) 0.44at%In, 0.28at%Ce (d) 0.64at%In, 0.26at%Ce.

Adding 0.22 at%In changes the intermetallic compound very little (see Figure 4-10 b), as the indium appears to simply replace some of the Mg in the $Mg_{11}Ce$, forming $(Mg,In)_{11}Ce$.

Further addition of In confirms this, as the Ce content of this phase remains constant while more and more Mg is replaced by In. The trend is not linear, with In at% in the compound seeming to level off at approximately 2.8 at% In.

Once In content reaches 0.44at% in the Mg0.27at%Ce series of alloys (see Figure 4-10 c), $(Mg,In)_{11}Ce$ no longer appears as a eutectic, and a second intermetallic phase begins to appear. This is the compound referred to as θ. At first, in the alloy containing 0.44at%In, it appears in very small amounts at the grain boundaries. Once the In content reaches 0.64at% (see Figure 4-10 d), however, this phase is very much in evidence at the grain boundaries, forming a eutectic structure.

Backscattered electron micrographs of the samples containing lower concentrations of Ce appear very similar to micrographs taken of higher Ce alloys, the main difference being that the grain boundary phases, though apparently similar in composition, are less plentiful and are thinner. This is consistent with the lower concentration of Ce, which appears to be the key element for the formation of the intermetallic compounds seen at the grain boundaries.

The θ phase has a very consistent Ce content of approximately 20 at%, with the other elements varying somewhat among the different alloys. Thus the compound could also be interpreted as a compound of Ce and Mg, with other elements replacing some of the Mg in a solid solution. If the Mg and In constituents of the phase (and Si where it appears) are added together, the sum is a very consistent 80.02 ± 0.46 at%, with Ce content at 19.98 ± 0.46 (atomic percentage values were normalized, so it is not significant that the values sum to 100%). The resulting proposed $(Mg,X)_4Ce$ does not correspond to any known binary Mg-Ce compound. Compositions of the phases identified at room temperature are plotted in Figure 4-11.
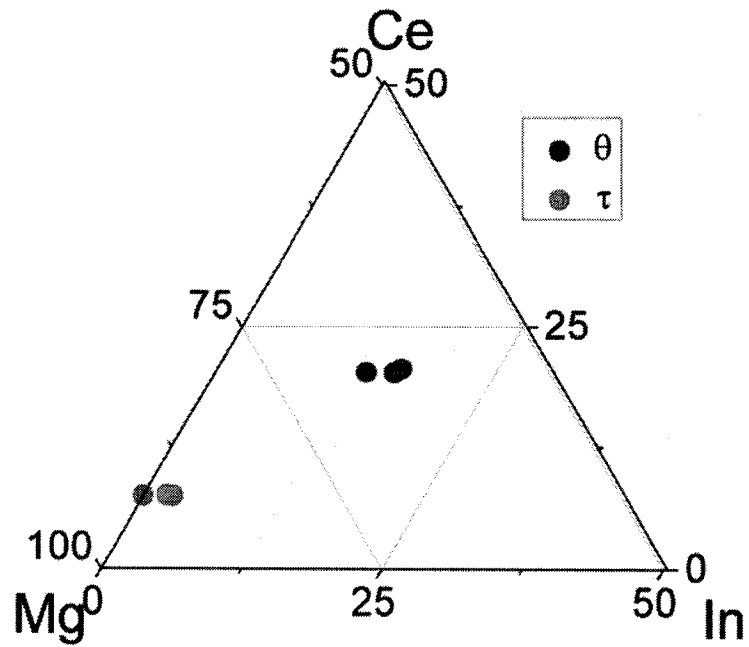
Figure 4-11 - Compositions of equilibrium room temperature phases identified in dilute ternary alloys.

Despite the slow cooling of the alloys during thermal analysis, element maps (see Figure 4-12) show that some coring may have resulted, with enrichment of grain boundaries with solutes. It cannot be assumed that equilibrium conditions have been achieved in these samples.
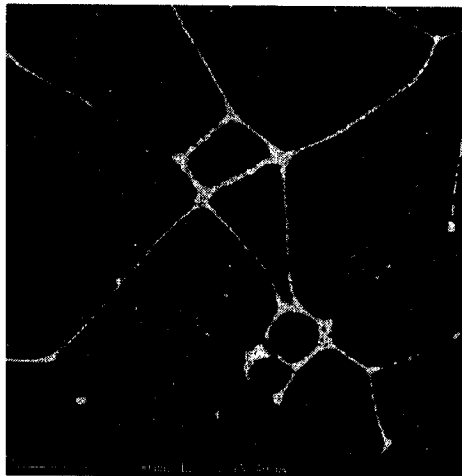
Figure 4-12 - Indium map for sample MIC-5 showing impoverishment of indium in centers of grains.

The formula for the θ compound varies from $Mg_{65}Ce_{20}In_{13}$ for alloys containing approximately 0.22 at% In, to $Mg_{63}Ce_{20}In_{16}$ for alloys containing approximately 0.43 at% In, to $Mg_{62}Ce_{20}In_{16}$ for alloys containing approximately 0.67 at% In. It can be seen that once again, as in $(Mg,In)_{11}Ce$, the variation diminishes as the total indium in the alloy increases, which may indicate that the composition is approaching the upper limit for the amount of In possible in this compound.

4.1.4 X-Ray Diffraction of Dilute Alloys

X-ray diffraction spectra of the dilute alloys studied were almost identical to pure magnesium spectra, since the volume percentages of intermetallics in the alloys are low and mostly below the detection limit of XRD. Peaks not matching the standard Mg spectrum can for the most part be attributed to the $Mg_{11}Ce$ spectrum. In Figure 4-13, the theoretical pure $Mg_{11}Ce$ spectrum has been shifted in order to match experimental peaks. This shift is due to the indium dissolved in the $Mg_{11}Ce$ compound, and is as expected.

One unknown peak does appear in several of the spectra at approximately 43° 2θ. This peak may belong to the new intermetallic compound observed in these alloys, designated as the θ compound.
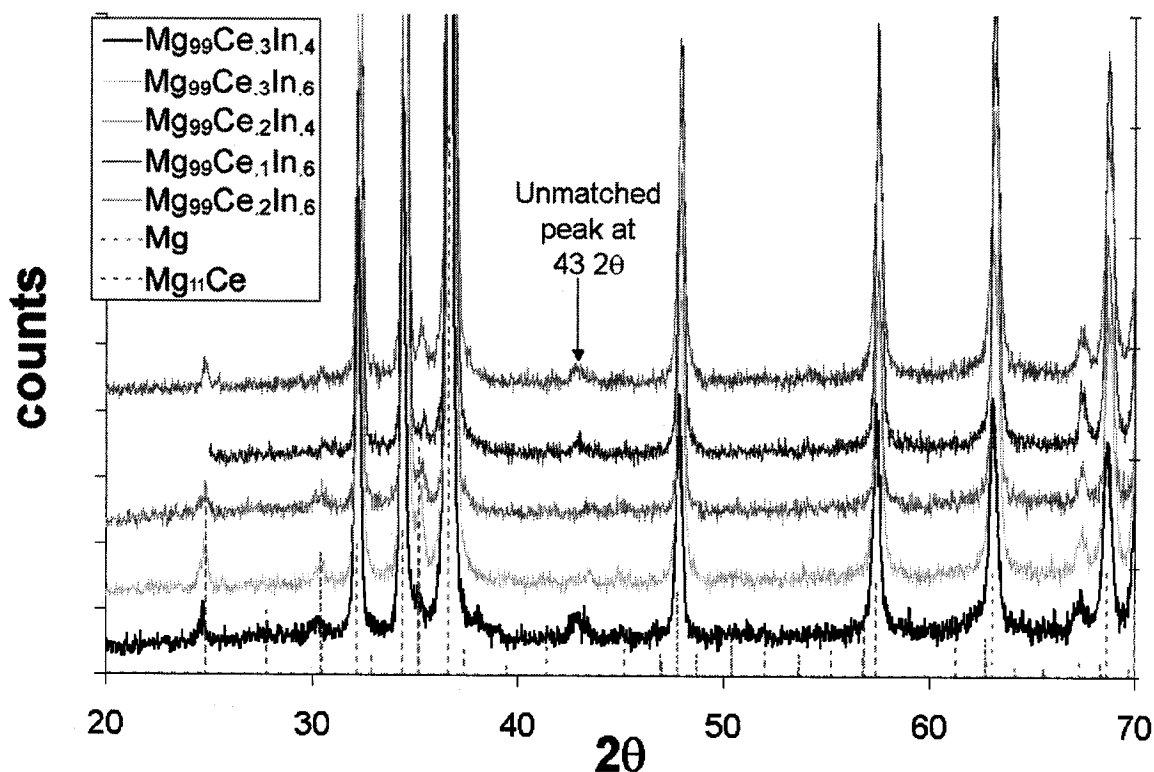
Figure 4-13 - XRD spectra from dilute Mg-Ce-In alloys.

4.2 Diffusion Couple

A diffusion couple consisting of one side pure Ce and the other side an alloy of Mg with 4.2 at% In was constructed using the liquid-solid method. Upon removal from the quartz encapsulation, the diffusion couple appeared darkened but intact, and the contact zone showed no separation or voids. The Ce-(Mg-In) diffusion couple, designated sample id MIC-20, was examined using electron probe microanalysis. The interface between the alloy and the Ce was found to have seven distinct zones, as can be seen in Figure 4-14 (note that white lines on figure are added for visual separation of zones). Comparing the zone compositions, in order, to the phases present in the Mg-Ce binary equilibrium phase diagram (Figure 4-15), it can be seen that most zones correspond well to binary Mg-Ce phases, indicating that it is likely that In is dissolved in the binary Mg-Ce phases.
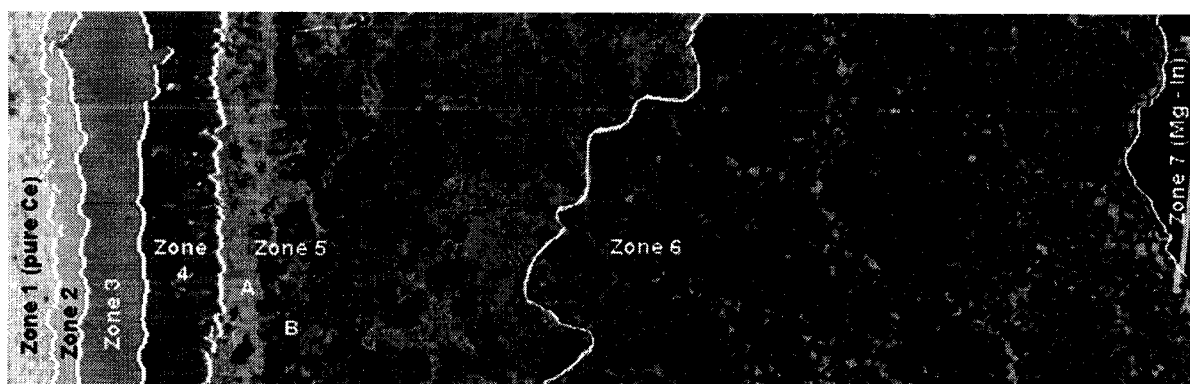
Figure 4-14 - BSE image of MIC-20 (Mg-In)-Ce diffusion couple after diffusion
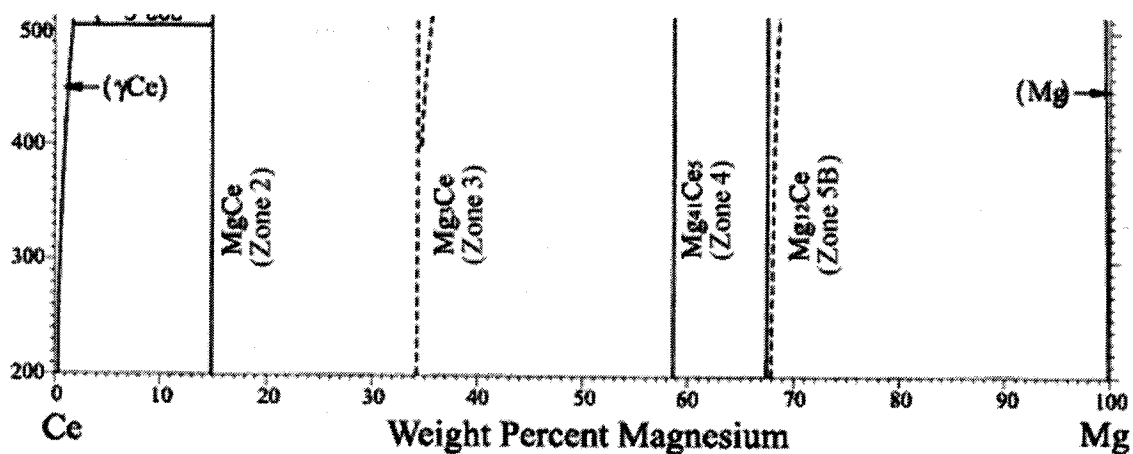
Figure 4-15 - Section of Mg-Ce binary equilibrium phase diagram.

A high oxygen content in some of the zones leads to a less accurate overall quantitative analysis, but nonetheless results for Mg and Ce concentration are very close to the stoichiometric ratios for known binary Mg-Ce compounds. Weight concentrations and standard deviations can be seen in Table 4-IV.

Table 4-IV - Weight concentrations of elements in zones of diffusion couple MIC-20

Wt %

Element	O	Mg	In	Si	Ce	Total
Zone 1	2.450	0.015	0.000	0.041	98.540	101.046
Zone 2 avg	0.757	13.482	0.913	0.011	84.690	99.853
stddev	0.192	0.185	0.461	0.014	0.213	
Zone 3 average	0.480	33.042	2.228	0.000	63.470	99.220
stddev	0.085	0.394	1.398	0.000	0.919	
Zone 4 average	0.357	55.604	1.846	0.004	41.952	99.763
stddev	0.038	0.163	0.138	0.005	0.305	
Zone 5A average	0.996	23.748	30.986	0.021	45.764	101.514
stddev	0.090	0.868	1.309	0.017	0.360	
Zone 5B average	0.469	62.456	3.548	0.004	32.602	99.080
stddev	0.237	0.612	0.688	0.004	0.182	
Zone 7 average	1.040	82.862	17.362	0.007	0.121	101.393
stddev	0.465	1.003	0.838	0.005	0.048	

An examination of the concentrations and standard deviations of indium in zones 2, 3 and 4 indicates that these values are very variable, with standard deviations ranging from about a tenth the total concentration to over half. It can be assumed that indium concentration in these zones is not dependent on stoichiometry, and simply represents whatever amount of indium happened to be dissolved in the compound. In contrast, Mg and Ce concentrations show a high degree of repeatability for these zones, indicating that their relative (and absolute) levels *are* related to stoichiometry.

The atomic concentrations of the elements, shown in Table 4-V, give information about the possible stoichiometry of the phases present. The ratio of Mg+In to Ce, shown in the last column, may indicate which zones correspond to binary Mg-Ce compounds with some percentage of In replacing Mg atoms, i.e. dissolved substitutionally.

Table 4-V - Atomic concentrations of elements in zones of diffusion couple MIC-20

	Atomic %						
	O	Mg	In	Si	Ce	Ratio Mg/Ce	Ratio (Mg+In)/Ce
Zone 1	17.84	0.07	0.00	0.17	81.92	0.00	0.00
Zone 2 avg	3.90	45.66	0.65	0.03	49.76	0.92	0.93
Zone 3 avg	1.61	73.02	1.04	0.00	24.33	3.00	3.04
Zone 4 avg	0.85	87.13	0.61	0.01	11.40	7.64	7.70
Zone 5A avg	3.80	59.70	16.49	0.05	19.96	2.99	3.82
Zone 5B avg	1.02	89.76	1.08	0.01	8.13	11.04	11.17
Zone 7 avg	1.79	94.01	4.17	0.01	0.02	n/a	n/a

Comparing the composition of the zones with known binary Mg-Ce compounds yields good matches for most of the zones, as can be seen in Table 4-VI. Zone 1 is pure Ce, with some Ce oxides which formed due to the high reactivity of Ce and the unavoidable transition through atmosphere between the encapsulation and the EPMA chamber. Zone 2 is MgCe with less than 1 at % dissolved indium. Zone 3 is Mg_3Ce with approximately 1 at % dissolved indium. Zone 4 is $Mg_{41}Ce_5$ with less than 1 at.% dissolved indium.

Zone 5 consists of an inhomogeneous mixture of two phases, identified as 5A and 5B (see Figure 4-14 for BSE micrograph showing these phases). Zone 5B corresponds to $Mg_{11}Ce$ with 1 at % dissolved indium. Zone 5A does not correspond to any known Mg-Ce binary, but does correspond to the θ phase found also in the dilute alloys.

Zone 6 is a eutectic mixture, formed when the diffusion couple was constructed using the solid-liquid method. Finally, Zone 7 matches very closely the terminal composition of the Mg-In side of the diffusion couple.

Table 4-VI - Atomic ratios of known room temperature Mg-Ce compounds

Compound	Ratio Mg/Ce	Possible match
MgCe	1.0	Zone 2 (0.93)
Mg_3Ce	3.0	Zone 3 (3.04)
$Mg_{41}Ce_5$	8.2	Zone 4 (7.70)
Unknown	-	Zone 5A (3.82)
$Mg_{11}Ce$	11.0	Zone 5B (11.17)

Comparing Figure 4-14, the micrograph of the diffusion couple, with Figure 4-15, a section of the binary Mg-Ce diagram, it can be seen that the diffusion zones formed in the same order as the binary Mg-Ce compounds present at equilibrium, with the exception of the new θ compound. Zone 6, a eutectic mixture formed at the time of the creation of the liquid solid diffusion couple, is represented by the region between the $Mg_{12}Ce$ line and the Mg-Ce solid solution region.

Figure 4-16 shows the zone compositions graphically, and makes it clear that the θ composition seen in the dilute alloys is a close match for zone 5A. The path from one zone to the next is also shown in this figure.

—
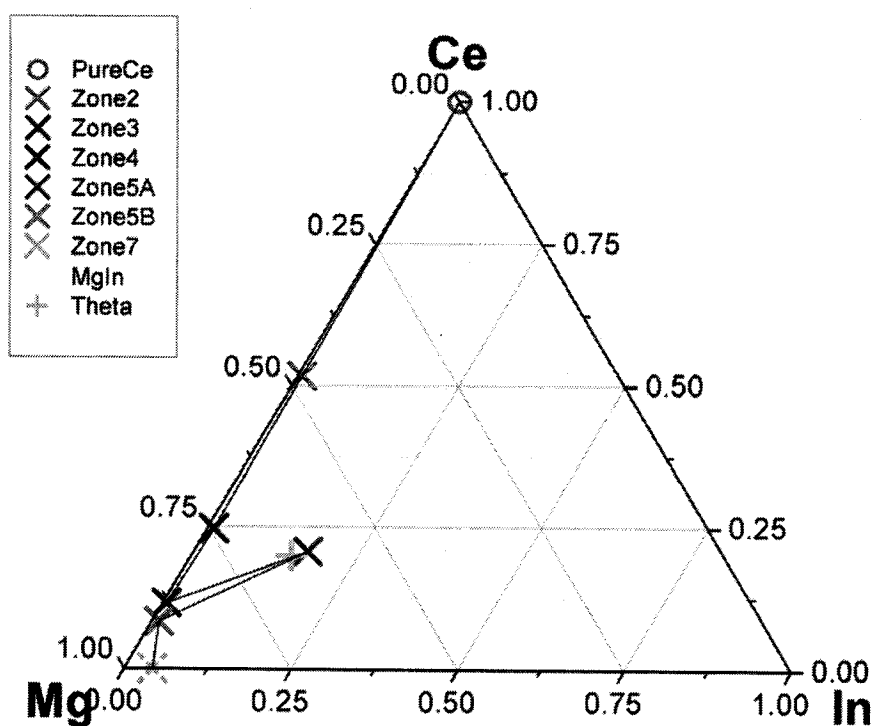
Figure 4-16 - Compositions of diffusion zones with theta compound indicated

4.3 Synthetic Alloys with High In and Ce Concentrations

In addition to the dilute alloys synthesized in the first part of the study, several alloys with much higher concentrations of alloying elements Ce and In were synthesized in order to study the intermetallic compound in more detail. Table 4-VII shows the compositions of the high In and Ce alloys as well as those of the new intermetallic compound as observed in the dilute alloys.

Table 4-VII: Compositions of alloys synthesized and of intermetallic compound observed in dilute alloys

Trial ID	Sample ID	Mg wt%	Mg at%	Ce wt%	Ce at%	In wt%	In at%
MIC-21	$Mg_{62}Ce_{21}In_{17}$	23.70	**62.18**	45.50	**20.71**	30.80	**17.11**
MIC-23	$Mg_{84}Ce_6In_{11}$	50.00	**83.58**	20.00	**5.80**	30.00	**10.62**
MIC-22	$Mg_{90}Ce_5In_5$	63.30	**90.04**	20.00	**4.93**	16.70	**5.03**
	θ	26.00	**65.09**	45.00	**19.54**	29.00	**15.37**

4.3.1 Microstructures

4.3.1.1 MIC-21

The $Mg_{62}Ce_{21}In_{17}$ (MIC-21) composition was chosen to match as closely as possible the composition of the θ phase observed in the dilute alloys. Rather than a single phase sample, a multi-phase sample was obtained, as can be seen in Figure 4-17. Four distinct phases were observed in the as-cast structure. E-probe analysis shows an additional "phase" containing high silicon (see Figure 4-18), appearing in some of the mid-gray ("b") regions of Figure 4-17. This high-Si phase has not been quantified in these samples.
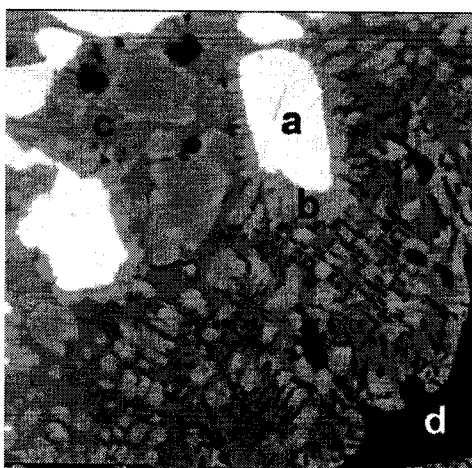
Figure 4-17 – $Mg_{62}Ce_{21}In_{17}$ alloy microstructure
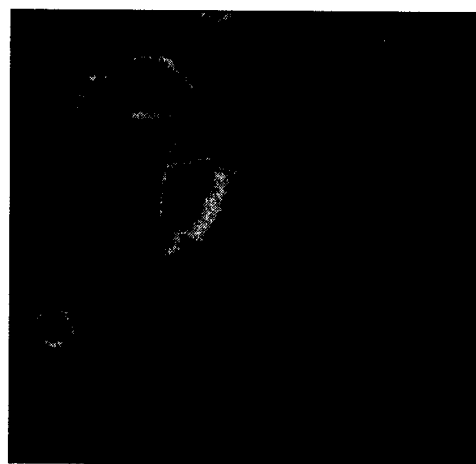
Figure 4-18 - EPMA map of Si in same region

Annealing the $Mg_{62}Ce_{21}In_{17}$ alloy resulted in a more complex series of phases, as can be seen in Figure 4-19, Figure 4-20, Figure 4-21, and Figure 4-22. Up to six distinct phases can be distinguished in the annealed samples: a, a', b, c, d, and d'.
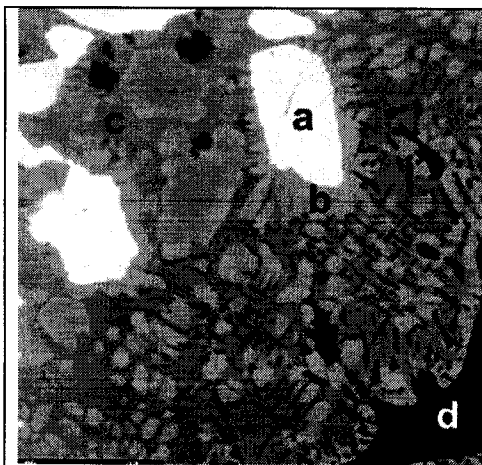
Figure 4-19 - Mg$_{62}$Ce$_{21}$In$_{17}$ as-Cast microstructure.
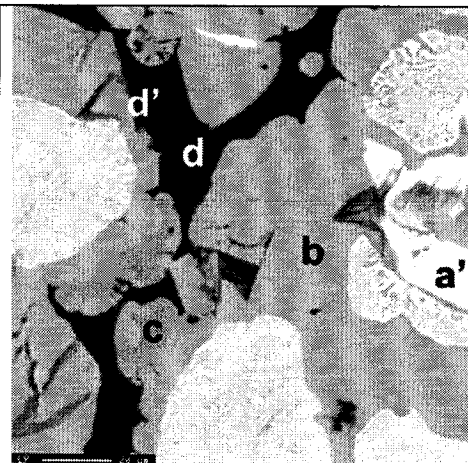
Figure 4-20 - Mg$_{62}$Ce$_{21}$In$_{17}$ annealed 175°C microstructure.
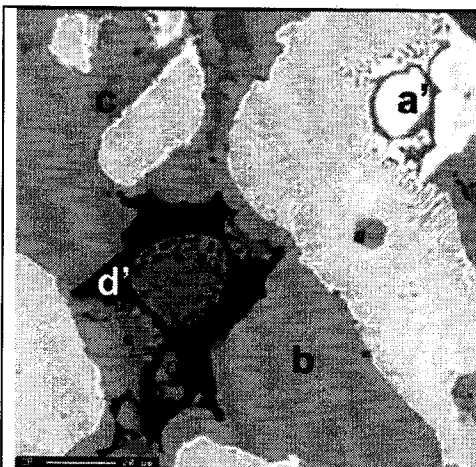
Figure 4-21 - Mg$_{62}$Ce$_{21}$In$_{17}$ annealed 250°C

Figure 4-22 - Mg$_{62}$Ce$_{21}$In$_{17}$ annealed 500°C

The compositions of these phases are shown in Table 4-VIII. The microstructure illustrated in Figure 4-19 appears to indicate a peritectic reaction with the primary phase being the white phase (designated "a" in the figures). This phase could be designated Mg$_4$Ce$_3$In$_2$, or could even be seen as (Mg,In)$_2$Ce.

In annealed micrographs, phase a becomes phase a'. Graphing the compositions as in Figure 4-23, it can be seen that with annealing, the a phase moves away from the

$(Mg,In)_2Ce$ composition it seems to have at first . Since Mg_2Ce, the corresponding binary phase, is a high temperature phase occurring only above 615°C, and the highest annealing temperature was 500°C, it is consistent with the Mg-Ce binary equilibrium phase diagram (see Figure 2-17) that this phase should disappear with annealing. The transformation from a to a' may be a eutectoid reaction

$$a + b \rightarrow a'$$
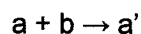
or a peritectoid reaction

$$a \rightarrow b+a'$$
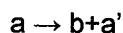
The next phase, the "b" phase, has the characteristic morphology of a peritectic. It seems to form as a result of a peritectic reaction from phase "a"

$$L + a \rightarrow b$$
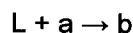
indicating that a is a primary phase that forms from the liquid.

With the composition $Mg_{65}Ce_2In_{14}$, this b phase is close to the θ phase observed in the dilute alloys. This phase concentrates Si inhomogeneously. Where present, the Si level varies from 0.25at% to a maximum of 2at%. The phase also exists with only trace Si levels. The reason for the affinity of this phase for Si is not clear. It may be that vacancies concentrate at the surface of the phase, allowing Si to segregate to these regions.

The "c" phase, with composition $Mg_{71}Ce_{22}In_6$, may be a non-equilibrium phase. It does not appear in any other samples in this study. Mg_3Ce was included on Figure 4-23 as a reference point, to show that the c phase is quite distinct from this compound, in contrast to the d phase's proximity to $Mg_{11}Ce$.

The "d" phase is the binary $Mg_{11}Ce$ with indium replacing some of the magnesium, as seen in the dilute alloys. After annealing, this phase may have disappeared or simply become very scarce. The darkest phase, d', is a α-Mg solid solution with 0.02% Ce and 0.66% In. The comparison of the micrographs shows us that the local equilibrium between b and d in the as-cast sample shown in Figure 3 is metastable for this sample composition and transforms into the local equilibrium between b and d' phases after annealing.

Table 4-VIII: Concentrations of elements in phases of as-cast and annealed $Mg_{62}Ce_{21}In_{17}$

	Mg at%	± (stddev)	Ce at%	± (stddev)	In at%	± (stddev)	Mg+In/Ce ratio	Designation
Bulk	83.6		5.8		10.6			
a	45.21	0.63	33.33	0.12	21.45	0.56	2.0	$Mg_4Ce_3In_2$
a'	33.21	0.45	34.37	0.34	32.36	0.48	1.9	MgCeIn
b	65.68	0.57	20.76	0.17	13.53	0.50	3.8	$Mg_{65}Ce_{21}In_{14}$ or θ, $(Mg,In)_4Ce$
c	71.32	1.65	22.47	0.89	6.20	0.91	3.4	$Mg_{71}Ce_{22}In_6$
d	89.31	0.89	8.28	0.23	2.41	1.06	11.1	$(Mg,In)_{11}Ce$
d'	99.27	0.22	0.07	0.05	0.66	0.21	n/a	Mg solid solution Mg(Ce,In)
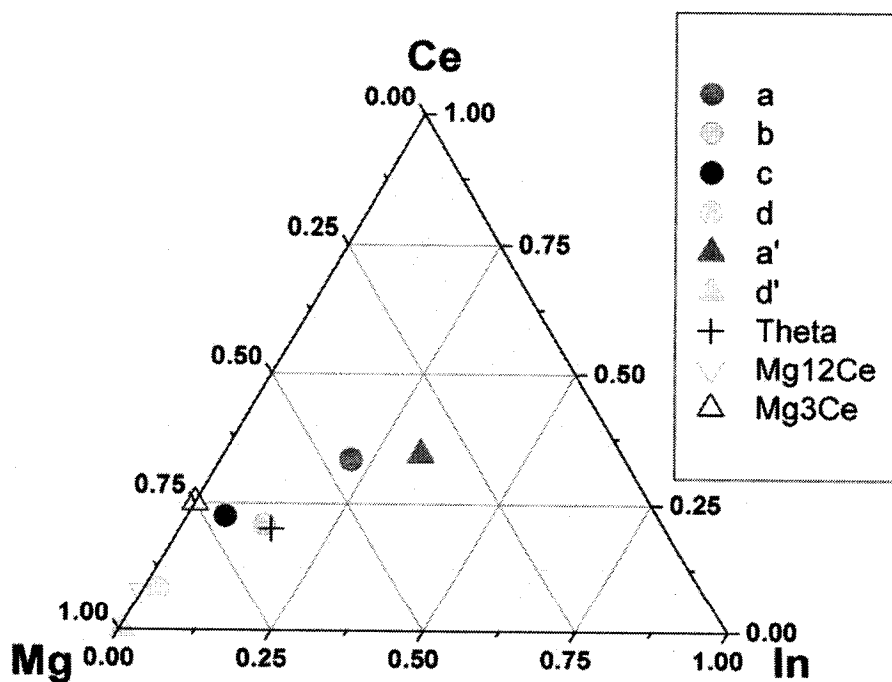
Figure 4-23 – Atomic compositions of $Mg_{62}Ce_{21}In_{17}$ phases, as-cast and annealed, and reference compounds.

4.3.1.2 MIC-22

In contrast to the many-phased structure in $Mg_{62}Ce_{21}In_{17}$ (MIC-21), the $Mg_{90}Ce_5In_5$ (MIC-22) alloy microstructure (see Figure 4-24) contains two main distinct phases only, with occasional pockets of high Si content. The alloy was analyzed in both as-cast and annealed conditions. As can be seen in Table 4-IX, the matrix (dark) phase contains 98 at% Mg, 1.5 at% In, and less than 0.02 at% Ce in the as-cast condition. The light-coloured phase contains approx. 20 at% Ce and 20 at % In, except when Si present, where In is reduced to 17.5 % and replaced by 2.5% Si. Annealing at 175 and 250°C does not change the compositions of these phases. The light phase matches the θ phase found in the dilute alloys in terms of Ce content, but has more In dissolved. This is a sign that a solid solution range is present in this phase. No $Mg_{11}Ce$ is present in this sample, unlike all other high In and Ce samples.
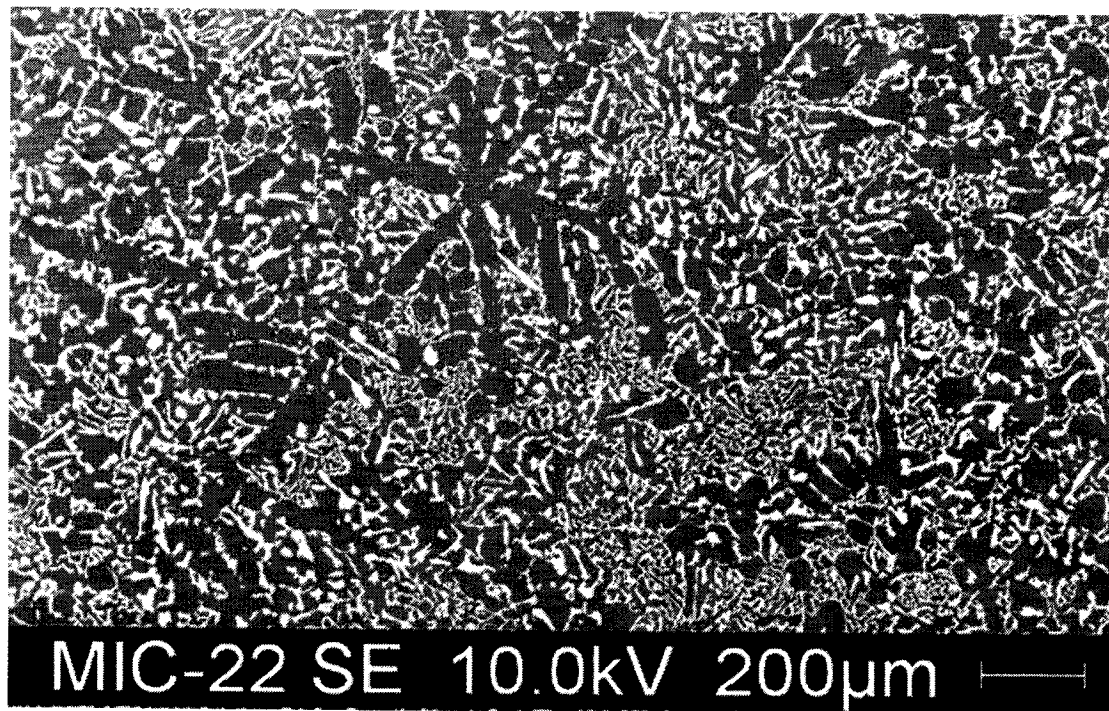
Figure 4-24 - Backscatter image showing two phases in $Mg_{90}Ce_5In_5$ alloy.

Graphing the compositions of the visible phases (see Table 4-IX and Figure 4-25) shows that annealing at 175 and at 250 has not changed the compositions of the phases at all, such that the graph points are almost completely superimposed. The θ phase is at the same Ce concentration as the light phases, but shifted towards a lower indium content.

Table 4-IX: Compositions of visible phases in Mg₉₀Ce₅In₅

	Mg at%	Ce at%	In at%	Si at%
White As-Cast	57.09	19.39	20.12	0.04
White Annealed 175	57.56	19.27	19.84	0.03
White Annealed 250	57.53	19.47	19.88	0.04
Dark As-Cast (Matrix)	97.75	0.02	1.78	0.00
Dark Annealed 175 (Matrix)	97.79	0.02	1.60	0.00
Dark Annealed 250 (Matrix)	98.09	0.03	1.42	0.01
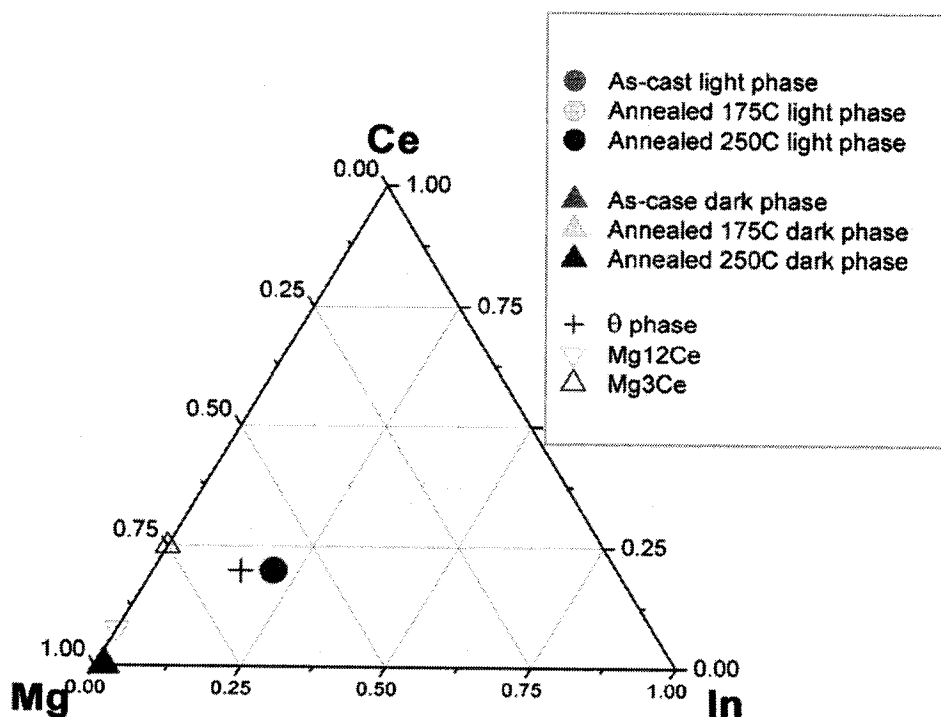
Figure 4-25 - Mg₉₀Ce₅In₅ phase compositions as-cast and annealed

4.3.2 MIC-23

The third high In and Ce alloy, $Mg_{84}Ce_6In_{11}$, also consisted of multiple phases. These phases were difficult to quantify due to the relatively fine distribution of the phase regions, as can be seen in Figure 4-26. The phases quantified successfully using EDS were the lightest and the darkest visible phases. As can be seen in Table 4-X, the light phase corresponds to the composition of the θ phase, whereas the dark phase is magnesium matrix with some dissolved indium.
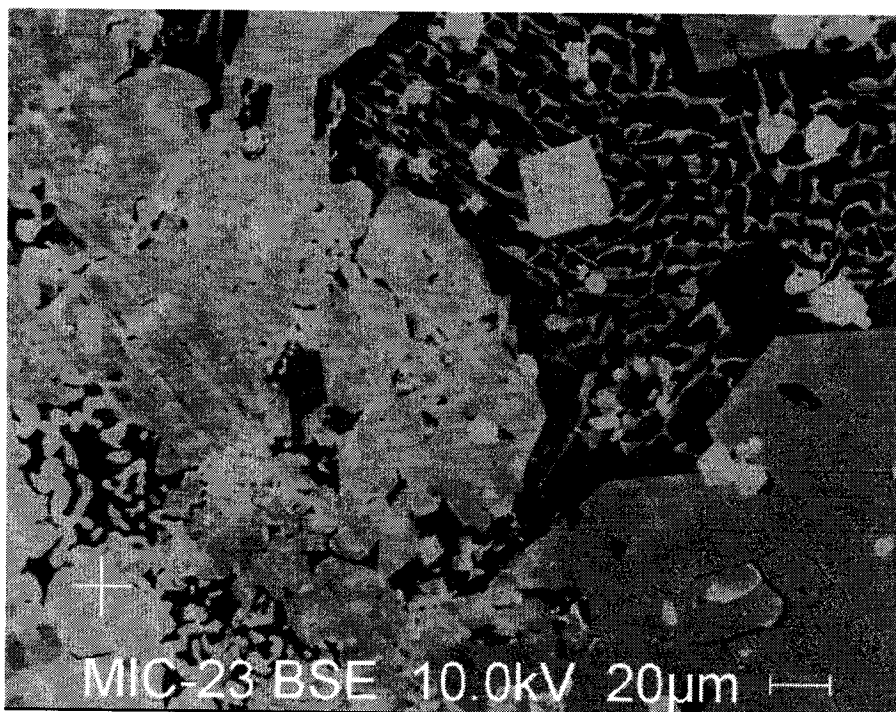
Figure 4-26 - $Mg_{84}Ce_6In_{11}$ alloy microstructure.

Table 4-X: Compositions of measurable phases in sample $Mg_{84}Ce_6In_{11}$

	Mg at%	In at%	Ce at%	Mg+In/Ce
light phase	58	19.98	21.77	3.58
dark phase	97.61	2.3	0	n/a

These compositions are shown in graphic form in Figure 4-27, with the θ phase composition and that of $Mg_{11}Ce$ included for comparison, as in previous figures.
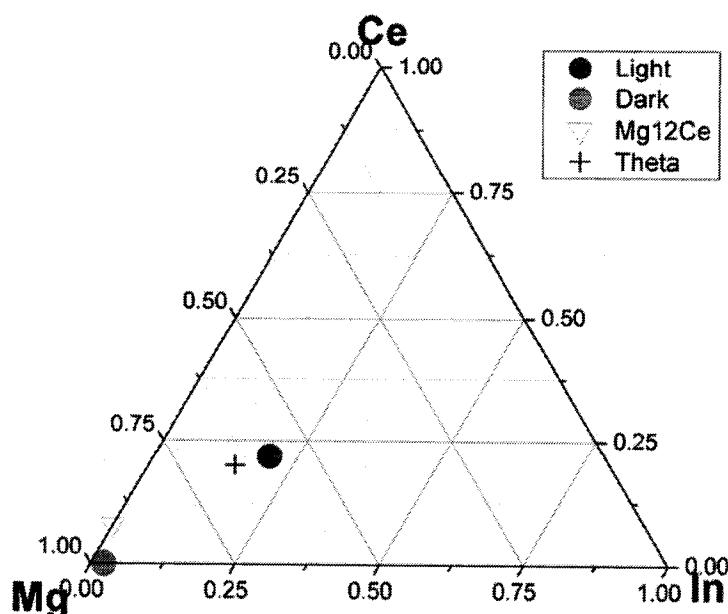
Figure 4-27 - Compositions of some phases in Mg$_{84}$Ce$_6$In$_{11}$.

4.3.3 Thermal Analysis

Cooling curve analysis of the high In and Ce alloys proved not to be feasible in the resistance furnace due to the long hold time necessary for dissolution and the incomplete gas protection at higher temperatures. However, using the induction furnace with a controlled inert atmosphere, several successful cooling curve trials were made on these alloys. These cooling curves, with their first derivative curves superimposed on them, can be seen in Figures 4-29 to 4-32.

The first derivative peaks in these cooling curve graphs represent the temperatures of the arrests occurring during cooling of each alloy, and correspond to phase transformations. Naturally, alloys containing more phases also show more cooling arrests.

In addition to the synthesized alloys with high concentrations of In and Ce, one dilute alloy observed to contain high levels of the intermetallic compound (MIC-13) was subjected to DSC testing.

77

4.3.3.1 MIC-21

Cooling curve analysis was not successful on this alloy. DSC testing yielded values for the liquidus temperature. A sample DSC graph can be seen in Figure 4-28.

A summary of results drawn from graphs such as the one in Figure 4-28, for this alloy as well as the other two high-Ce/In alloys, can be seen in Table 4-XI. The values shown represent averages of several trials. Each value was obtained using the Setaram software to calculate the onset temperature. As mentioned in section 3, Experimental Methodology, the enthalpy values from these tests were not found to be reliable enough to include.
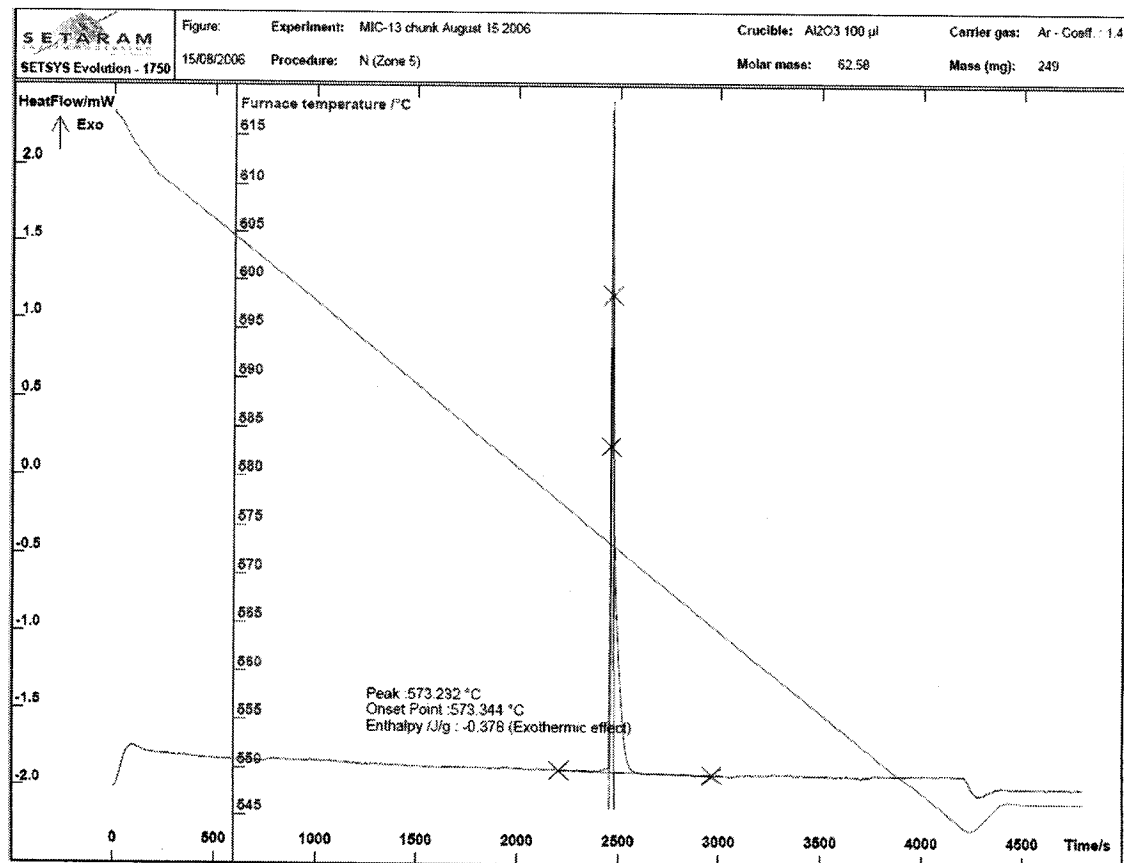
Figure 4-28 - Sample DSC graph from Setaram.

4.3.4 MIC-22

Alloy $Mg_{90}Ce_5In_5$ (MIC-22) shows a thermal arrest at approximately 581°C which seems to be the eutectic reaction $L \rightarrow \alpha\text{-Mg} + \theta$. In both cooling curve and DSC analysis, this alloy displayed no arrest above 581°C. This fact, in combination with the eutectic microstructure of this alloy shown in Figure 4-24, indicates that this alloy is at or close to the eutectic composition, and therefore the eutectic temperature is coincident with the liquidus at this composition. Although the DSC test range was limited by the Setaram equipment, which in the configuration used had a maximum temperature of 800°C, cooling curve analysis began above 825°C. It was clear from observing the alloy's behaviour during cooling curve analysis that complete melting took place, therefore there is no possibility that the liquidus for this alloy occurs at a higher temperature than the test range.
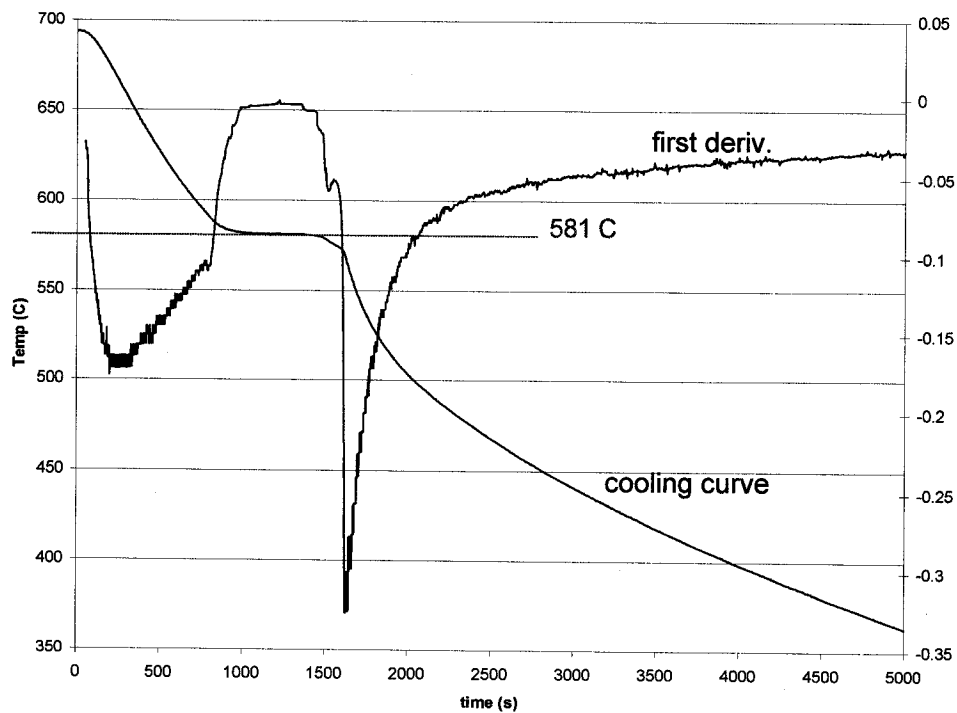
Figure 4-29 – Cooling curve 28/07/2006 MIC-22/$Mg_{90}Ce_5In_5$ (resistance furnace)
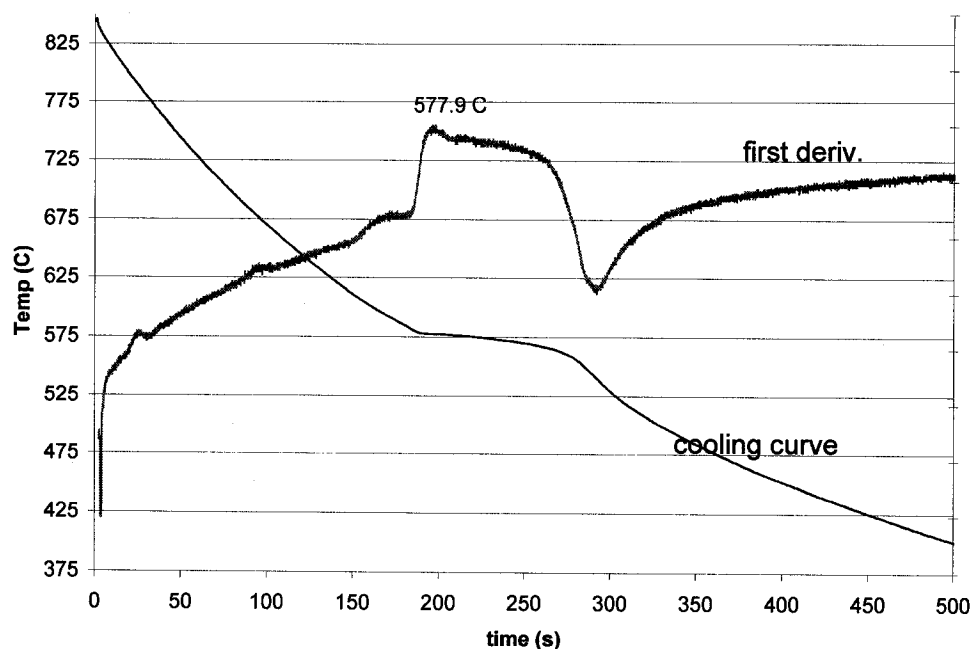
Figure 4-30 – Cooling curve 16/05/2007 MIC-22/Mg$_{90}$Ce$_5$In$_5$ (induction furnace)

4.3.5   MIC-23

Alloy Mg$_{84}$Ce$_6$In$_{11}$ shows a thermal arrest at 910-950°C. This may be the formation of a primary phase. The five phases were not all identified in this alloy, but it could be hypothesized that this is the formation of the a phase in MIC-21. Repeatability was still an issue for certain arrests in this alloy. While the eutectic transformation was relatively consistent across repeats, other arrests were not. This could be due to oxidation, or to incomplete dissolution of alloying elements leading to an inhomogeneous mixture.

The second arrest at 623°C may correspond to the formation of a phase corresponding to the c phase in MIC-21, while the third arrest at 577 represents the eutectic reaction L→ α-Mg + θ. The arrest at 555-563°C could be a solid state transformation of Mg$_{11}$Ce.
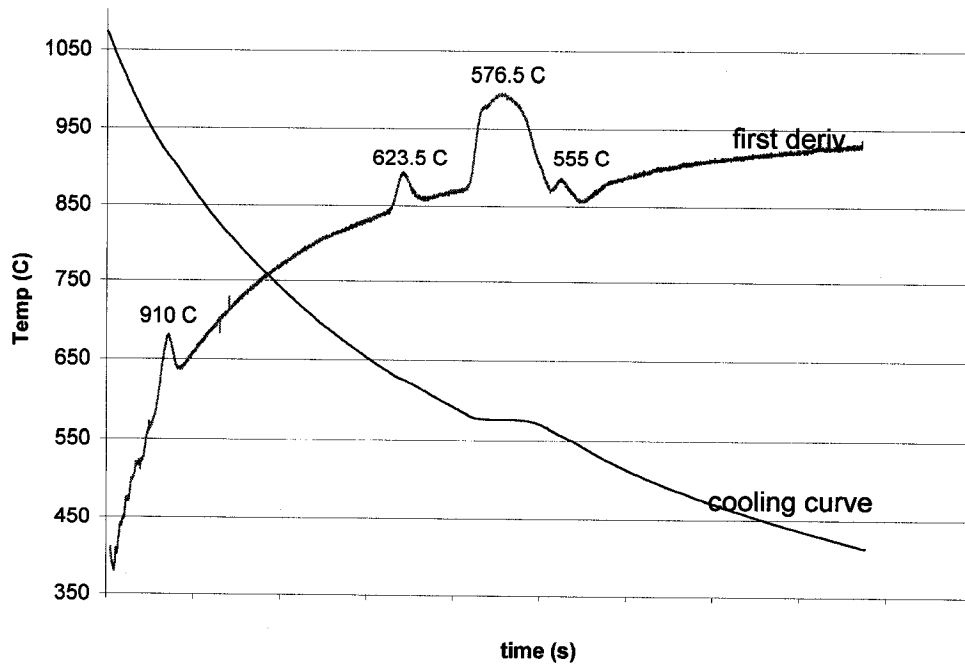
Figure 4-31 – Cooling curve 06/10/2006, MIC-23/Mg$_{84}$Ce$_6$In$_{11}$ alloy (induction furnace).
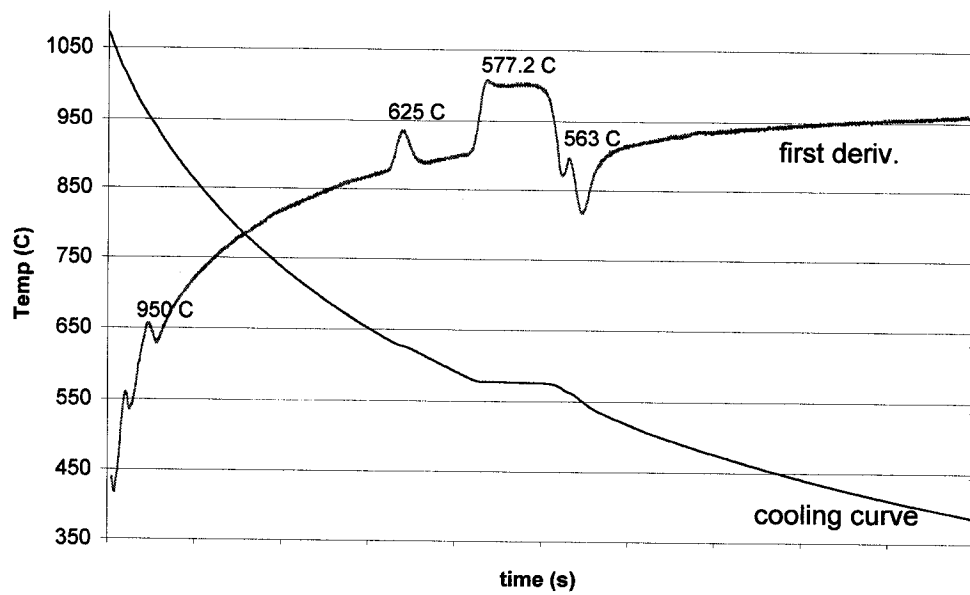
Figure 4-32 - Cooling curve 11/10/2006, MIC-23/Mg$_{84}$Ce$_6$In$_{11}$ alloy (induction furnace).

Table 4-XI collects the thermal analysis data for all three high-Ce/In alloys, as well as the binary eutectic temperature for the Mg-Ce system. It can be seen that not all alloys display peaks for all phase change events, which is attributable to the fact that not all alloys contain the same phases.

Table 4-XI: Thermal analysis of high In and Ce alloys.

Date / Type	Sample ID	Arrest 1 (°C)	Arrest 2 (°C)	Arrest 3 (°C)	Arrest 4 (°C)
6/10/2006 CC	$Mg_{84}Ce_6In_{11}$ (MIC-23)	910	623	576	555
11/10/2006 CC	$Mg_{84}Ce_6In_{11}$ (MIC-23)	950	625	577.2	563
28/07/2006 CC	$Mg_{90}Ce_5In_5$ (MIC-22)			581	
16/05/2007 CC	$Mg_{90}Ce_5In_5$ (MIC-22)			577.9	
DSC	$Mg_{90}Ce_5In_5$ (MIC-22)			580.3	
DSC	$Mg_{99}Ce_{.3}In_{.6}$ (MIC-13)		639.6	577.2	
DSC	$Mg_{62}Ce_{21}In_{17}$-b (MIC-21)	749.4	605.4	605.4	
Mg-Ce Eutectic[6] (literature value)				591±2	

Figure 4-33 places the values obtained using thermal analysis for the ternary eutectic and liquidus temperatures on a three-dimensional figure. On the back faces of this figure are superimposed sections of the appropriate binary phase diagrams, such that the Mg-In diagram appears on the face corresponding to 0% Ce, and the Mg-Ce diagram appears on the 0% In face.
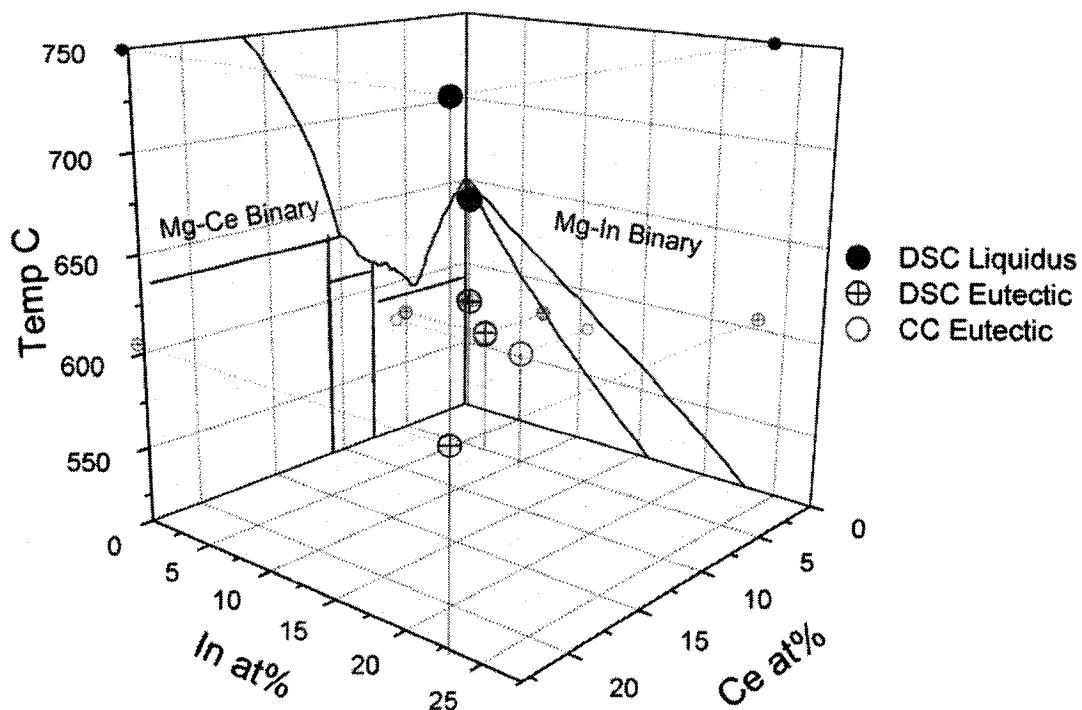
Figure 4-33 - Ternary thermal arrest values obtained from DSC and cooling curve analysis of high In and Ce alloys

4.3.6 θ Phase Analysis of High In and Ce Samples Using XRD

Analysis of XRD patterns including peaks from the new intermetallic compound was inconclusive, as no one possible crystal structure stood out as a definite match. The spectra from the three high-Ce/In samples are shown in Figure 4-34 and in Figure 4-35. Above 80° 2θ, peaks were so numerous and so close to the background that it was not considered useful to show this range. The most likely crystal structure for the θ compound, based on peaks left over after ignoring those which match known compounds present in the samples, is a tetragonal structure. Sometimes identification of unknown compounds can be suggested using comparison of the spectra with spectra generated from similar compounds, but in this case no compound has as yet been identified that has a similar pattern.
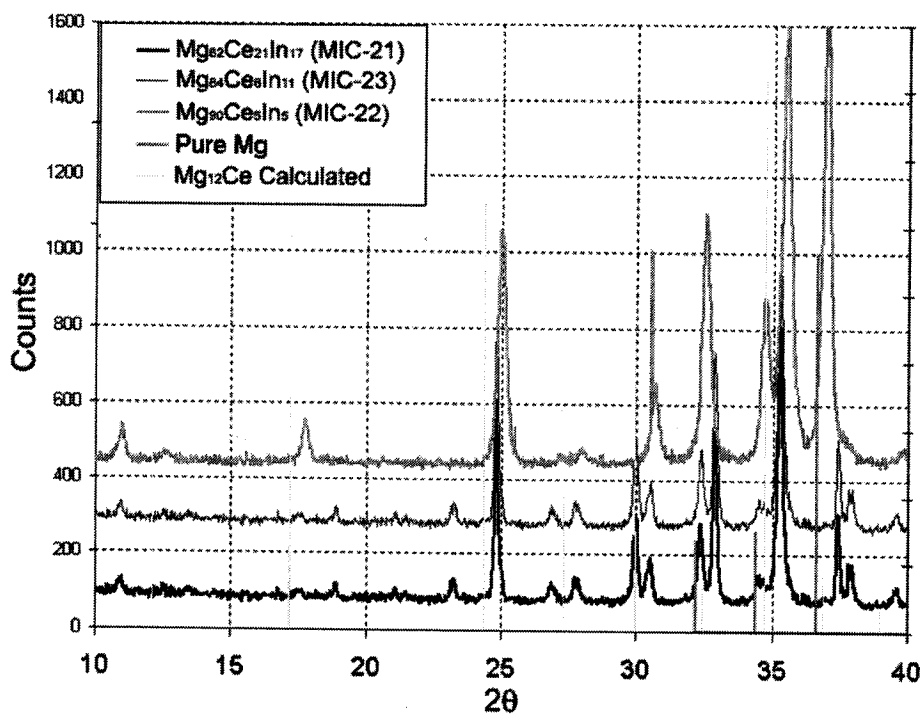
Figure 4-34 - XRD spectra for high In and Ce alloys in the range 10 to 40 2θ
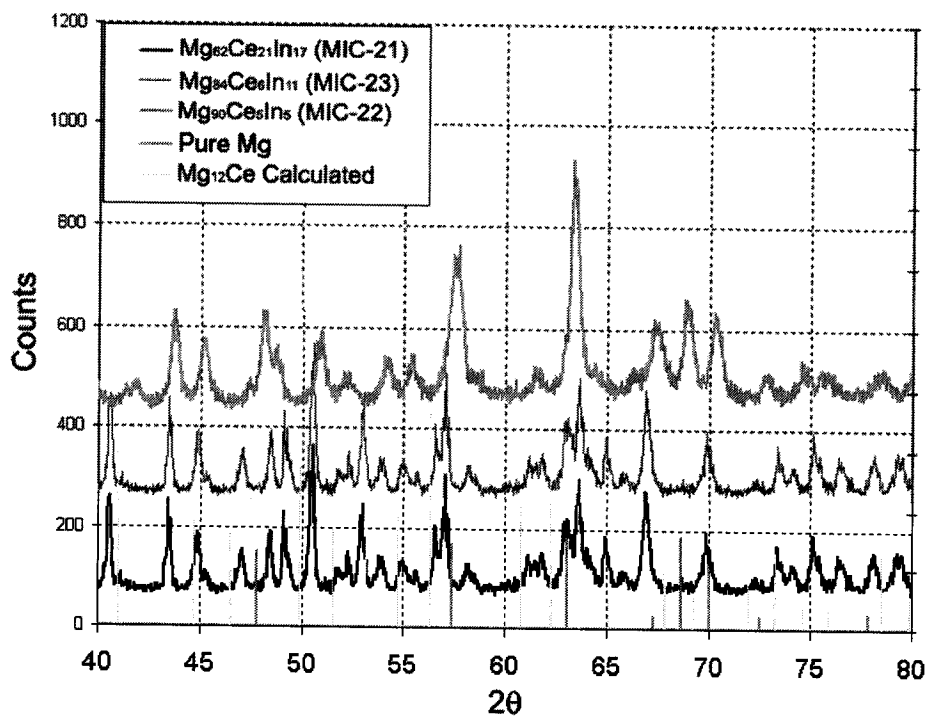
Figure 4-35 - XRD spectra for high In and Ce alloys in the range 40 to 80 2θ

It can be seen in Figure 4-34 and in Figure 4-35 that allowing for peak shift due to solid solution with indium, magnesium peaks are present in all samples. In addition, $Mg_{11}Ce$ peaks may be matched if again a shift is assumed due to dissolution of indium in the compound.

The unmatched peak noted in the dilute alloy samples at 43.5° 2θ (see Figure 4-13) also appears in these spectra. This provides some confidence that this peak does indeed come from the new compound.

Sample $Mg_{90}Ce_5In_5$ (MIC-22) is the most promising place to look for peaks for the new compound, since this alloy displays only two phases, as previously discussed, those being Mg matrix with dissolved In, and θ. However, since many of the peaks assumed to be $Mg_{11}Ce$ are also present in this sample, and the sample contains no $Mg_{11}Ce$ according to EPMA and SEM analysis, identification of the structure of the new compound does not appear to be possible using XRD methods. One possibility is that the new compound has a very similar structure to $Mg_{11}Ce$, which, given the composition of θ at $Mg_{60-67}Ce_{20}In_{13-20}$, seems unlikely. Another possible explanation is that $Mg_{11}Ce$ is present in the $Mg_{90}Ce_5In_5$ alloy as well, and was not observed using techniques other than XRD. Observations on peaks which are not well matched to peaks in standard spectra for Mg and for $Mg_{11}Ce$ can be found in Table 4-XII.

Table 4-XII: XRD peaks in high In and Ce alloys not matched by standards

2θ	Normalized Counts	Observations
11.05	15.76	All three alloys have it, not matched by standards.
23.25	11.61	Alloys MIC-21B and MIC-23 only.
21.5	9.95	Alloy MIC-21B only.
39.95	7.30	Alloy MIC-22 only.
40.65	19.63	Alloy MIC-22 is missing a peak shown in both other alloys, which matches an $Mg_{12}Ce$ peak.
42.025	6.81	Alloy MIC-22 only.
43.6	19.63	All three alloys have it, not matched by standards.
49.1	12.53	All three alloys have it, not matched by standards.
69.075	20.18	Alloy MIC-22 only, but might match a Mg peak that the others don't display due to preferential orientation.

4.3.7   Solid Solubility of Indium in the θ Phase and in $Mg_{11}Ce$

It has been seen that the level of indium dissolved in the theta compound and in $Mg_{11}Ce$ (originally designated 'tau') varies between the samples examined. It can be assumed that the instance of theta found in the diffusion couple and in the annealed samples represents close to an equilibrium state, and thus the amount of dissolved indium in these samples represents the solubility limit of indium in these compounds. It has been noted that wherever indium appears to be dissolved in these compounds, its concentration varies inversely with that of magnesium (or occasionally silicon, where present). From this it can be deduced that magnesium and indium share a sublattice and that indium dissolves substitutionally in the magnesium, leaving the cerium on its own lattice, unchanged.

Table 4-XIII: Indium concentration in phases found in Mg-In-Ce samples

	bulk In at%	In at% in theta	In at% in $(Mg,In)_{11}Ce$
$Mg_{99}Ce_{.3}In_{.4}$	0.44	15.58±0.77	2.76±0.08
$Mg_{99}Ce_{.2}In_{.4}$	0.44	15.18±0.29	2.89±0.01
$Mg_{99}Ce_{.1}In_{.4}$	0.43	16.49±0.37	2.32±0.11
$Mg_{99}Ce_{.3}In_{.2}$	0.22	12.90±0.97	1.90±0.06
$Mg_{99}Ce_{.2}In_{.2}$	0.21	12.99±0.48	2.11±0.05
$Mg_{99}Ce_{.1}In_{.2}$	0.22	13.44±0.76	2.15±0.01
$Mg_{99}Ce_{.3}In_{.6}$	0.64	16.10±0.79	2.80±0.14
Diffusion Couple	4.2	16.49	1.08
$Mg_{62}Ce_{21}In_{17}$	17.11	13.53	2.41
$Mg_{84}Ce_{6}In_{11}$	10.62	19.98	
$Mg_{90}Ce_{5}In_{5}$	5.03	19.88	

Looking at Table 4-XIII, it can be seen that although indium in the θ compound from the dilute samples varies from 12.9 to 16.5, in the annealed or diffused samples the level is from 16.5 to 20.0 at% indium. 20 at% indium appears to be the limit of indium in this compound.

Dissolved indium in the $(Mg, In)_{11}Ce$ compound, in contrast, does not increase in the high In and Ce samples, but stays in the same range as in the dilute samples. It appears that the solubility of indium in this compound is much lower than in the θ compound, varying from 1.1 to 2.9 at% indium.

4.4   Calculated Phase Diagrams

4.4.1   Calculated Binary Phase Diagrams

To begin with, three binary equilibrium phase diagrams were generated using FactSage©
with the latest CTRC databases, and with the addition of unpublished preliminary
optimizations.[31] These calculated binaries are included here as Figure 4-36, Figure 4-37,
and Figure 4-38 in order to show that while sometimes simplified, these diagrams do
have good correspondence with the literature binary phase diagrams in the magnesium
rich corner.
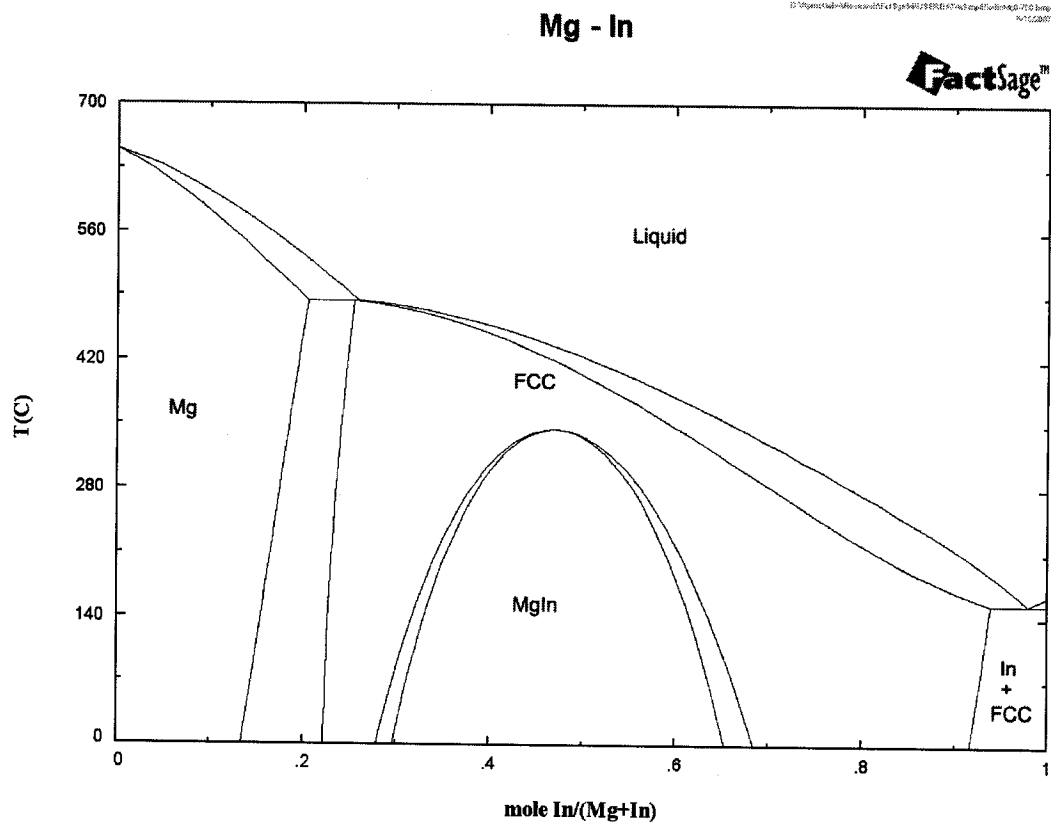
Figure 4-36 - Simplified Mg-In binary equilibrium phase diagram generated by FactSage©.

The Mg-In diagram is the least complete, having been generated specifically for this
study using available literature binary data and first principles. Several Mg-In compounds

have been left out in the interest of simplicity, since the Mg-rich side consists mainly of a broad solid solution, and this is the area of interest in this study.
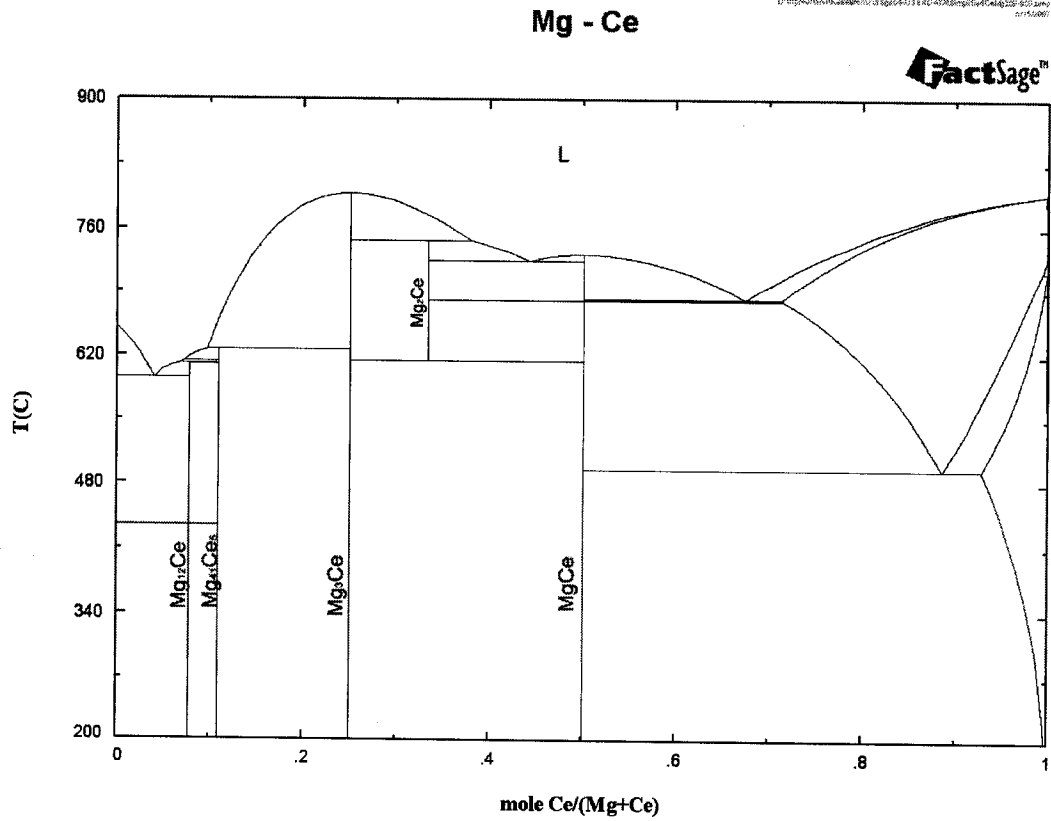
Figure 4-37 - Mg-Ce binary equilibrium phase diagram generated by FactSage.

In contrast to the Mg-In diagram, the Mg-Ce is quite complete and conforms very closely to the literature phase diagram as seen in Figure 4-37.

Ce - In

Figure 4-38 - Ce-In binary equilibrium phase diagram generated by FactSage.

Finally, the Ce-In calculated binary diagram, while it includes all compounds in the system, still requires some optimization to more closely match the literature data. Since in this study the Mg-rich corner was being examined, this binary is the least important of the three.

4.4.2 Calculated Isopleths

Isopleths were calculated at the indium concentrations used in the dilute alloys. Three isopleths were calculated, at respectively 0.22 at% In, 0.44 at% In, and 0.66 at% In. These isopleths do not differ greatly from each other due to the small variation in indium concentration. Each isopleth was calculated in the range 0 to 2 at% Ce.

Figure 4-39 - Calculated Mg-Ce-In isopleth at 0.22 at% In

Figure 4-39 comprises the calculated Mg-Ce-In isopleth at 0.22 at% In. Upon the isopleth are superimposed the experimental points for both the liquidus arrests and the eutectic arrests. No eutectic region appears on the calculated isopleth due to the fact that this recent discovery has not yet been incorporated into the FactSage databases. However, the experimental data show where such a line will appear. Given the very small amounts of alloying elements in the samples shown in these isopleths, the close correspondence with calculated values is not surprising.

91
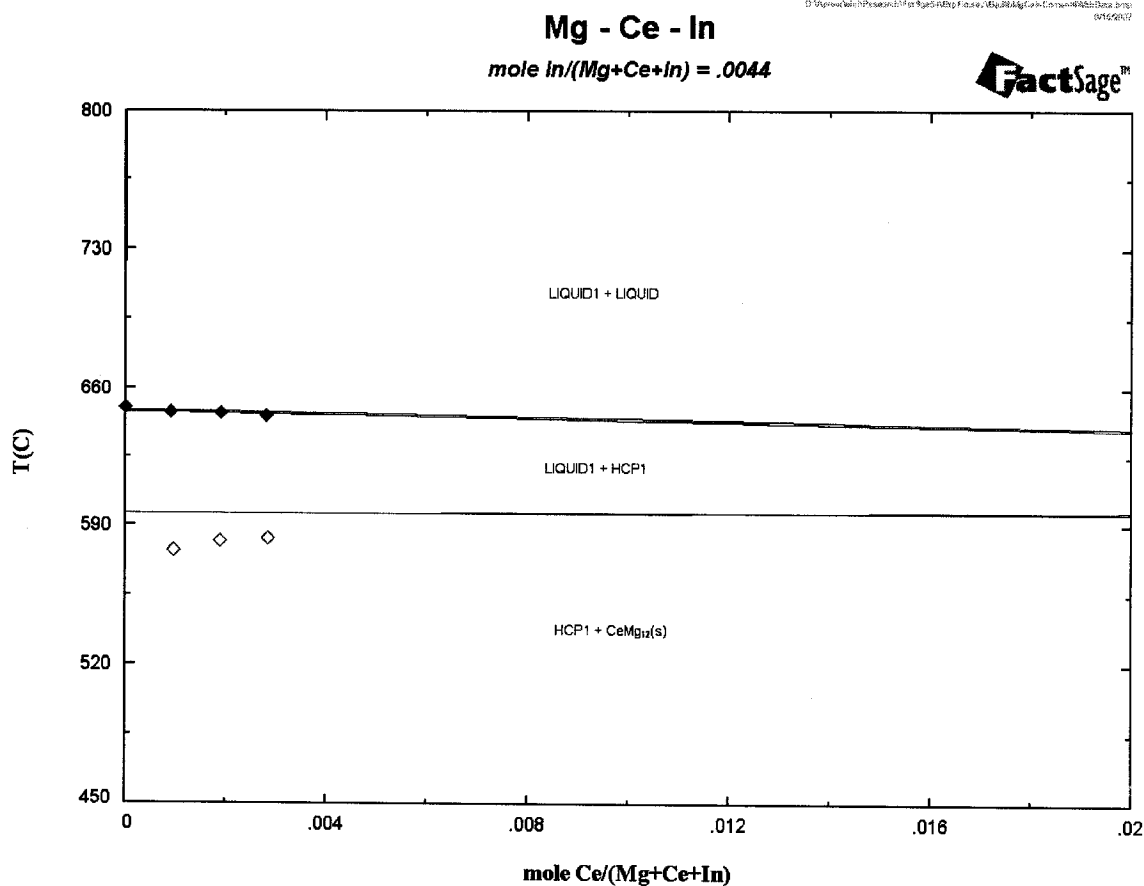
Figure 4-40 - Calculated Mg-Ce-In isopleth at 0.44 at% In

Figure 4-40 and Figure 4-41, similarly, are isopleths calculated with the other two indium concentrations from the dilute alloy study, at 0.44 at% In and 0.66 at% In. Again, the close correspondence is partly due to the very small deviation from pure magnesium in these alloys, but is nonetheless a good confirmation of the validity of both the calculated diagrams and the experimental data.
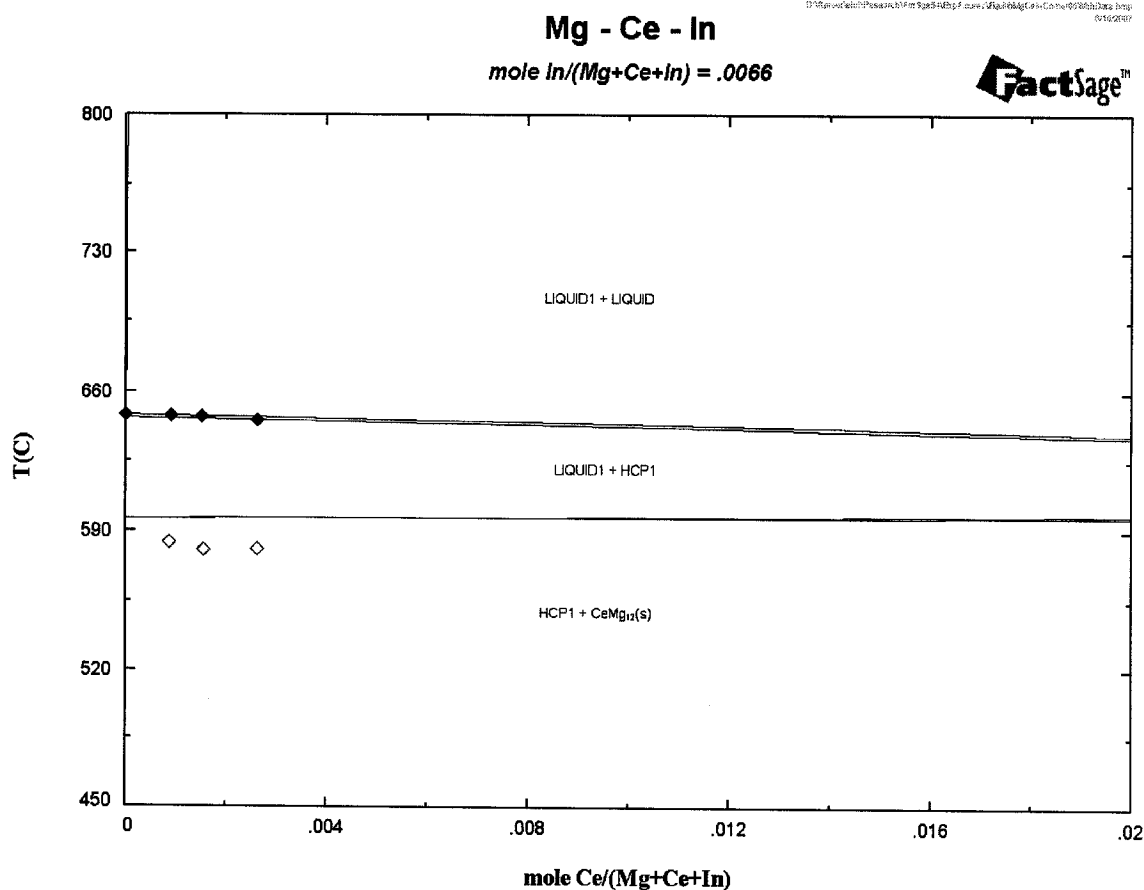
Figure 4-41 - Calculated Mg-Ce-In isopleth at 0.66 at% In

4.4.3 Calculated Isotherm at Diffusion Couple Temperature

The last calculated diagram, shown in Figure 4-42, represents the ternary system at a constant temperature of 390°C. This is the temperature at which the diffusion couple in this study was made, and the diffusion zone compositions have been superimposed on the diagram. In addition, the binary compounds have been placed on the three sides of the diagram representing the binary systems.

All experimentally determined zone compositions fall on tie lines leading from binary Mg-Ce compounds towards the indium side of the figure except the new ternary compound, which does not yet exist in the database used for the calculation.

Figure 4-42 - Calculated Mg-Ce-In isotherm at 390°C

5 Summary and Conclusions

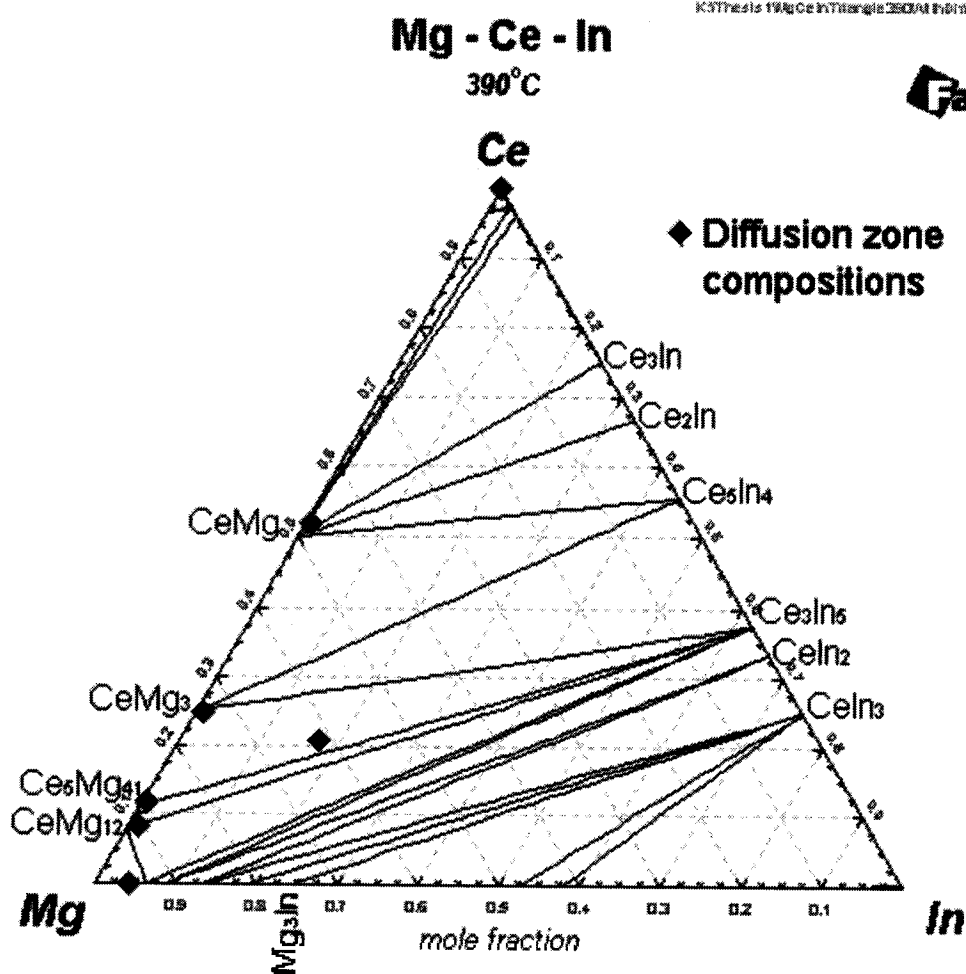Thermal analysis, combined with SEM, EPMA and XRD techniques, have yielded useful data towards the construction of a section in the Mg-rich corner of the ternary equilibrium phase diagram in the Mg-Ce-In system. This system has not previously been described in the literature, but may be of interest in magnesium wrought alloy research due to the possible effects of Ce and In on pure Mg.

The dilute alloys studied in the Mg-Ce-In system revealed the liquidus surface in that region of the system, as well as giving information about one new ternary compound and indium solubility in binary Mg-Ce compounds.

First derivatives of cooling curves are effective in identifying small arrests barely visible to the naked eye in the cooling curves. Differential thermal analysis confirms the existence of these arrests.

A ternary eutectic point, related to the binary eutectic at 591°C ± 2 °C in the Mg-Ce system, was discovered. The eutectic melting point is approximately 583°C. The eutectic composition, based on microstructural and cooling curve analysis, is very close to $Mg_{90}Ce_5In_5$.

Figure 5-1 shows all the compounds, phases, and diffusion zones studied on one ternary figure. Looking at the crosses representing the diffusion zones, a path can be drawn which represents the Mg-Ce binary phases with a small amount of indium dissolved, i.e. a path parallel to the Mg-Ce side of the triangle but slightly offset towards the indium corner, except for zone 5A, which represents the new intermetallic compound. Therefore, at the diffusion temperature of 390°C and with endpoints of pure Ce and Mg5at%In, only one true ternary intermetallic compound appears, the remainder of the phases being binary Mg-Ce compounds with dissolved indium.

Atomic fraction of compounds and phases present
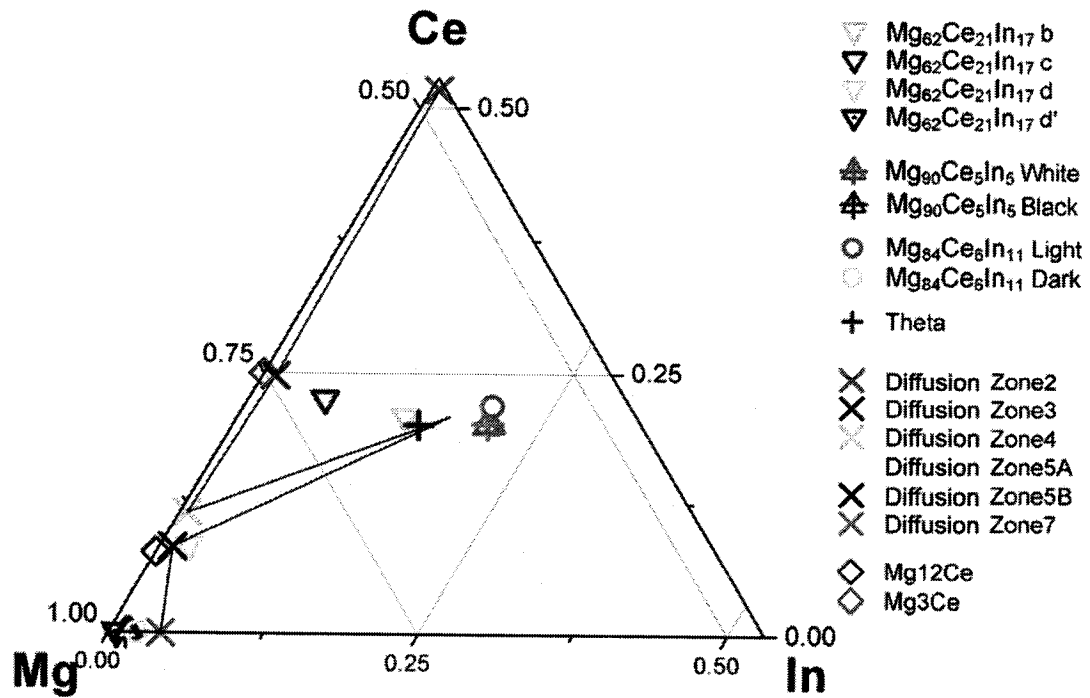
Figure 5-1 - Compositions of alloys, phases, and diffusion zones

A new intermetallic compound exists in the system. It is identified as θ and has the composition $Mg_{60-65}Ce_{20}In_{15-20}$.

XRD analysis of dilute and high In and Ce alloys revealed several peaks which are not matched by standards for Mg or for $Mg_{11}Ce$. One such peak, at 43° 2θ, appears in both dilute and high In and Ce alloys. The unmatched peaks taken as a set did not yield a definite crystal structure identification for the new ternary compound θ, though a tetragonal structure seemed to be indicated.

Several binary Mg-Ce compounds were found to dissolve indium. One of these is the phase identified in this thesis as τ, which has a composition of $(Mg\text{-}In)_{11}Ce$. The others are binary compounds $Mg_{41}Ce_5$, Mg_3Ce and $MgCe$.

Calculated isopleth sections at the indium levels of experimental alloys have good agreement with liquidus temperatures found experimentally.

A calculated isotherm at the diffusion couple temperature of 390 °C shows that the compositions of all the zones in the diffusion couple have good agreement with the calculated ternary, except the new intermetallic compound.

6 Future Work

Future work on the alloys containing high concentrations of In and Ce should include high temperature DTA in order to confirm the liquidus points detected using cooling curve analysis. In addition, TEM work might shed light on the structure of the new intermetallic compound observed, if a clear diffraction pattern can be obtained and related to known structures. Finally, a series of anneal and quench tests could aid in determining the phase transformation boundaries.

DSC using an instrument with good enthalpy calibration would add more thermodynamic data to the system, towards the eventual calculation of a full ternary phase diagram.

Another possible approach to the question of compound identification using XRD would be to predict possible theoretical arrangements of the species present, and model these, then compare the generated spectra with the experimental one in order to attempt a match.

Additional diffusion couples were attempted, but diffusion was not successful. Successful couples might help define the maximum solubility of In in $(Mg,In)_4Ce$ (i.e. the θ compound) by providing an excess of available In atoms, and might provide more information on the phase boundaries in the ternary isothermal section.

7 References

[1] G.V. Raynor, The Physical Metallurgy of Magnesium and its Alloys, Pergamon Press, New York, 1959.

[2] W. B. Pearson, The Crystal Chemistry and Physics of Metals and Alloys, Wiley-Interscience, New York, 1972.

[3] AA. Nayeb-Hashemi, J.B. Clark, "The In-Mg (Indium-Magnesium) System", Bulletin of Alloy Phase Diagrams, Vol. 6, No.2 1985, 149-160.

[4] A.A. Nayeb-Hashemi, J.B. Clark, "The Ce-Mg (Cerium-Magnesium) System", Bulletin of Alloy Phase Diagrams, Vol. 9, No.2 1988, 162-172.

[5] L.L. Rokhlin, Magnesium Alloys Containing Rare Earth Metals, Taylor & Francis, New York, 2003.

[6] Metals Handbook, 10th ed. Vol 3 Alloy Phase Diagrams, ASM International, 1992.

[7] A. Prince, Alloy Phase Equilibria, 1966, Elsevier Publishing, Amsterdam.

[8] E. Jak, H.G. Lee, P.C. Hayes, "Improved Methodologies for the Determination of High Temperature Phase Equilibria", Korean Journal of Materials vol. 1 pp. 1-8. 1995.

[9] L. Backerud, G. Chai, J. Tamminen, Solidification Characteristics of Aluminum Alloys. Vol. 2. Foundry Alloys, American Foundrymen's Society, Inc., 1990.

[10] D. Kevorkov, unpublished work, 2005.

[11] R. Schmid-Fetzer, "On Liquidus and Solidus Temperatures in AZ and AM Alloys", Proceedings of the 2006 TMS Meeting, Magnesium Technology Session, 2006.

[12] R. Montanari, "High-temperature XRD investigations on phase transformations", La Metalurgia Italiana, 2/2004.

[13] F. J. J. van Loo, "Multiphase Diffusion in Binary and Ternary Solid-State System", Prog. Solid St. Chem., 1990, vol.20, pp. 47-99.

[14] A. A. Kodentsov, G. F. Bastin, and F. J. J. van Loo, "The Diffusion Couple Technique in Phase Diagram Determination", Journal of Alloys and Compounds, 2001, 320, pp. 207-217.

[15] DoITPoMS Micrograph Library, University of Cambridge, http://www.doitpoms.ac.uk/miclib/index.php.

[16] Joseph Goldstein, Scanning Electron Microscopy and X-ray Microanalysis, Springer; 3rd ed. 2003.

[17] Gerald Kothleitner, "Energy-Filtering Transmission Electron Microscopy (EFTEM)", Gatan GIF school presentation, California, 2000.

[18] David B Williams, C Barry Carter, Transmission Electron Microscopy: A Textbook for Materials Science, Plenum Press, New York,1996.

[19] J-P Morniroli, "Large angle convergent beam electron diffraction - application to crystal defects", *Pub. Societé Française des Microscopies*, 2002.

[20] C. Antion, P. Donnadieu, C. Tassin, A. Pisch, A. Deschamps, P. Chaudouët, "Magnesium rare earths alloys: Elaboration of new alloys and fine scale microstructures in Mg-RE alloys", *Matériaux* 2002

[21] M. Piché, A.D. Pelton, C. Brochu, "A thermodynamic database for magnesium alloys", *Magnesium Technology 2003*, TMS 2003.

[22] G.V.Raynor, The Physical Metallurgy of Magnesium and Its Alloys, Pergamon Press, London, 1959.

[23] Teatum, E. T., Gschneider, K. Jr & Waber, J. T. (1968). "Compilation of calculated data useful in predicting metallurgical behaviour of the elements in binary alloy systems", USAEC Report LA-4003, 206 pp. [Supercedes Report LA-2345 (1960).] Washington, DC: United States Atomic Energy Commission.

[24] M. Avedesian and H. Baker ed., ASM Specialty Handbook: Magnesium and Magnesium Alloys, ASM International, Ohio, 1999.

[25] K. Scheme and E. Hornbogen, "Rapidly Solidified Mg-Li Base Superlight Alloys." *Proceedings of the International Conference on Light Metals*, ed, T. Khan, G.Effenberg, ASM International, Amsterdam, 1990, pp. 797-803.

[26] K.H.Matucha, "Structure and Properties of Non Ferrous Alloys," *Materials Science and Technology: A Comprehensive Treatment;* Vol. 8, ed, R.W. Cahn, P. Haasen, E.J. Kramer, VCH, Weinheim; New York; Basel; Cambridge; Tokyo; 1996.

[27] K.U. Kainer and F. von Dutch, "The Current State of Technology And Potential for further Development of Magnesium Applications" Magnesium Alloys and Technologies, ed, K.U.Kainer, Wiley-VCH Verlag GmbH & Co. KGaA, Weinheim, 2003, 1-22.

[28] W. B. Pearson, The Crystal Chemistry and Physics of Metals and Alloys, Wiley-Interscience, New York, 1972.

[29] X. Zhang, unpublished work, 2005.

[30] Program created by Stuart Easson, 2005.

[31] Unpublished FactSage optimizations prepared by Youn-Bae Kang, 2006.